

May 2023

The Search for the Four-electron Reduced Intermediate in the Cytochrome C Nitrite Reductase (CCNIR) - Catalyzed Reduction of Nitrite

Victoria Lynn Mandella
University of Wisconsin-Milwaukee

Follow this and additional works at: <https://dc.uwm.edu/etd>

 Part of the [Analytical Chemistry Commons](#), and the [Inorganic Chemistry Commons](#)

Recommended Citation

Mandella, Victoria Lynn, "The Search for the Four-electron Reduced Intermediate in the Cytochrome C Nitrite Reductase (CCNIR) - Catalyzed Reduction of Nitrite" (2023). *Theses and Dissertations*. 3186.
<https://dc.uwm.edu/etd/3186>

This Dissertation is brought to you for free and open access by UWM Digital Commons. It has been accepted for inclusion in Theses and Dissertations by an authorized administrator of UWM Digital Commons. For more information, please contact scholarlycommunicationteam-group@uwm.edu.

THE SEARCH FOR THE FOUR-ELECTRON REDUCED INTERMEDIATE IN THE
CYTOCHROME C NITRITE REDUCTASE (CCNIR) - CATALYZED REDUCTION OF
NITRITE

by

Victoria Lynn Mandella

A Dissertation Submitted in
Partial Fulfillment of the
Requirements for the Degree of

Doctor of Philosophy
in Chemistry

at

The University of Wisconsin-Milwaukee

May 2023

ABSTRACT

THE SEARCH FOR THE FOUR-ELECTRON REDUCED INTERMEDIATE IN THE CYTOCHROME C NITRITE REDUCTASE (CCNiR) - CATALYZED REDUCTION OF NITRITE

by

Victoria Lynn Mandella

The University of Wisconsin-Milwaukee, 2023
Under the Supervision of Professor A. Andrew Pacheco

Although there are many nitrogen species in the nitrogen cycle, nitrite occupies a central role. Nitrite can either reduce to ammonium or dinitrogen or oxidize to nitrate. Ammonium and nitrate can be found in the environment; however, problems arise when the accumulation of these nitrogen species leads to eutrophication in aquatic environments. High ammonium or nitrate levels in lakes or other bodies of water can lead to the overgrowth of algae, which causes the blockage of sunlight to different species below the water surface. Imbalance in the ecosystem is a serious environmental issue that can be addressed by further studying and understanding the nitrogen cycle. Cytochrome *c* Nitrite Reductase (ccNiR) is a complex multi-heme respiratory enzyme, found in the aquatic bacteria *Shewanella oneidensis*, that catalyzes the reduction of nitrite to ammonium. Earlier in vitro studies had used the strong reductant methyl viologen monocation radical (MV_{red}) to study the reaction, but under these conditions, no intermediates accumulate, which leaves the mechanistic steps of the catalysis uncharted. In this study, ccNiR-mediated nitrite reduction was effected by a variety of weak reductants in place of MV_{red} . Assays for hydroxylamine and ammonium formation showed that ammonium was still the only significant product under these conditions. However, intermediate species in which partially reduced nitrogenous moieties were bound at the ccNiR active site were now detectable. The kinetics of intermediate and ammonium formation were monitored by conventional and stopped-

flow UV-Visible Spectroscopy. The results presented herein pave the way to further characterizing the catalytic intermediates using electron paramagnetic resonance spectroscopy and time resolved X-ray crystallography. To that end, preliminary crystallographic results collected at the European X-Ray free-electron laser facility are also presented.

© Copyright by Full Name, 2023
All Rights Reserved

*To my nephew, Logan Charles Scharf
When you were a baby, I held you in my arms while studying for a final exam and that's when I
knew this thesis would be dedicated to you. I hope your love for math and science continues to
grow. I love you with all of my heart.*

TABLE OF CONTENTS

LIST OF FIGURES	ix
LIST OF TABLES	xiii
LIST OF SCHEMES	xv
LIST OF ABBREVIATIONS	xvii
ACKNOWLEDGEMENTS	xviii
Chapter 1 Introduction	1
1.1. The importance of nitrogen	1
1.2. What is the nitrogen cycle?	2
1.3. The importance of nitrite in the nitrogen cycle	5
1.4. Metalloenzymes and their relationship to the nitrogen cycle	6
1.5. Shewanella Oneidensis MR-1	9
1.6. Hemes	10
1.7. Cytochromes	11
1.8. Structure of ccNiR	15
1.9. Atypical nitrite ammonifying enzymes.....	18
1.10. The bioenergetics of nitrite ammonification	19
1.11. CcNiR reaction mechanism	21
1.11.1. Overview.....	21
1.11.2. Structural and computational analyses of the ccNiR mechanism	22
1.11.2.1. The resting enzyme and nitrite activation at the active site.....	22
1.11.2.2. The Possible Pathways for the First N–O Bond Cleavage.....	26
1.11.2.3. Heme iron-nitrosyl intermediates and the second N – O bond cleavage.....	28
1.12. Possible roles for the Ca²⁺ ion	32
1.13. Detection of catalytic intermediates under weakly reducing conditions	33
1.13.1. Detection of high potential intermediates.....	33
1.13.2. Detection of lower potential ferrous nitrosyl intermediates.....	34
1.14. Specific objectives of this thesis	35
1.15 References	37
Chapter 2 The expression, purification, and characterization of Cytochrome c Nitrite Reductase	44
2.1 Overview	44
2.2. Materials and Methods	44
2.2.1. General instrumentation.....	44
2.2.2. General Materials.....	45
2.2.3. Large Scale <i>S. oneidensis</i> TSP-C cell culture for wild type ccNiR protein.....	45

2.2.4. Pyridine hemochromagen assay for determining the concentration of wtccNiR	49
2.2.5. Mass Spectrometry for mass confirmation of wtccNiR	51
2.2.6. The standard ccNiR activity assay using the methyl viologen monocation radical	51
2.5 References.....	59
<i>Chapter 3 The test for hydroxylamine side product generation during ccNiR catalyzed reduction of nitrite under weakly reducing conditions</i>	
3.1. Overview.....	60
3.2. Materials and methods	61
3.2.1. General materials	61
3.2.2. General instrumentation.....	62
3.2.3. Preparation of reduced indigo trisulfonate	62
3.2.4. Johnson assay calibration curve	63
3.2.5. Johnson assay as a test for ccNiR-catalyzed hydroxylamine generation.....	65
3.3. Results and discussion of the Johnson assay	67
3.4 References.....	70
<i>Chapter 4 The quantification of ammonium present in solution after the ccNiR-catalyzed reduction of nitrite under weakly reducing conditions</i>	
4.1. Overview.....	71
4.2. Materials and Methods	73
4.2.1. General materials	73
4.2.2. General instrumentation.....	73
4.2.3. Calibration Curve	74
4.2.5. CcNiR-mediated reduction of nitrite in the presence of the various reducing agents.....	79
4.2.6. Ammonium assay for reaction products obtained under weakly reducing conditions	82
4.2.7. Analysis of the assay results	83
4.3. Results.....	86
4.3.1. I3S _{PR} as electron source	86
4.3.2. I3S _{FR} as an electron source	89
4.3.3. I3S _{FR} reduction of nitrite in the presence of the ccNiR variants R103Q and Y206F	90
4.3.4. I4S _{FR} as an electron source	93
4.3.5. Ru ^{II} as an electron source	94
4.4. Discussion	97
4.4.1. I3S as an electron source	97
4.4.2. I4S as an electron source.....	98
4.4.3. Ru ^{II} as an electron source	99
4.5. Summary	100
4.6 References.....	100
<i>Chapter 5 The search for the four electron reduced putative ccNiR intermediate using the stopped-flow technique</i>	
5.1. Overview.....	102
5.2. Materials and Methods	103
5.2.1. General materials	103
5.2.2. General instrumentation.....	103
5.2.3. Preparation of reducing agents	104
5.2.4. Preparation of the ccNiR/nitrite tonometers	104

5.2.5. Preparation of the I3S _{FR} Tonometers	104
5.2.6. Preparation of the I3S _{PR} Tonometer.....	105
5.2.7. Preparation of the I4S _{FR} Tonometers	105
5.2.8. Preparation of the MV _{red} Tonometer	105
5.2.9. Reduction of nitrite-loaded <i>S. oneidensis</i> ccNiR by various reductants: Stopped-flow experiments	106
5.3. Results and discussion	107
5.3.1. Partially Reduced I3S as the electron source	108
5.3.2. Fully Reduced I3S as the electron source	112
5.3.3. Fully Reduced I4S as the electron source	114
5.3.4. Reduced methyl viologen as the electron source	116
5.4 References.....	121
<i>Chapter 6 The Crystallographic Search for the Two Electron Reduced ccNiR Intermediate 123</i>	
6.1. Overview.....	123
6.2. Materials and methods	125
6.2.1. Formation of ccNiR microcrystals	126
6.2.2. Test for the catalytic activity of ccNiR microcrystals.....	126
6.2.3. Preliminary screening tests for and investigation of serial femtosecond X-ray crystallography ..	126
6.3. Results and Discussion	130
6.3.1. Catalytic activity of the ccNiR micro-crystals	130
6.3.2. Preliminary XFEL Investigation	130
6.4. References.....	131
<i>Chapter 7 Concluding Remarks</i>	
<i>7.1 References</i>	
<i>135</i>	

LIST OF FIGURES

- Figure 1.1 The nitrogen cycle, showing various enzyme-catalyzed pathways. **Purple:** Nitrogen fixation (Mo or Fe metal containing nitrogenase), **Red:** Dissimilatory nitrite reduction to ammonium (DNRA) (NaR: Mo containing nitrate reductase, ccNiR: *c*-heme containing cytochrome nitrite reductase), **Orange:** Assimilatory Ammonification (NaR: Mo containing nitrate reductase, CsNiR: siroheme containing nitrite reductase), **Green:** Denitrification, **Yellow:** Anaerobic ammonium oxidation (Anammox), **Light Blue:** Nitrification (AMO; ammonium monooxygenase, HAO: hydroxylamine oxidase). 3
- Figure 1.2 The homodimeric structure of *S. oneidensis* ccNiR. Each protomer contains five heme centers, heme#1 – heme#5. Electrons enter at Heme #2 (green). Heme# 1 (purple) is the active site in each protomer. The calcium ion is present twice in the dimer (left protomer; yellow sphere, right protomer; gray sphere). **B.** A closer depiction of the left protomer showing the substrate entry to Heme #1, and the exit of the product. The two funnel-like channels were drawn using free software Caver 3.0.3 plugin in PyMol (PDB 6P73). The green ball represents the entry of substrate following the path shown by the dashed black line. The blue ball shows the possible ammonium product release through the front side of the tunnel. **C.** The five ccNiR hemes of one protomer oriented based on the proximal and distal ligands. The histidine ligands are shown in blue, while the active site lysine is represented in yellow. **D.** A closer view of the *S. oneidensis* active site Heme #1 with the three conserved amino acid residues; H257, R103Q, and Y206F shown in red. All the hydrogen atoms are represented in green.⁶ 8
- Figure 1.3 Multiple sequence alignments of different ccNiR homologues. **Blue:** The conserved amino acid sequence for the *c*-heme motif (CXXCH). The lysine (K) residue of the active site heme is highlighted in yellow. **Red:** The histidine residues conserved in the distal site for the heme centers, which conclude the bis-his ligated heme center. A **brown arc** focuses the fixates on a misalignment in the sequence for the *G. lovleyi* ccNiR, which contains R122. **Green:** Amino acids outside of the active site that are not structurally or catalytically active, thus far. **Red Highlight:** A methionine (M255) in place of the usual tyrosine in *G. lovleyi* ccNiR. The function remains unclear. The *G. lovleyi* ccNiR also has an arginine (R277) next to the active site histidine instead of a glutamine residues that is seen in other 14

	homologues ⁶ .histidine instead of a glutamine residues that is seen in other homologues ¹ .	
Figure 1.4	The arrangement with the ccNiR dimer of <i>S. oneidensis</i> . The protomers are separated by a black dotted line. Electrons are donated from CymA (shown in brown), entering through Heme #2. The electrons are then shuttled to Heme #3, with the predicted pathway of electron transfer shown in red. Heme #3 (blue), Heme #4 (cyan), and Heme #5 (orange) are the bis-histidine ligated electron transferring hemes (six-coordinate).The five-coordinate active site Heme#1 has the CXXCK motif, containing the Lysine and an open distal site for substrate binding. ^{257, 16, 29} in <i>W. succinogenes</i> they are Arg-114, Tyr-218, and His-277, and in <i>S. deleyianum</i> they are Arg-113, Tyr-217, His-282. ³⁶	17
Figure 1.5	The possible modes of nitrite bound to iron.	24
Figure 1.6	The back-bonding interaction between the active site heme of ccNiR (in the ferrous state) and the physiological substrate nitrite. The d_{xz} orbital of iron interacts with the NO_2^- lowest unoccupied molecular orbital (LUMO) of NO_2^- , which has an antibonding character with respect to the N-O bond. ⁶	25
Figure 1.7	Cartoon representation of the ccNiR-catalyzed nitrite reduction path proposed on the basis of experimental and theoretical data available at the start of the project described in this thesis.	36
Figure 2.1	Large scale (45 L) <i>Shewanella oneidensis</i> culture for high amount wtccNiR enzyme purification. A carboy used for this culture was surrounded by water. A thermostat maintains the constant optimum temperature (30 °C). To keep the culture aerated and to avoid cell settling, two fritted sparging tubes inside of the carboy provided compressed air circulation that continuously agitated the culture.	46
Figure 2.2	SDS-PAGE gel of various samples of purified, wild type ccNiR. Each lane consists of a sample of purified protein from individual 50 L cultures utilized for crystallography, with a molecular weight ladder in the left most lane.	50
Figure 2.3	The spectrum in red represents the mass spectrum up to 800 m/z. The spectrum in blue shows the full spectrum up to 150,000 m/z. Both spectra show a peak around 52,000 -53,000 m/z, which confirms the mass of a ccNiR protomer. The full spectrum shows a peak at ~125,000 m/z, which corresponds to the mass of the ccNiR dimer. This confirms the presence of ccNiR in the sample.	52
Figure 3.1	Spectra of the reaction mixtures containing a 1µM ccNiR, 60µM partially reduced Indigo trisulfonate, and 500µM Nitrite, with a known amount of hydroxylamine at concentrations ranging from 100-500µM.	65

Figure 3.2	A comparison of the standard curve to the linear fit of the reaction mixtures.	66
Figure 4.1	Spectral trace at 342nm corresponding to the oxidation of NADH to NAD ⁺ over time.	72
Figure 4.2	NADH spectral changes observed over the course of 15 minutes for the 40μM ammonium standard.	77
Figure 4.3	Spectral changes observed at t = 0 (red) and t = 450s (blue) for a solution containing 40μM ammonium standard solution and also oxidized I3S. Changes in the 340 nm range correspond to the decrease in absorbance as NADH is consumed, but for complex mixtures such as this one, it is advisable to fit the entire spectrum as described in section 4.2.7, rather than a single wavelength, as in Fig. 4.1.	77
Figure 4.4	The calibration curve produced from measuring the change in NADH concentration over time for standards ranging from 2-80μM ammonium. The linear fit is shown in red.	87
Figure 5.1	Spectral changes observed after mixing ~1 μM ccNiR and 500 mM nitrite with 80 μM I3S _{PR} .	109
Figure 5.2	Absorbance vs time traces at specific wavelengths obtained from the Fig. 5.2 data.	110
Figure 5.3	Spectral component that was present at t = 0 after mixing ~1 μM ccNiR and 500 mM nitrite with 80 μM I3S _{PR} .	110
Figure 5.4	Spectral component that grew in with a half-life of 111 ms after mixing ~1 μM ccNiR and 500 mM nitrite with 80 μM I3S _{PR} .	111
Figure 5.5	Spectral component that grew in with a half-life of 4.8 s after mixing ~1 μM ccNiR and 500 mM nitrite with 80 μM I3S _{PR} .	111
Figure 5.6	Spectral component that grew in ~1 s with I3S _{FR} at varying concentrations, ~1 μM ccNiR and 500 mM nitrite.	113
Figure 5.7	Rate constant $k_{I_{obs}}$ for the reactions described in Figure 5.6.(Linear fit shown as a solid red line.)	113
Figure 5.8	Spectra extracted at different timescales from the reaction of 10 μM I4S, 2 μM ccNiR, and 500 mM Nitrite produced from a UV-visible spectrophotometer run on cycle mode.	115
Figure 5.9	Spectral changes observed in the first 20 ms after mixing ~1 μM ccNiR and 500 mM nitrite with 200 μM methyl viologen monocation radical (MV _{red}).	117
Figure 5.10	Spectral changes observed between 20 ms and 10 s after mixing ~1 mM ccNiR and 500 mM nitrite with 200 μM methyl viologen monocation radical (MV _{red}). The dotted red curves are the fits obtained with the Scheme 4.2 model.	118
Figure 5.11	Spectral traces observed after mixing ~1 μM ccNiR and 500 mM nitrite with 200 μM methyl viologen monocation radical (MV _{red}). The dotted red curves are the fits obtained with the Scheme 4.2 model.	118

Figure 5.12	UV/Vis absorbance spectrum taken after 30 ms from the Fig. 5.10 data set. The spectrum shows extensive bis-His heme reduction.	119
Figure 5.13	The fifth spectral component obtained in the fit of the stopped-flow data presented in Fig. 5.10 with the Scheme 5.2 model. This component appears with a half-life of ~170 ms.	119
Figure 5.14	The sixth spectral component obtained in the fit of the stopped-flow data presented in Fig. 5.10 with the Scheme 5.2 model. This component appears with a half-life of ~6.5 s.	120
Figure 6.1	A schematic representation of ccNiR microcrystals flowing through the injector to be struck by the X-ray beam. A diffraction pattern is created on the detector and later used to obtain a crystal structure.	125
Figure 6.2	A representation of the catalytic activity of ccNiR microcrystals. The linear fit is shown in red. The activity of the crystals increases with increasing crystal number density.	127
Figure 6.3	Crystal preparation viewed in a Neubauer counting chamber. In addition to crystals, amorphous debris is present.	128
Figure 6.4	SONICC signal of ccNiR microcrystals.	129
Figure 6.5	A. Crystal lattice. B. Electron diffraction using Micro-ED.	129
Figure 6.6	Diffraction patterns of microcrystals beyond the water ring.	131

LIST OF TABLES

Table 2.1	A comparison of the k_{cat} values for different protein purifications of the <i>S. oneidensis</i> ccNiR, as well as the <i>D. desulfuricans</i> ccNiR provided by the Almeida Group.	58
Table 3.1	The final concentration of hydroxylamine calculated to be present in the standards and the spiked reaction mixtures. The absorbances for the standards and the reaction mixtures are listed in the table and correspond to those plotted in Figure 3.2.	67
Table 3.2	T-test table.	69
Table 4.1	Volumes of each stock solution used to make reaction mixtures with varying concentrations of I3S _{FR} . The concentrations of ccNiR and nitrite are constant at 1.5 mM and 500 mM, respectively, in all reaction mixtures. The total volume of each reaction mixture was 1.0 mL.	80
Table 4.2	Volumes of each stock solution used to make reaction mixtures with varying concentrations of Ru ^{II} . The concentrations of ccNiR and nitrite are constant at 1.5 mM and 500 mM, respectively, in all reaction mixtures. The total volume of each reaction mixture was 1.0 mL.	81
Table 4.3	Replicated experiments of the ccNiR-catalyzed reduction of nitrite in the presence of partially reduced Indigo trisulfonate.	88
Table 4.4	The calculated ammonium formation for the ccNiR-catalyzed reduction of nitrite in the presence of fully reduced indigo trisulfonate at concentrations ranging from 45-120 μM. The experiments were reproduced five times.	89
Table 4.5	The calculated percent ammonium formation for the ccNiR-catalyzed reduction of nitrite in the presence of fully reduced indigo trisulfonate at concentrations ranging from 45-120 μM for Dataset 1 from Table 4.4.	90
Table 4.6	The calculated ammonium formation for the R103Q ccNiR variant -catalyzed reduction of nitrite in the presence of fully reduced Indigo trisulfonate at concentrations ranging from 45-120 μM. The experiments were reproduced in triplicate.	91
Table 4.7	The calculated percent ammonium formation for the R103Q ccNiR variant -catalyzed reduction of nitrite in the presence of fully reduced Indigo trisulfonate at concentrations ranging from 45-120 μM for Dataset A from Table 4.6.	91
Table 4.8	The calculated ammonium formation for the Y206F ccNiR mutant-catalyzed reduction of nitrite in the presence of fully reduced Indigo trisulfonate at concentrations ranging from 45-120 μM. The experiments were reproduced in triplicate.	92

Table 4.9	The calculated percent ammonium formation for the Y206F ccNiR mutant-catalyzed reduction of nitrite in the presence of fully reduced Indigo trisulfonate at concentrations ranging from 45-120 μ M for Dataset A from Table 4.6.	92
Table 4.10	The calculated ammonium formation for the ccNiR-catalyzed reduction of nitrite in the presence of fully reduced indigo tetrasulfonate at concentrations ranging from 45-120 μ M. The experiments were reproduced in triplicate.	93
Table 4.11	The calculated percent ammonium formation for the ccNiR-catalyzed reduction of nitrite in the presence of fully reduced indigo tetrasulfonate at concentrations ranging from 45-120 μ M for Dataset 2 from Table 4.10.	94
Table 4.12	The calculated ammonium formation for the ccNiR-catalyzed reduction of nitrite in the presence of fully reduced hexaammineruthenium at concentrations ranging from 10-80 μ M. The experiments were reproduced in triplicate.	96
Table 4.13	The calculated ammonium formation for the ccNiR _{R103Q} variant-mediated reduction of nitrite in the presence of fully reduced hexaammineruthenium at concentrations ranging from 10-80 μ M. The experiments were reproduced in triplicate.	96
Table 4.14	The calculated ammonium formation for the ccNiR _{R103Q} variant-mediated reduction of nitrite in the presence of fully reduced hexaammineruthenium at concentrations ranging from 10-80 μ M. The experiments were reproduced in triplicate.	97

LIST OF SCHEMES

Scheme 1.1	Enemark – Feltham notation used to represent iron nitrosyl species for which the electron distribution is uncertain.	29
Scheme 1.2	Some of the catalytic steps proposed for the reduction of nitrite to ammonia at the ccNiR active site, based on computational analysis. ^{17, 18} The heme-bound nitrosyl species are represented by their Enemark-Feltham notations (Scheme 1.2). When present in protonated form, the catalytically important conserved active site amino acids are labeled as follows (using <i>S. oneidensis</i> numbering): Y _H , Tyr-206; R _H , Arg-103; H _H , His-257; and H ₀ -where His-257 is not in a protonated form. This shorthand is adapted from that used by Bykov and Neese, ¹⁸ but with some modifications. PCET: <u>P</u> roton <u>C</u> oupled <u>E</u> lectron <u>T</u> ransfer.	30
Scheme 3.1	The reaction between hydroxylamine and p-nitrobenzaldehyde to form the oxime product measurable by UV-Visible Spectrophotometry.	61
Scheme 3.2	Equations used to complete a t-test. A. The t_{calc} value obtained by evaluating the means of two data sets, the number of values in each data set, and the S_{pooled} value. B. The S_{pooled} value obtained from the standard deviations of the two data sets, the number of values in the data set, and the degrees of freedom.	61
Scheme 3.3	Half-reactions for nitrite oxidation to hydroxylamine and I3S _{red} oxidation, and the net reaction for nitrite reduction to hydroxylamine by I3S _{red} . The reactions show that 2 equivalents of I3S _{red} are required to reduce one equivalent of nitrite to hydroxylamine.	68
Scheme 3.4	Equations used to complete a t-test. A. The t_{calc} value obtained by evaluating the means of two data sets, the number of values in each data set, and the S_{pooled} value. B. The S_{pooled} value obtained from the standard deviations of the two data sets, the number of values in the data set, and the degrees of freedom.	69
Scheme 4.1	The six electron reduction of nitrite to ammonium catalyzed by ccNiR in the presence of a weak reductant. B. The glutamate dehydrogenase catalyzed reduction of α -ketoglutarate to glutamate using NADH as an electron donor. NADH oxidation to NAD ⁺ can be correlated with the concentration of ammonium in solution.	72
Scheme 4.2	Equation used to fit the spectral changes associated with NADH oxidation in the presence of other absorbing species such as ccNiR and I3S or I4S.	85
Scheme 4.3	Stoichiometry for the reaction of I3S with nitrite to produce ammonium. I4S would have the same stoichiometry,	87

	whereas Ru^{II} is a 1-electron donor, so 6 equivalents are required to reduce nitrite to ammonium.	
Scheme 5.1	Kinetic model used for fitting of the I3S _{PR} data and the observed rate constants k_{1app} and k_{2app} .	109
Scheme 5.2	The differential equations that were applied to analyze the ccNiR-mediated reduction of nitrite using the strong reductant MV_{red} .	116

LIST OF ABBREVIATIONS

Where possible all abbreviations used are those recommended in “ACS Guide to Scholarly Communication” Section 5.3.8.

ccNiR	Cytochrome <i>c</i> nitrite reductase
I3S	Indigo trisulfonate
I4S	Indigo tetrasulfonate

ACKNOWLEDGEMENTS

First and foremost, I would like to thank my supervisor, Professor A. Andrew Pacheco. Six years ago, he gave me the opportunity to be his laboratory technician and later I became his graduate student, despite my little knowledge of biological sample handling. He put his faith in me and with constructive criticism and support, I was able to broaden my abilities in ways that I never imagined possible for myself. Thank you for taking the chance on me and allowing me to prove I was worthy of that. I am forever grateful for all the encouragement and guidance over these years.

I would like to thank my husband and lab member Alexander Drena for the constant support over the last five years. I am incredibly grateful for having you as a sounding board anytime I wanted to discuss research. Also, I would like to express my utmost gratitude for your contribution to the XFEL sample preparation. If you had not grown up ten 50L preps of bacteria for me to purify ccNiR, I would have never met my deadline. Thank you for being the better half of our team. It is an honor to be able to walk across the stage with you on graduation.

I would like to extend my gratitude to my committee members, who have provided me with great feedback on my research. Professor Shama Mirza enriched me with knowledge of mass spectrometry and assisted me in using MALDI-TOF. Professor Joseph Aldstadt helped to improve my analytical understanding, whereas Professor Nicholas Silvaggi directed me in “black magic” of protein crystallography. Professor Jarett Wilcoxon allowed me to use his stopped-flow instrument and guided me anytime I ran into unusual research problems. I would like to give a special thank you to Professor Mark Dietz. Before he was my committee member, he was my supervisor for undergraduate research. I will always cherish the two years I spent researching in his laboratory. With his guidance and support, my undergraduate research resulted in two

publications. Thank you for taking me in your lab (even though I was not a standout student at the time) and contributing to my success as a scientist.

Thank you to my lab members: Dr. Shahama Alam, Steven Reinhardt, Dr. Shahid, and Dr. Mahbbat Ali for all of your contributions to the ccNiR project that allowed me to help further the project. A special thank you to Dr. Shahid who gave me permission to use his images, which are shown in Figures 1.2-1.4, and 1.6. Thank you to the newer graduate students Shabnam Marium, Sharmin Shampa, Bradley Dimock, Stephen Nkwocha, and Joseph Oke for coming to the Pacheco lab and for the effort you all will put into future research. I would like to extend my gratitude to my friends either in or formerly in the department: Dr. Tania Mutchie, Dr. Trevor Melkonian, Jon Mielke, Dr. Jennifer McGarry, and Nicholas Hopper for all of the advice and guidance during my Ph.D.

I am very grateful to Professor Marius Schmidt, Dr. Srinivasan Muniyappan, and Tek Malla from the UW-Milwaukee Physics Department for their collaboration with the crystallographic search of intermediates using the XFEL. I enjoyed working with each one of you and appreciate your contributions in making this project successful.

Last but certainly not least, I would like to thank my parents for the unconditional love and support that I needed during the last 10 years. They helped me through my undergraduate degree, and then through my graduate degree. I will never be able to express how grateful I am for the constant guidance during a difficult and challenging time. I would like to show my deep appreciation to my sister, brother-in-law, nephew, niece, my extended family, and all my friends who provided me with love and support.

Finally, I would like to acknowledge the support I received from the National Science Foundation (MCB-1616824 and MCB-2032265) throughout my time as a graduate student. Also,

a special thank you to the Shimadzu laboratory at UW-Milwaukee for the assistance with the mass spectrometers.

Chapter 1 Introduction

1.1. The importance of nitrogen

Nitrogen is an element that is important to all living things. It is found in animals, plants, soil, water, and air. Around 78% of the Earth's atmosphere is nitrogen. It is one of the key elements in nucleic acids, DNA and RNA, which are present in all living things and form the genetic blueprint of a lifeform. Organisms need nitrogen to produce amino acids in order to make proteins necessary for proper function. For example, when a plant is lacking nitrogen, the plant DNA cannot produce the proteins necessary for the plant cells to grow, and such deficiencies can have detrimental effects.¹

As described in the previous paragraph, one of the key roles of nitrogen is in plant growth. When there is too little nitrogen available to plants, this can lead to a low crop yield, meaning there is less food to feed all of the lifeforms on the planet.² When there are low levels of nitrogen in soil, farmers tend to add fertilizer to aid in the growth of the plants. There are two main problems that can arise when fertilizer is overused. There is the effect on soil, as well as the effect on ground water. An excess of nitrogen in the soil can lead to the plants' inability to form strong roots and an overgrowth of biomass, such as stalks and leaves, inhibiting the strength of the plant. Another issue that occurs due to high nitrogen levels is the poisoning of the animals that consume the plants.³

Overuse of fertilizer can also affect aquatic life. When too much nitrogen is present in soil, it can leach into nearby bodies of water. This results in the overgrowth of algae into algal blooms. When algae overgrow, a barrier is created on the surface of the water. Sunlight can no longer penetrate below the surface, which leads to the decrease of different organisms below the

surface, especially the ones that need sunlight to perform photosynthesis to grow. Alternatively, when algae die off, microbes in the water decompose them, which in turn, consumes a lot of the oxygen in the water. Lack of oxygen causes organisms to die, leading to dead zones, which is especially impactful on bigger organisms such as fish. Fertilizer runoff can also affect animals or people that drink the water.¹ Finally, excess nitrogen causes overgrowth of cyanobacteria and other organisms that are toxic when consumed. For all these reasons, an in depth understanding of the global nitrogen cycle, which could lead to better use of fertilizer, is critical in order to help plan for and mitigate changes that could threaten ecological balance.

1.2. What is the nitrogen cycle?

The nitrogen cycle is one of the many important biological cycles on Earth. It is a cyclical process in which nitrogen interconverts between different species that are distributed in living and non-living things such as soil, water, plants, animals, and bacteria. Figure 1.1 outlines the different nitrogen species that make up the nitrogen cycle. Most terrestrial nitrogen is in the form of dinitrogen (N_2). The form of nitrogen that is most directly usable by organisms is ammonium (NH_4^+), though nitrate (NO_3^-) is typically more abundant, and plants, bacteria and fungi can often convert nitrate to ammonium. When fertilizer is used, nitrogen is found as ammonia (NH_3), ammonium nitrate (NH_4NO_3), or other ammonium salts.

There are five stages to the nitrogen cycle: nitrogen fixation, mineralization, nitrification, immobilization, and denitrification. This cycle is crucial to biological life and requires balance in order to conserve ecosystems. Nitrogen fixation is the stage in which atmospheric nitrogen is transferred from the air to the soil. As previously stated, most of the nitrogen available on Earth

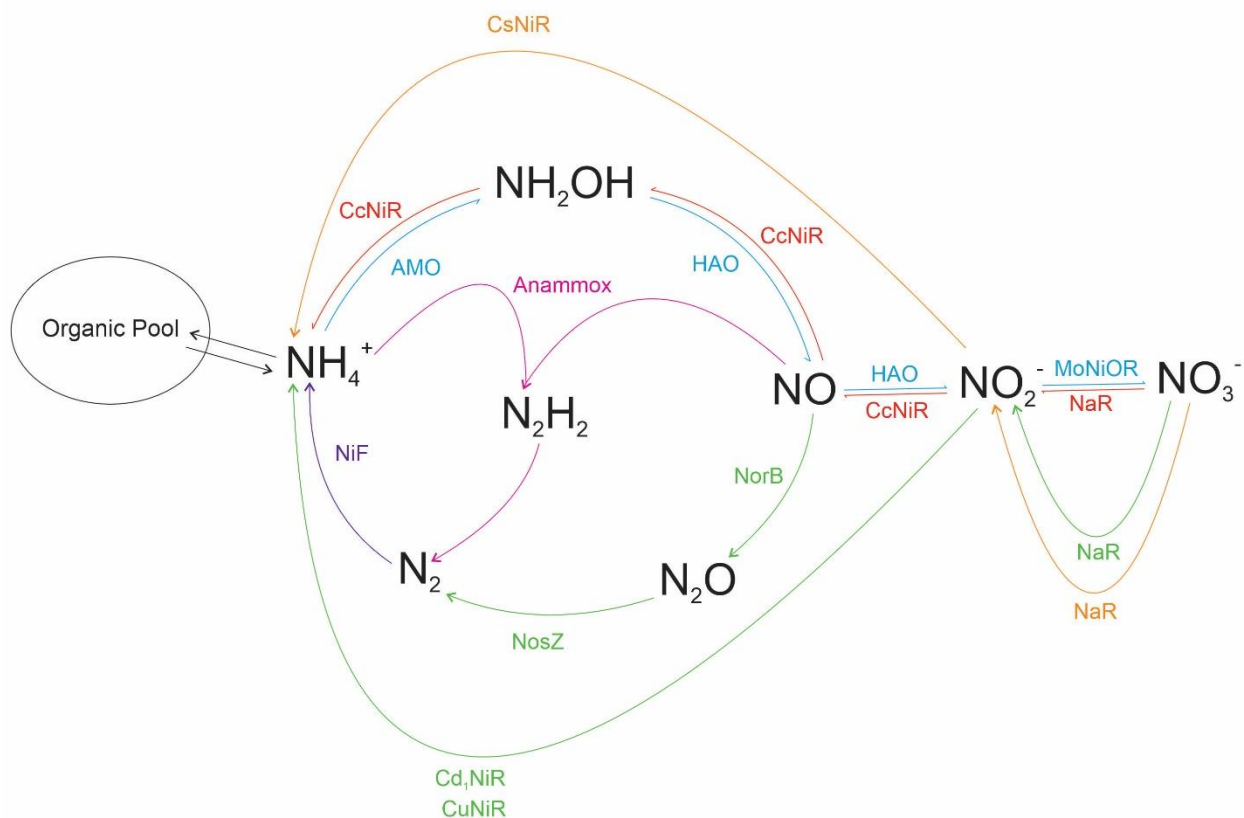


Figure 1.1. The nitrogen cycle, showing various enzyme-catalyzed pathways. **Purple:** Nitrogen fixation (Mo or Fe metal containing nitrogenase), **Red:** Dissimilatory nitrite reduction to ammonium (DNRA) (NaR: Mo containing nitrate reductase, ccNiR: *c*-heme containing cytochrome nitrite reductase), **Orange:** Assimilatory Ammonification (NaR: Mo containing nitrate reductase, CsNiR: siroheme containing nitrite reductase), **Green:** Denitrification, **Yellow:** Anaerobic ammonium oxidation (Anammox), **Light Blue:** Nitrification (AMO; ammonium monooxygenase, HAO: hydroxylamine oxidase).

is present in the atmosphere as dinitrogen. Dinitrogen is a gaseous form of nitrogen that is unusable to most forms of life. Therefore, the conversion to more usable forms of nitrogen is very important in the balance of an ecosystem. There are three possible ways for nitrogen fixation to occur. The first is that lightning must strike the air, causing a reaction between dinitrogen and oxygen. This reaction will then produce nitric oxide or nitrogen dioxide, which can then enter to soil by either rainwater or snow.⁴ The second way for nitrogen to be fixed is industrially via the Haber-Bosch process, where high heat and pressure are applied to atmospheric nitrogen and hydrogen, thus forming ammonia. Ammonia can be further processed into ammonium nitrate, which is then added to soil. The third, and until recently the most common, way that nitrogen is fixed is by nitrogen-fixing bacteria living in the soil. Many of these bacteria get energy from photosynthesis and can convert nitrogen into usable forms for the plant to absorb through its roots in the soil. Mineralization occurs when either manure is in the soil or plant materials have decomposed, and nitrogen moves from this organic material into inorganic nitrogen forms. This process can proceed due to microbes in the soil completing this conversion. The result of this conversion is ammonia, that upon addition of water, can be converted into ammonium and used by other plants. Nitrification occurs when the ammonium in the soil is converted into nitrites and nitrates by some bacteria such as *Nitrosomonas sp.* Nitrate is usable by plants and some bacteria and fungi that can convert it back to ammonium. Furthermore, many plants have a siroheme-based nitrite reductase that converts nitrite to ammonium like ccNiR does. Immobilization is the fourth stage of the nitrogen cycle and is often referred to as reverse mineralization. Both plants and microbes need nitrogen species in order to function. Problems can arise when organic materials that are placed in the soil for decomposition are limiting in nitrogen, thus increasing the C/N, or carbon to nitrogen ratio. When this ratio is

high, microorganisms that need nitrogen scavenge and store all the inorganic nitrogen in the soil. The final step of the nitrogen cycle is denitrification, where microbes reduce nitrate in the soil back to dinitrogen in the atmosphere. This occurs stepwise via nitrite, nitric oxide, and nitrous oxide.

1.3. The importance of nitrite in the nitrogen cycle

One of the extraordinary points described in the previous section is the interconversion of nitrogen species by bacteria. Specifically, looking at nitrification, it is known that ammonia can be converted to nitrite by *Nitrosomas*, then further converted to nitrate by *Nitrobacter*.⁵

Although there are many nitrogen species in the nitrogen cycle, nitrite plays a central role. Nitrite can undergo reduction to either ammonia or dinitrogen, or oxidization to nitrate, in processes catalyzed by various biological enzymes. Ammonia and nitrates can be found in the environment; however, problems can arise when the accumulation of these nitrogen species lead to eutrophication in aquatic environments. Energy conservation and balancing eutrophication in the environment, among other things, is of high interest to ecologists and microbiologists. Biological nitrite reduction can play a pivotal role in this environmental regulation.⁶

The reduction of nitrite can occur in two ways. The first way is by assimilatory nitrite reduction, where nitrite is reduced to ammonium for incorporation into biomass. This assimilatory process is found in plants, fungi, and bacteria. Assimilatory nitrite reduction is catalyzed by either NAD(P)H- or ferredoxin-dependent cytoplasmic siroheme-containing nitrite reductases (CsNiR).⁷⁻⁹ The second way in which nitrite can be reduced is by dissimilatory nitrite reduction. Bacteria are able to carry out dissimilatory nitrite reduction as an anaerobic respiratory process for which the product can be dinitrogen (respiratory denitrification) or ammonium

(respiratory nitrite ammonification).^{7, 8, 10} However, during anaerobic respiration, both dinitrogen and ammonium are never produced concurrently.¹¹

1.4. Metalloenzymes and their relationship to the nitrogen cycle

Metalloenzymes are fundamental to both assimilatory and dissimilatory processes; indeed, they are involved in every step of the nitrogen cycle. The first step in respiratory denitrification is the reduction of nitrite to nitric oxide ($\text{NO}\cdot$), which can either be catalyzed by an enzyme called cytochrome *cd1* nitrite reductase, or by a copper-containing nitrite reductase. Another enzyme called NO reductase aids in the reduction of $\text{NO}\cdot$ to nitrous oxide (N_2O), which is then reduced by N_2O reductase to dinitrogen (N_2). Nitrite reductases, NO reductase, and N_2O reductase are all metalloenzymes. The complete denitrification process converts the more reactive nitrogen species, that are universally bioavailable, into dinitrogen. Dinitrogen, as mentioned previously in this chapter, is the largest terrestrial nitrogen source, but is only able to be used by a handful of prokaryotes that express the nitrogen-fixing enzyme nitrogenase (NiF). Nitrogenase is a metalloenzyme that reduces dinitrogen to the reactive nitrogen species ammonium, making nitrogen bioavailable for non-nitrogen fixing organisms, which are the vast majority.⁶

Although ammonium is directly incorporated into the biomass, nitrate is the main source of reactive nitrogen in the biosphere, as well as being the less toxic nitrogen species. Nitrate is converted to nitrite by molybdenum-containing enzymes referred to as Nitrate reductases. Nitrite can be further converted to ammonium for incorporation into the biomass by either the assimilatory or dissimilatory nitrite reduction pathway, as described earlier in this section.¹²

Cytochrome *c* nitrite reductase (ccNiR, also called NrfA after the *nrfA* gene that codes for it), depicted in Fig. 1.2, is the main enzyme in the dissimilatory nitrite reduction process, which is also referred to as the nitrite ammonification pathway. Under standard assay conditions *in vitro*, ccNiR converts nitrite to ammonium, without the release of any potential toxic intermediates. Nitrite is not the only *in vitro* terminal electron acceptor in this reduction process though. Other nitrogenous molecules, such as nitric oxide and hydroxylamine, can be reduced to ammonium by ccNiR. Over the past 20 years, various groups have provided interesting results relating to ccNiR.¹³⁻¹⁵

The focus of this thesis is to explore the mechanism of the ccNiR-catalyzed reduction of nitrite to ammonium and examine the possibility of toxic side product formation during nitrite reduction. As mentioned above, no side products or reaction intermediates are generated *in vitro* under standard assay conditions (described below in Section 1.11). However, as will be seen in Section 1.11, the Pacheco group has, over the past 8 years, shown that transient reaction intermediates can be detected under weakly reducing conditions. Earlier studies conclusively identified nitrite-loaded 1-electron and 2-electron reduced intermediates, and also showed that small quantities of NO \cdot are generated when ccNiR catalyzes reduction of nitrite by very weak reductants such as ferrocyanide.^{16, 17} This thesis explores the possibility of generating 4-electron reduced intermediates under conditions that are more weakly reducing than used in the standard assay but more strongly reducing than used earlier by the Pacheco group. In addition, the thesis also describes experiments to quantify the amount of ammonium and hydroxylamine generated during ccNiR-catalyzed reduction of nitrite by weak reductants, where hydroxylamine is a possible side-product of partial nitrite reduction (Fig. 1.1). The ccNiR used for the studies

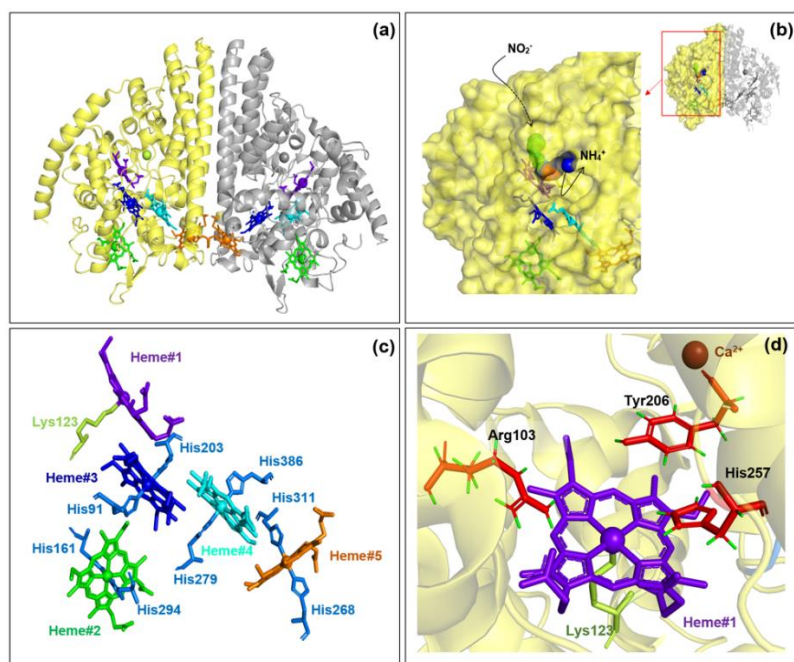


Figure 1.2. A. The homodimeric structure of *S. oneidensis* ccNiR. Each protomer contains five heme centers, heme#1 – heme#5. Electrons enter at Heme #2 (green). Heme# 1 (purple) is the active site in each protomer. The calcium ion is present twice in the dimer (left protomer; yellow sphere, right protomer; gray sphere). **B.** A closer depiction of the left protomer showing the substrate entry to Heme #1, and the exit of the product. The two funnel-like channels were drawn using free software Caver 3.0.3 plugin in PyMol (PDB 6P73). The green ball represents the entry of substrate following the path shown by the dashed black line. The blue ball shows the possible ammonium product release through the front side of the tunnel. **C.** The five ccNiR hemes of one protomer oriented based on the proximal and distal ligands. The histidine ligands are shown in blue, while the active site lysine is represented in yellow. **D.** A closer view of the *S. oneidensis* active site Heme #1 with the three conserved amino acid residues; H257, R103Q, and Y206F shown in red. All the hydrogen atoms are represented in green.⁶

presented in the upcoming sections was sourced from the bacterium called *Shewanella oneidensis*, so a brief introduction to this bacterium is presented in the next section.

1.5. *Shewanella Oneidensis* MR-1

Shewanella oneidensis is a proteobacterium with highly versatile respiration abilities, as well as great potential for bioremediation applications, which makes it quite interesting to study. A *Shewanella* species was first discovered in putrid butter, along with other forms of bacteria. After further investigation, it was found that *Shewanella* is a rod-shaped bacterium with a polar-type flagella, allowing it to swim around through marine sediment and soil. A single bacterium is 2-3 μm in length, and 0.4-0.7 μm in width.¹⁸ Originally, *Shewanella* were classified under the *Achromobacter* genus,¹⁹ however, they were later reclassified under a new genus name of *Shewanella*, after the renowned marine microbiologist, Dr. James M. Shewan.²⁰ The species referred to as *S. oneidensis* was discovered when a group of scientists were studying the aquatic life in Lake Oneida. Upon their investigations, they found a large amount of reduced manganese (Mn^{2+}) with a comparatively lower amount of oxidized manganese (Mn^{4+} as MnO_2). Interestingly, this was unexpected due to the natural aeration of the water. After performing DNA hybridization and 16S rRNA sequencing studies, the evidence presented a new metal-reducing species that could be classified under *Shewanella* bacteria. This new species was named *Shewanella oneidensis*, coined from the lake in which it was discovered. Since *S. oneidensis* has a manganese reducing property (due to the high levels of Mn^{2+} found in the water of Lake Oneida), the suffix MR-1 was added to signify the manganese- or metal-reducing property of the bacteria. This particular *Shewanella* species is very adaptable in anaerobic respiration; specifically, *S. oneidensis* can reduce a wide variety of inorganic, organic, soluble, and non-soluble compounds, using them as terminal electron acceptors. Besides reduction of manganese,

these bacteria can reduce, among other compounds, iron, dimethyl sulfoxide, dioxygen, and uranium during anaerobic respiration.¹⁹

The *S. oneidensis* MR-1 species was the first in the *Shewanella* genome to be sequenced. *S. oneidensis* contains 39 cytochrome *c* genes, and 14 of these genes encode for multi-heme proteins containing at least four hemes. This makes *S. oneidensis* one of the most prolific producers of *c*-type hemes in nature, second only to *Geobacter sulfurreducens*, that currently holds the record at 111 cytochrome *c* encoding genes. Out of these, 73 genes encode for at least two heme groups per protein.^{21, 22} The *c*-heme count is based on identifying the *c*-heme attachment motif, CXXCH, as not all the *c*-hemes in *S. oneidensis* (or *G. sulfurreducens*) have been purified and characterized. The multi-heme enzymes in *S. oneidensis* and *G. sulfurreducens* play essential roles in providing allow organisms with the capability of using a broad range of substrates for respiration.²¹⁻²³ The Pacheco group's main reason for choosing *S. oneidensis* as a ccNiR source was it's ability to readily produce large quantities of the enzyme under both aerobic and anaerobic conditions.

1.6. Hemes

Hemes are prosthetic groups found in living cells. The roles that they play include electron transfer, energy metabolism, catalysis, and small molecule transport.²⁴ A heme contains a central iron with four nitrogen donor atoms coordinated equatorially from a macrocyclic porphyrin ligand. Hemes tend to have ligands bound to the iron axial sites. The function of a variety of heme proteins or enzymes can be correlated with the arrangement of the porphyrin ring, in conjunction with the axial ligand arrangement. For example, hemes that are involved in electron transfer are usually six-coordinate, with two amino acid ligands bound to the axial positions of the iron.^{25, 26} Commonly, in electron transfer heme proteins, the amino acid residues

will be histidine or methionine. When both the proximal and distal sites are occupied, the heme is considered to be “closed”. By contrast, a penta-coordinated heme is said to be “open” because the open distal site allows for substrate binding to occur. In this case, histidine or another residue is bound in the proximal site, leaving the open site available for small molecules, such as oxygen, to bind. Generally, the role of a protein with this type of heme structure will be small molecule transport. In contrast, a closed heme does not necessarily remain closed. The closed heme can become open when a weakly-held proximal ligand such as water leaves which allows it to be displaced by a substrate. Once a substrate ligand is bound, oxidoreductase reactions can occur.²⁶ Various examples of weak distal ligand coordination are demonstrated by Cd1NiR, bacterial cytochrome *c* peroxidase, Neuroglobin (Nb), or Cytochrome *b₅*.²⁷ In these cases, the distal ligand is often an amino acid from the protein backbone.

The nature of the proximal site ligand is often important in dictating heme reactivity. CytP450 and NO synthase are examples of enzymes that have hemes containing cysteine amino acids in the proximal site, whereas peroxidases have histidine, and catalase contains tyrosine.²⁸ Unusually, CcNiR, the subject of this thesis, has a lysine ligand in the proximal site.^{16,29} It is also worth noting that, when looking at nitrite reduction, the nitrite ammonifying ccNiR has the lysine as the proximal ligand, whereas the NO-producing *cd1* type heme (Cd1NiR) has histidine in the proximal site.³⁰

1.7. Cytochromes

Cytochromes are a class of heme proteins involved in electron transport, as well as oxidation-reduction processes. Cytochromes are quite prevalent in the biosphere as electron transport proteins. In the process of respiration, cytochromes are among the primary electron transporting molecules. Cytochromes are very versatile, due to the vast tunability of hemes

within the structure, as well as the various oxidation states accessible to iron, which include the oxidized Fe^{3+} , reduced Fe^{2+} , and the possible Fe^{4+} forms of iron present in catalytic intermediates.

Cytochromes were initially classified into groups *a-c* by entomologist David Keilin. This classification was based on the differences in the lowest energy absorption band position in the reduced state of the various heme types. For cytochrome *a*, the lowest energy band is found at around 605 nm, in contrast to the lowest energy band absorption of cytochrome *b* and cytochrome *c*, which are found at 565 nm and 550 nm, respectively.³¹ Subsequently, cytochrome *d* was added to the classification,³¹ and more recently cytochrome *o*³² and cytochrome *P450*, and many others have joined the cytochrome family. The spectroscopic properties of cytochromes correlate with the chemical properties of the heme prosthetic group. This will be further described in the next section, specifically for the case of cytochrome *c*.

Nearly 80% of the total outer membrane protein composition in *S. oneidensis* is composed of cytochrome *c* proteins, due to the metal-reducing properties of these proteins.³³ What makes cytochrome *c* proteins unique is that they contain *c*-type hemes. Of the various types of hemes, the *c*-type heme structure is unique because of the capability of the porphyrin rings to covalently bind to the protein backbone. This is in contrast to the other hemes, which are held in place by non-covalent interactions, as well as by the interactions between one, or possibly both of the iron axial sites with the amino acid residues from the protein backbone. Heme *c* covalently binds to the protein backbone via two thioether bonds. Moreover, the bond formation region of the amino acid sequence in the cytochrome *c* family is specifically encoded by the motif CXXCH, where C represents the amino acid cysteine, X symbolizes any amino acid residue, and H is for Histidine. Figure 1.3 compares ccNiR sequences from various bacteria,

highlighting their CXXCH sequences. The thioether bonds between the backbone and the c-type heme are formed by covalent bonding between the sulfur atoms from the two cysteine residues and the two vinyl groups from the porphyrin ring. The histidine ligand from the CXXCH sequence binds to one of the axial sites on the heme iron.

Over one hundred years ago, mammalian cytochrome *c* was discovered, deeply studied, and over the years became the best characterized among the cytochrome *c* family.³⁴ *S. oneidensis* contains at least 42 types of possible cytochrome *c* proteins which were identified based on the number of CXXCH motifs present in the genome.³⁵ Unusually, cytochrome *c* nitrite reductases, including the ccNiR found in *S. oneidensis*, contain a unique motif, CXXCK instead of CXXCH, which is involved in covalently attaching the active site heme.³⁶ In prokaryotic cells, the primary function of cytochrome *c*'s is in respiration and photosynthesis. However, they can also perform other important roles. For example, in some organisms ccNiR reduces nitrite in response to nitrosative stresses instead of as part of anaerobic respiration.

In most organisms, the fundamental role of ccNiR is to catalyze nitrite ammonification during anaerobic respiration. In this process, nitrite is the electron sink in energy transduction. However, the microaerobic bacteria *Campylobacter rectus* are unable to survive when nitrite is the only electron sink, and in this case the role of ccNiR in *C. rectus* is to reduce nitric oxide to lower nitrosative stress. Because of this detoxification process, *C. rectus* bacteria are able to survive in the human oral cavity and circulatory system. Some results of this adaptation are periodontal disease, formation of plaque in the arterial walls, and other pathologies.^{37, 38} Another example in which ccNiR's primary role appears to be nitrosative stress reduction rather than

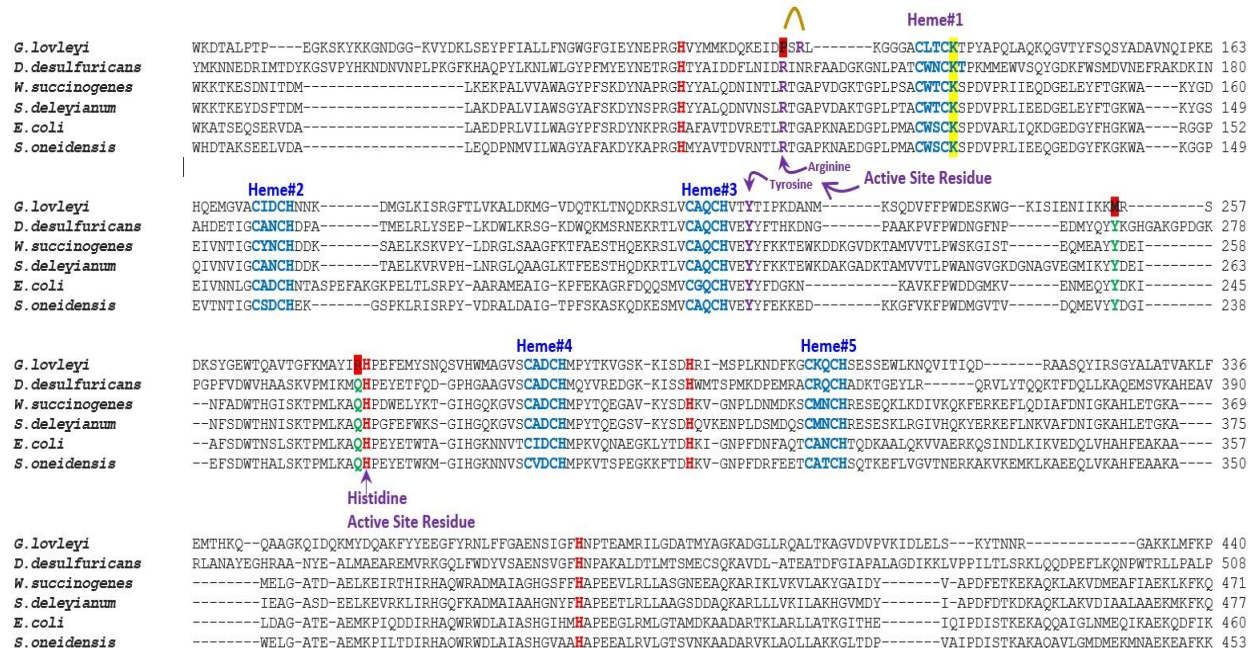


Figure 1.3. Multiple sequence alignments of different ccNiR homologues. **Blue:** The conserved amino acid sequence for the *c*-heme motif (CXXCH). The lysine (K) residue of the active site heme is highlighted in yellow. **Red:** The histidine residues conserved in the distal site for the heme centers, which conclude the bis-his ligated heme center. A **brown arc** focuses the fixates on a misalignment in the sequence for the *G. lovleyi* ccNiR, which contains R122. **Green:** Amino acids outside of the active site that are not structurally or catalytically active, thus far. **Red Highlight:** A methionine (M255) in place of the usual tyrosine in *G. lovleyi* ccNiR. The function remains unclear. The *G. lovleyi* ccNiR also has an arginine (R277) next to the active site histidine instead of a glutamine residues that is seen in other homologues ⁶.

respiration is provided by the *Campylobacter jejuni* homologue. This homologue contains a CXXCH active site motif instead of the CXXCK motif seen in most ccNiR homologues, ³⁹ as a

result of which it does not readily reduce nitrite. On the other hand, the *C. jejuni* enzyme still readily reduces nitric oxide, which is essential in the moderation of nitrosative stress.

1.8. Structure of ccNiR

Cytochrome c nitrite reductase is a stable, soluble, multi-heme respiratory enzyme found in the periplasm of a variety of gram-negative bacteria. Originally, the first crystal structure of ccNiR from *S. oneidensis* was obtained at room temperature using the Laue method (2.59 Å PDB 3UBR)²⁹, however, more recently a low temperature structure was also captured at an even higher resolution (1.66 Å, PDB 6P73).¹⁶ Both crystal structures revealed that the *S. oneidensis* enzyme is structurally similar to the previously characterized ccNiR homologues from *Wolinella succinogenes*,⁴⁰ *E. coli*,⁴¹ *Sulfurospirillum deleyianum* (1.9 Å),³⁶ *Desulfovibrio desulfuricans*,⁴² *Desulfovibrio vulgaris*,⁴³ and *Haemophilus influenzae*.³⁶

The *S. oneidensis* protein is a homodimer, where each protomer contains five *c*-type hemes and has a molecular weight around 52.9 kDa. However, the molecular weight of a protomer can vary from 52-70 kDa depending on the bacterial source.^{8, 44} Four of the hemes, specifically Heme #2 to Heme #5, are low spin, bis-histidine ligated and covalently attached to the backbone through the CXXCH sequence that was described in the previous section. In contrast, the active site heme (Heme #1) is five coordinate, high-spin ferric resting state (Fe³⁺), and contains a unique lysine (Lys 123) bound to the proximal site instead of a histidine (Fig. 1.4).⁴⁵ This unusual lysine exemplifies the novel CXXCK motif peculiar to ccNiRs. In addition to the CXXCK sequence, which is characteristic of most homologues, all cytochrome *c* nitrite reductases that have been structurally distinguished have three conserved amino acid active site residues, arginine, tyrosine, and histidine, that seem to be pivotal for optimal catalytic activity.

These amino acids may vary in residue number among the homologues; in *S. oneidensis* ccNiR the residues are Arg-103, Tyr-206, and His-257.

Electron Paramagnetic Resonance spectroscopy (EPR) is a useful tool for identifying the arrangement of hemes in ccNiR. The two imidazoles of the histidines in six-coordinate *c*-hemes can range from being completely parallel to completely perpendicular to each other (Fig. 1.2c). In EPR, hemes with perpendicular imidazoles have axial signals, whereas hemes with parallel imidazoles have rhombic signals, differences that are readily distinguishable in an EPR spectrum. Thus far, in all ccNiR variants, the imidazole planes in Heme #2 are close to parallel; however, they are the most parallel in the *S. oneidensis* homologue. The imidazole planes in Heme #3 are close to parallel as well, but the imidazole planes in Heme #4 and Heme #5 are perpendicular.⁴¹

An investigation completed by Page et al. showed that electron transfer can occur between redox centers provided the distance between the centers is less than 14 Å.⁴⁶ Thus, electron shuttling can occur between the ccNiR hemes since the heme centers are closely spaced, with the Fe-Fe distances being less than 13 Å. The physiological electron donors appear to shuttle electrons through Heme #2, then from there electrons can move from heme to heme until they reach the active site of the same protomer.^{41,43} Electrons can also move between protomers because the Heme #5s of the protomers are in close proximity to each other. Therefore, electrons can exit one protomer, enter the other protomer, and then shuttle through the other protomer's hemes to the active site heme (Fig. 1.4).⁴⁴

A calcium ion near the active site of ccNiR was first identified by Einsle et al, specifically in the *S. deleyianum* homologue. The calcium ion was found in the X-ray crystal

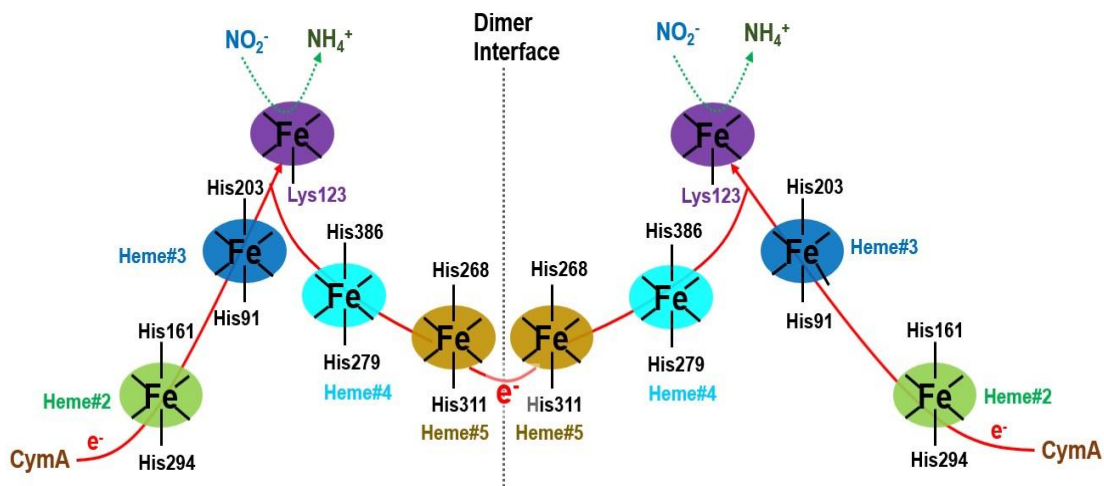


Figure 1.4. The arrangement with the ccNiR dimer of *S. oneidensis*. The protomers are separated by a black dotted line. Electrons are donated from CymA (shown in brown), entering through Heme #2. The electrons are then shuttled to Heme #3, with the predicted pathway of electron transfer shown in red. Heme #3 (blue), Heme #4 (cyan), and Heme #5 (orange) are the bis-histidine ligated electron transferring hemes (six-coordinate). The five-coordinate active site Heme#1 has the CXXCK motif, containing the Lysine and an open distal site for substrate binding.^{257, 16, 29} in *W. succinogenes* they are Arg-114, Tyr-218, and His-277, and in *S. deleyianum* they are Arg-113, Tyr-217, His-282.³⁶

structure, but later confirmed ICP-MS.³⁶ To date, with one exception discussed below, the calcium ion has been found in all structural analyses of ccNiR; however, the role of calcium in the enzyme catalysis is at present unclear.^{42, 47, 48, 49} Through structural analysis, researchers have found that the calcium ion is 10.7 Å away from the active site. There is a possibility that the cation may facilitate proton delivery during catalysis.

The secondary structure motif of ccNiR consists mainly of alpha helices. Upon the end of the peptide chain, there are four long helices and four short turns. Each protomer contains two short antiparallel beta sheets, one of which seems to form a funnel-like structure that is found relatively close to the active site, promoting substrate entry. Einsle et al, named two helices *h22* and *h25*, which help to form the dimer interface. The helix *h25* directly interacts with the second protomer. The dimer forms upon interactions between approximately 28 amino acid residues along a distance of 42 Å. This stretch is around 8.5% of the total available surface area of a protomer (Fig. 1.2).³⁶

1.9. Atypical nitrite ammonifying enzymes

Contrary to ccNiR found in *S. oneidensis* that contains a five c-type heme protomer, there are a few structural variations that have been observed in other bacterial strains. For example, in *Thi alkalivibrio nitratireducens* and *Thi alkalivibrio paradoxus*, which are characterized from the *Thi alkalivibrio* species, ccNiR is homohexameric. In these strains, a single protomer consists of eight hemes and has two domains. Three hemes are conserved in the N-terminal domain with a unique fold, while the other five hemes are in the C-terminal domain in the usual pattern observed in *S. oneidensis*. The *Thi alkalivibrio* pentaheme sequence only shows about 20% similarity to the sequence in the *S. oneidensis* domain; however, the main catalytic amino acid residues, calcium metal-binding site, and lysine bound in the proximal axial site are homologous. The *T. nitratireducens* ccNiR (referred to as TvNiR) is also different than *S. oneidensis* in the fact that there is a covalent modification between the amino acids Tyrosine-331 and Cysteine-333.⁵⁰ Another difference can be seen in the substrate entry and product exit channels.^{50, 51}

The *Desulfovibrio desulfuricans* ccNiR displays similar activity to that seen in the *S.oneidensis* ccNiR; however, there are some structural differences. The *D. desulfuricans* homologue is a NrfA:NrfH adduct (as previously stated, ccNiR is also referred to as NrfA). Therefore, with this adduct, for every five hemes of NrfA, there will be four hemes from NrfH, making the *D. desulfuricans* a nine-heme ccNiR enzyme. NrfH is the electron donor for the *D. desulfuricans* ccNiR instead of CymA, which is the electron donor for ccNiR in *S.oneidensis*. The difference between these two homologues is that ccNiR can be purified without CymA from *S.oneidensis*, whereas the *D. desulfuricans* ccNiR structurally depends on NrfH. This homologue will be discussed more in depth in Chapter 2 of this thesis.⁴²

A recent crystal structure of ccNiR from *Geobacter lovleyi* (2.55 Å resolution, PDB 6V0A) showed an interesting result in that the calcium ion normally found in the active site was not present. The structure revealed that the amino acid residue Arginine-277 provides the electrostatic stability and hydrogen-bond network that the calcium ion usually supports in the active site. Even with this modification, the ccNiR from *G. lovleyi* still displays similar catalytic properties to the other ccNiR homologues.

1.10. The bioenergetics of nitrite ammonification

Nitrite is the main electron acceptor during the ccNiR-catalyzed anaerobic respiration process, while formate is the electron donor, with NAD⁺/NADH mediating the transport of electrons. This process is not simple by any means because there are many reactions occurring at once. Nitrite reduction is not the only ammonification process that occurs. Ammonification also takes place because of nitrogenous oxidative stress due to high amounts of nitric oxide, hydroxylamine, and o-methyl hydroxylamine. In order to decrease this type of stress, these

stressor molecules must be reduced to ammonium. Sequentially, ccNiR can also mediate the reduction of sulfite to sulfide, helping to bridge the sulfur and nitrogen cycles.^{8, 39, 40, 47, 52, 53}

In the previous section, CymA was cited for its role in supplying electrons to the *S. oneidensis* ccNiR during the anaerobic respiration process, in contrast to *D. desulfuricans* which has NrfH as an electron donor. This variation in physiological electron donors is dependent on the bacterial source. The δ , ϵ , and γ -proteobacteria have different electron transport proteins that directly administer electrons to Heme #2 in ccNiR. Heme #2 is the physiological entry point for electrons.^{41, 54} *S. oneidensis* is a γ -proteobacterium, therefore electrons are supplied by Cytoplasmic Membrane Protein A or CymA. CymA is an electron transport protein that is anchored to the inner membrane with a molecular weight of ~21 kDa (Fig. 1.4). Along with *S. oneidensis*, *E. coli* is a γ -proteobacterium, however instead of CymA, the electron source is NrfB, which is a periplasmic pentaheme protein with a similar molecular weight to CymA.^{41, 55}

The structures of the *S. oneidensis* and *E. coli* homologues are quite similar, with the main difference between them being in the protein surface surrounding the electron entry point of Heme #2 (Fig. 1.4). This makes sense given the difference in electron donors for the two homologues, and results in rather interesting electrochemical effects on the enzyme.⁴⁴ Another electron donor found in other homologues of ccNiR is NrfH, which is a cytoplasmic membrane-anchored protein with a molecular weight of ~20 kDa. This is the electron source for the ϵ -proteobacterium *W. succinogenes*,^{14, 40, 56} and for the two δ -proteobacteria *D. desulfuricans*,⁴² and *D. vulgaris*.^{43, 57}

In *S. oneidensis*, the CymA protein is fixed in the inner membrane and can distribute electrons to various periplasmic reductase proteins. Upon mutating CymA, ccNiR activity,

fumarate to succinate conversion, as well as DMSO to dimethyl sulfide conversion would all be affected. CymA mediates a complex electron transport system. The Cytochrome Periplasmic Metal Reducing Proteins MtrA and Mtr B work in this complex with the outer membrane protein MtrC to facilitate the respiratory extracellular reduction of insoluble metals such as manganese dioxide.⁵⁸

The respiratory enzyme fumarate reductase (FccA) also has an essential role in the *S. oneidensis* electron transport system. FccA is a soluble, monomeric protein responsible for the reduction of fumarate to succinate upon the supply of electrons from CymA. In *S. oneidensis*, FccA has additional roles that are not seen in other organisms. For example, FccA seems to also store electrons, taking on a role as an intermediate electron acceptor when a terminal electron acceptor is not present.⁵⁹

1.11. CcNiR reaction mechanism

1.11.1. Overview

The ccNiR-mediated nitrite ammonification pathway involves the transfer of six electrons and eight protons in proton-coupled electron transfers (PCETs) at the ccNiR active site heme center. The complexity of this respiratory process has captured the interest of many researchers over time. The standard assay used for *in vitro* studies of ccNiR utilizes methyl viologen monocation radical (MV_{red} , $E^o = -0.449$ V vs. SHE) as a strong reductant to facilitate nitrite reduction. The result of this assay is ammonium product, without any detectable enzyme intermediates or other nitrogenous products.^{36, 37, 41, 60} The absence of any intermediates correlates with the prediction that each reduction step increases the protonation affinity, thus increasing the affinity for the next reduction step.³⁰ Scientific researchers soon became skeptical

of the nonappearance of intermediates and speculated that nitrogenous species such as nitric oxide and/or hydroxylamine bound to the iron of the heme active site might in fact be catalytic intermediates, which could be detected under the right conditions. This hypothesis was supported by the observation that both nitric oxide and hydroxylamine can act as substrates in the standard assay.^{36, 41, 42, 45} More recently, the Pacheco group has demonstrated that during the ccNiR-catalyzed nitrite reduction process, putative intermediates can be trapped and studied under more weakly reducing conditions than those used in the methyl viologen standard assay.^{29, 48, 49}

Milwaukee, WI, 2019.,⁶¹ These experimental results, together with crystallographic and computational studies of ccNiR have provided a progressively more complete understanding of the enzyme's mechanism. The upcoming sections describes the mechanism that has been proposed based on the computational and experimental results.

1.11.2. Structural and computational analyses of the ccNiR mechanism

1.11.2.1. The resting enzyme and nitrite activation at the active site.

Early on, spectroscopic evidence suggested that the resting state of ccNiR was a ferric iron with either no distal ligand, or a water or hydroxide bound at the distal site, depending on the protonation state of the active site conserved histidine residue.^{15, 62} More recently, the resting-state of ccNiR was observed crystallographically to have a variety of ligands occupying the distal position of Heme #1.²² The *S. oneidensis* and *E. coli* homologues were crystallized with water or hydroxide in the distal position,^{16, 41} whereas the crystal structure of *W. succiogenes* and *S. deleyianum* displayed a sulfate instead.³⁶ The crystal structure of *W. succiogenes* was also studied in the presence of the substrate nitrite, as well as the putative transient reaction intermediate, hydroxylamine.⁴⁵ In-depth computational studies were

completed by Bykov and Neese in which experimental structures were used as the basis of their calculations.⁶³⁻⁶⁶ These studies will be further addressed in the following sections.

The resting state of the enzyme was first modeled by the Neese group. The active site displayed water at the distal site of a ferric heme with a calculated bond distance of 2.106 Å between the iron of the heme and the oxygen of the water molecule.^{63,65} This calculation agreed well with the experimental structure that presented a 2.1 Å distance.⁴⁵ Contrary to the density functional method used in the calculations, EPR evidence suggests that the active site is high spin instead of low spin.^{44,67} This discrepancy between the theoretical and experimental results is due to the DFT method overestimating the stability of low spin states.⁶⁵ Although there are limitations, the calculations are still valuable in comparative studies. The calculations give evidence that water weakly binds in both the ferric and ferrous states, with binding energies of -5.6 kcal/mol and -10.8 kcal/mol, respectively. Also, during reduction, the bond length between iron and oxygen increases from 2.106 Å to 2.134 Å.

The ccNiR catalytic mechanism is proposed to be a multi-step process. This process begins upon the binding of nitrite to the distal position of the active site heme (Heme #1). In principle, nitrite can bind to iron through either a nitrogen or oxygen donor atom, since nitrite is an ambidentate ligand. The result would be a nitro form in the case of the metal-nitrogen bond formation, or a nitrito form in the case of metal-oxygen bonding (Fig. 1.5). The 2002 structure of ccNiR from *W. succinogenes* presented the nitro isomer.⁴⁵ The theoretical calculations by Bykov and Neese support the structural representation of the *W. succinogenes* homologue because the metal-oxygen bonding was predicted to be 4 kcal/mol less favorable than

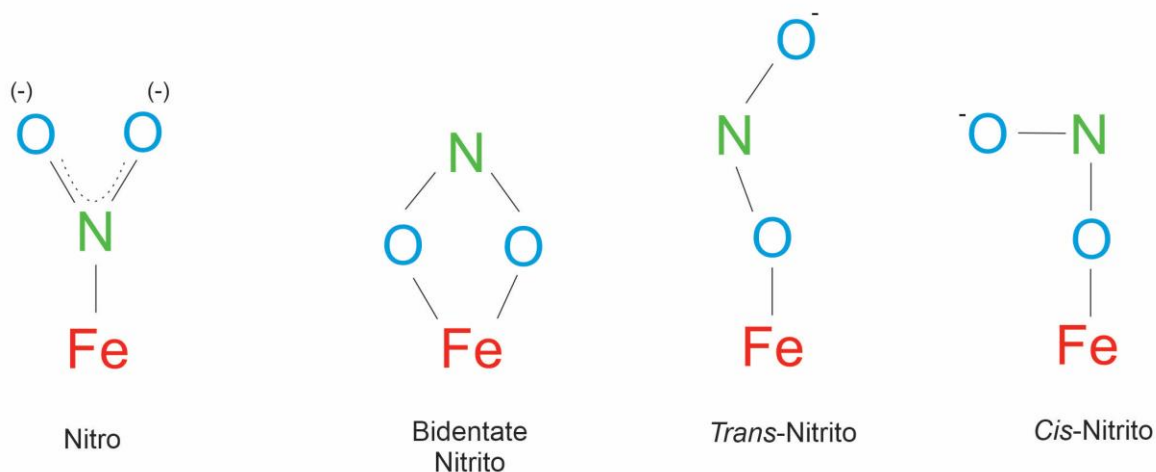


Figure 1.5. The possible modes of nitrite bound to iron.

metal-nitrogen bonding.⁶³ These calculations suggest that the proximal lysine ligand in the active site contributes to the stabilization of the iron-nitrogen bond formation. Furthermore, the positively charged amino acid residues in the active site pocket interact with the oxygen atoms of the nitrite ligand, in the case of the nitro form.^{45, 63, 65} For example, in the *S.oneidensis* homologue, His-257 and Arg-103 are the positively charged amino acids that help to stabilize the nitro isomer.⁶⁰ These residues form an electropositive environment that helps to fine-tune the iron-nitrite backbone for optimization of the consecutive PCET reactions, which will be discussed further in this section.

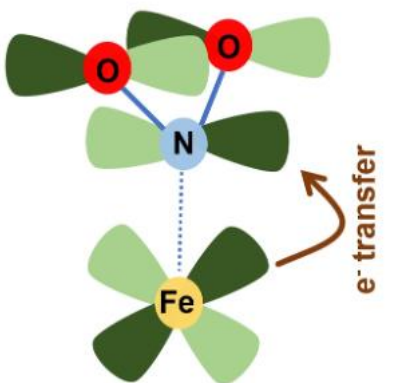


Figure 1.6. The back-bonding interaction between the active site heme of ccNiR (in the ferrous state) and the physiological substrate nitrite. The d_{xz} orbital of iron interacts with the NO_2^- lowest unoccupied molecular orbital (LUMO) of NO_2^- , which has an antibonding character with respect to the N-O bond. ⁶.

Bykov and Neese implemented density functional theory (DFT) to study the energetics and kinetics of the initial stages of nitrite reduction. The low-lying d -orbital of Fe^{II} and the lowest unoccupied molecular orbital of nitrite interact to form the $\text{Fe}^{\text{II}}\text{NO}_2^-$ complex. DFT calculations predicted that the nitro isomer becomes significantly stronger when nitrite is loaded on to a reduced ferrous active site. This prediction is supported by the p-backbonding that occurs when the electron density from the reduced iron is pushed into nitrite, which has p-antibonding with respect to the N — O bond (Fig. 1.6). As a result, the $\text{Fe}^{\text{II}} - \text{N}$ bond length decreases to 1.877 Å. By contrast, the Fe — O bond distance (between Heme #1 iron and water) in the aquo complex lengthens from 2.106 Å to 2.134 Å during the reduction of the hemes, which consequently facilitates the replacement of water by nitrite under a driving force calculated to be -39 kcal/mol. ⁶⁵ The shortening of the $\text{Fe}^{\text{II}} - \text{N}$ bond leads to the simultaneous weakening of the N — O bond in the nitrite ligand, as it adds electron density to the antibonding orbital. The nitrite N — O bond elongates, which facilitates the heterolytic cleavage of one of the N — O bonds. ^{45, 63, 65, 68}

However, this catalytic process becomes more intricate because the N – O bond cleavage is dependent on the protonation capabilities of the active site residues.

1.11.2.2. The Possible Pathways for the First N–O Bond Cleavage

The theoretical investigation by the Neese group included the role of the three conserved active site residues mentioned previously. The theory is that the residues help mediate the first N – O bond cleavage. Based on the pK_a s of the free amino acids, at physiological pH, Tyrosine and Arginine will have protonated side chains because the pK_a values are 10.1 and 12.5, respectively. The pK_a of the imidazole side chain of Histidine is 6, therefore it can be protonated or deprotonated due to the close proximity to the physiological level. Based on the study performed by Bykov and Neese, there are two possible pathways of N – O bond cleavage, either under the conditions where His is protonated, or where His is deprotonated.^{63, 65}

Under the condition where His is protonated, the idea that Tyr was a proton donor leading to HONO formation was negated because the Fe(HONO) adduct is unstable. The Fe(HONO) adduct is stable when either Arg or His act as the proton donor. However, the protonation by His is more energetically feasible, having a $\Delta G = +4.9$ kcal/mol, whereas the proton transfer by Arg is more endergonic ($\Delta G = +17.7$ kcal/mol). The calculations concluded that the transition state energy in this proton transfer step via His is +5.5 kcal/mol. The proton transfer by His is still predicted to be endergonic; however, if the Fe(HONO) is continually removed by the subsequent reactions, this process will be manageable.

The N – O bond will be cleaved upon the second proton transfer to the Fe(HONO) adduct. There are three possibilities of where this proton will come from; however, for His to be a possible donor, the side chain must be re-protonated first. When investigated computationally,

the second proton transfer event was shown to be highly endergonic. Kinetic studies have shown that the rate limiting-step of this event should stay beneath +15.2 kcal/mol. Bykov and Neese calculated that His could be re-protonated if the Fe(HONO) adduct temporarily rotated towards Tyr with an energy cost of +4.2 kcal/mol. Given the rotation of the Fe(HONO) complex and the re-protonation of His (+7.9 kcal/mol), the proton transfer event and the subsequent release of the water molecule from Fe(H₂ONO) would cost +12.1 kcal/mol energetically. This compares favorably with the expected experimental value, making the mechanistic pathway quite plausible. By contrast, protonation by Arg or Tyr have activation barriers of +24.4 kcal/mol and +37.5 kcal/mol, respectively. These values greatly exceed the experimental kinetic barrier, proving that His is the more favorable proton donor.^{47, 53} After the second PT, the water molecule would dissociate and as a result, an {Fe(NO)}⁶ intermediate would form.

There is strong crystallographic evidence that supports the theoretical conclusions of Bykov and Neese.^{45, 69} In the crystal structure of nitrite-loaded ccNiR, the active site Arg is 2.8 Å away from the second oxygen atom of nitrite; however, the active site His is 2.6 Å away from one of the oxygen atoms, making it slightly closer in proximity. Bykov and Neese calculated the hydrogen bonding distance between nitrite and His to be 1.56 Å and the two H-bonding interactions with Arg to be 2.67 Å and 2.30 Å.^{45, 63} The crystal structure with hydroxylamine in the distal site shows that the hydrogen bond between His and oxygen is now missing, but there is a hydrogen bond interaction between Arg and hydroxylamine oxygen (3.0 Å). This suggests that the oxygen from nitrite that was interacting with the protonated His was cleaved.⁴⁵

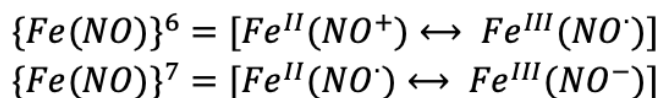
The analyses described thus far assumed that the active site His started out protonated. Alternatively, if the active site His started out in a deprotonated form, presumably at high pH, then the predicted proton transfer events would be different. There are still three possible ways

that the first protonation could occur. The most thermodynamically unfavorable proton transfer events would occur if either a Tyr or neutral His performed the first proton transfer. The most probable amino acid for the first protonation is thus Arg. The activation energy for this proton transfer is +16.7 kcal/mol, which is still within the range required by the experimental value. Another idea that was presented is that the protonation occurs from a water molecule in the active site with similar energy to the proton transfer from Arg. Under high pH conditions, the second proton transfer could occur via Tyr or Arg. However, in the case of Tyr, the reaction enthalpy is +19.2 kcal/mol and the transition state energy is +31.1 kcal/mol, which greatly exceeds the experimental barrier value. The most promising is the pathway in which Arg is re-protonated in an exothermic process with an energy of -13 kcal/mol, but must overcome an activation barrier of +14.1 kcal/mol. The key idea is that this catalytic process can occur under varying pH conditions with great adaptability.

1.11.2.3. Heme iron-nitrosyl intermediates and the second N – O bond cleavage

In an extensive computational study, the Neese group analyzed the reduction steps that take place after the cleavage of the first N – O bond. The study spans two detailed articles^{64, 66} and a review.⁶⁵ These investigations analyzed not only the changes that occur at the active site heme, but also the protonation states of the three active site amino acid residues and how these changes contribute to the enzymatic catalysis. This section summarizes the main analyses using a modified version of the shorthand key used in various papers by Bykov and Neese. Specifically, changes to the protonation states of each of the conserved amino acid residues will be signified by the one letter amino acid code with either an H or a 0 as a subscript (Scheme 1.2).

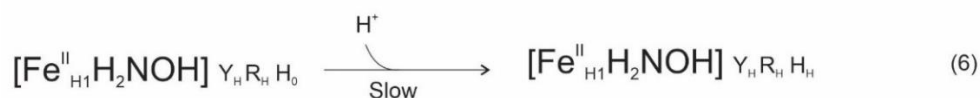
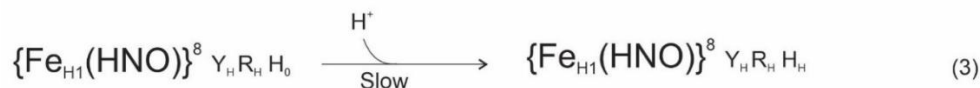
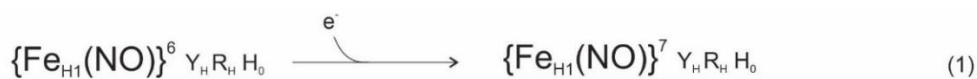
Following the hydrolysis and cleavage of the N – O bond, the nitrosyl intermediate $\{\text{Fe}_{\text{HI}}(\text{NO})\}^6$ is formed. The Enemark-Feltham notation is used to describe the various intermediates that form during the reduction process (Scheme 1.1).⁷⁰ During catalysis, $\{\text{Fe}_{\text{HI}}(\text{NO})\}^6$ is reduced to $\{\text{Fe}_{\text{HI}}(\text{NO})\}^7$ under conditions predicted to be highly exergonic.⁶⁴



Scheme 1.1. Enemark – Feltham notation used to represent iron nitrosyl species for which the electron distribution is uncertain.

This reduction process was confirmed in recent experiments performed by the Pacheco group.¹⁶
¹⁷ Next, a proton-coupled electron transfer occurs resulting in the switch from $\{\text{Fe}_{\text{HI}}(\text{NO})\}^7$ to $\{\text{Fe}_{\text{HI}}(\text{HNO})\}^8$. In the $\{\text{Fe}_{\text{HI}}(\text{NO})\}^7$ state, Tyr and Arg are protonated, while His remains deprotonated. The $\{\text{Fe}_{\text{HI}}(\text{NO})\}^7$ intermediate sits at an energetic minimum but PCET to form the $\{\text{Fe}_{\text{HI}}(\text{HNO})\}^8$ intermediate can occur in a thermoneutral process with a 6.5 kcal/mol activation barrier (Step 2, Scheme 1.2).⁶⁴ The re-protonation of the active site residues is crucial during catalysis because as the residues re-protonate, there is an increase in positive charge which leads to elongation of the N – O bond. This is due to the influence that the positive charge surrounding the active site residues has on the electron density from iron in the heme.

Reduction of $\{\text{Fe}_{\text{HI}}(\text{HNO})\}^8$ can only occur if it is coupled to proton transfer, or else the sole reduction is exceedingly endergonic. Bykov and Neese present calculations suggesting that, before PCET can occur, there is a rate-limiting step involving the protonation of the active site His (+12.9 kcal/mol, Scheme 1.2).⁶⁶ The reduction of $\{\text{Fe}_{\text{HI}}(\text{HNO})\}^8$ results in two energetically



Scheme 1.2. Some of the catalytic steps proposed for the reduction of nitrite to ammonia at the ccNiR active site, based on computational analysis.^{64-66, 70} The heme-bound nitrosyl species are represented by their Enemark-Feltham notations (Scheme 1.1). When present in protonated form, the catalytically important conserved active site amino acids are labeled as follows (using *S. oneidensis* numbering): Y_H, Tyr-206; R_H, Arg-103; H_H, His-257; and H₀-where His-257 is not in a protonated form. This shorthand is adapted from that used by Bykov and Neese,⁶⁶ but with some modifications. PCET: Proton Coupled Electron Transfer.

plausible intermediate products: $[\text{Fe}_{\text{HI}}^{\text{II}}\text{H}_2\text{NO}^\cdot]$ and $[\text{Fe}_{\text{HI}}^{\text{II}}\text{H}_2\text{NOH}]$. The $[\text{Fe}_{\text{HI}}^{\text{II}}\text{H}_2\text{NO}^\cdot]$ intermediate, shown in Step 4 of Scheme 1.2, correlates nicely with the experimental results of the Pacheco group.²⁹ Step 5 of Scheme 1.2 represents the sequential protonation and reduction of $[\text{Fe}_{\text{HI}}\text{H}_2\text{NO}^\cdot]$ to generate the hydroxylamine bound intermediate. Both these intermediates have the nitrogenous species bound to a ferrous heme. This factor must be distinguished in light of the final catalytic step described in the next paragraph.

The last step of the proposed catalytic cycle is the reduction of the hydroxylamine bound intermediate to ammonium. The computational studies⁶⁶ and the experimental analysis completed by the Pacheco lab offer evidence that this stage is quite energetically expensive. The computational results by Neese suggest that the rate limiting step is the dehydration of hydroxylamine. The pathway requires the active site His to be re-protonated at an energy expenditure of 5 kcal/mol (Step 6, Scheme 1.2). The protonation of the His is followed by the proton transfer to the oxygen of hydroxylamine, then the dehydration (Step 7, Scheme 1.2) occurs. These consecutive events have an endergonic cost of 9.0 kcal/mol and an activation barrier of 12.2 kcal/mol.⁶⁶ Two experimental results from the Pacheco group support this set of events being rate limiting at pH 7.0. First, the rate constants for nitrite and hydroxylamine reduction by MV_{red} (in electrons transferred per second) are the same.⁶⁰ Second, hydroxylamine can be oxidized but not reduced by resting ccNiR, despite the fact that the reductive step is more thermodynamically favorable.²⁹ The fact that ccNiR is incapable of catalyzing hydroxylamine disproportionation, despite a strong thermodynamic driving force, also argues for a kinetic barrier to hydroxylamine reduction.²⁹

After the hydroxylamine is dehydrated, the following reaction steps are very exergonic. Steps 8-10 in Scheme 1.2 are representative of a potential set of subsequent reactions leading to

heme-bound ammonia. In the computational analysis, the final nitrogenous product is presumably ammonia bound to ferric heme, meaning that somewhere in the process, the heme must re-oxidize with ammonia still bound. The dissociation of ammonia is dependent upon the rate at which the iron switches from a low-spin to a high-spin ferric. As the $\text{Fe}^{\text{III}} - \text{N}$ bond lengthens, the low-spin state energy increases but the high-spin state one decreases, thus the activation barrier for the dissociation coincides with the intersection between the potential energy surfaces of the low-spin state and high-spin state.⁶⁶ Although His provides the lowest energy pathway to the dehydration of hydroxylamine, calculations by Bykov and Neese show that the protonation by Tyr is advantageous as well given that Tyrosine appears to play an important role for hydroxylamine reduction.⁶⁶

1.12. Possible roles for the Ca^{2+} ion

A calcium ion close to the active site was first noted by Einsle, et.al. in a X-ray crystallographic study of the ccNiR homologue from *S. deleyianum*. The presence of calcium was later confirmed by inductively coupled plasma mass spectrometry (ICP-MS).³⁶ The calcium ion has been found in every structural characterization completed for ccNiR homologues,^{42, 47} with the exception of the *G. lovlei* homologue.⁷¹ The role of the ion in enzyme catalysis is still ambiguous. This Ca^{2+} is found 10.7 Å in distance to the active site, advocating for the hypothesis that the ion may indirectly facilitate proton delivery at the time of catalysis. The theory is that the calcium ion stabilizes hydroxide that forms during the protonation of the nitrogenous intermediates in PCET.⁶⁵ Another possibility is that hydrogen bonding can occur between Ca^{2+} and the three conserved amino acids in the active site. This would provide stability and a positive electrostatic potential to help facilitate the substrate entry of nitrite to the active site.^{42, 65}

1.13. Detection of catalytic intermediates under weakly reducing conditions

1.13.1. Detection of high potential intermediates

For the Pacheco group, the first hint that catalytic intermediates between nitrite and ammonia might be observable under the right conditions came from comparison of protein film voltammetry (PFV) and spectropotentiometry experiments. In PFV experiments, no significant catalytic current was observed at potentials higher than -120mV vs SHE,^{48, 60, 61} and yet, heme 1 ligated with the strong field ligand cyanide could be reduced at +20 mV vs SHE.⁴⁴ As nitrite is also a strong field ligand, it seemed possible that nitrite-loaded heme 1 would be reducible at potentials above those needed to fully reduce nitrite to ammonia, thus trapping one or more intermediates. This conjecture was later verified in studies that trapped the 2-electron reduced $\{\text{Fe}_{\text{H1}}\text{NO}\}^7$ intermediate,¹⁶ and detected a transient $[\text{Fe}_{\text{H1}}^{\text{II}}(\text{NO}_2^-)]$ intermediate.¹⁷ Notably, in the spectropotentiometry experiments, $[\text{Fe}_{\text{H1}}^{\text{III}}(\text{NO}_2^-)]$ was reduced to $\{\text{Fe}_{\text{H1}}\text{NO}\}^7$ in a single concerted step with a midpoint potential of +246 mV vs SHE at pH 7.0,¹⁶ which is 220 mV higher than the reported midpoint potential of the cyanide-bound active site, and over 350 mV greater than the potential at which the onset of catalysis was observed in PFV experiments.^{48, 61} These results show that $\{\text{Fe}_{\text{H1}}(\text{NO})\}^7$ is in fact a trappable putative intermediate that forms in the nitrite reduction process catalyzed by ccNiR. The accumulation of this moiety is dependent on the applied potential. At lower applied potentials, such are generated in the presence of MV_{Red} (-449mV vs SHE), rapid reduction occurs without intermediates; however, at higher potentials, catalytic ammonia formation appears to be kinetically slow, allowing intermediates to accumulate. These observations formed the basis for the Pacheco group's continuing studies of ccNiR-catalyzed reduction of nitrite by a variety of reducing agents of varying potency, with the intention of fine-tuning the applied potential to find other trappable intermediates.

1.13.2. Detection of lower potential ferrous nitrosyl intermediates

In the experiments mentioned in the previous section, the reaction of nitrite-loaded ccNiR by the weak reductant TMPD was studied by stopped-flow and UV-Vis spectropotentiometry and resulted in the observable generation of the transient intermediate $\text{Fe}_{\text{HI}}^{\text{II}}(\text{NO}_2^-)$ and the longer lived intermediate $\{\text{Fe}_{\text{HI}}(\text{NO})\}$.^{7, 16, 17} Dr. Shahid of the Pacheco group also found that under steady-state conditions, ccNiR catalyzed the slow one-electron reduction of nitrite to nitric oxide by the weak reductant TMPD. Kinetic analysis provided good evidence that the nitric oxide is released from $\{\text{Fe}_{\text{HI}}(\text{NO})\}$,⁶ though this species is not detected, but also from $\{\text{Fe}_{\text{HI}}(\text{NO})\}$ ⁷ at a much slower rate.¹⁷ In model complexes, the $\{\text{Fe}(\text{NO})\}$ ⁶ moiety is usually more labile than $\{\text{Fe}(\text{NO})\}$.^{7, 72}

In the computational studies performed by Bykov and Neese, they identify various steps in the ccNiR catalyzed nitrite reduction, suggesting that other moieties besides $\{\text{Fe}_{\text{HI}}(\text{NO})\}$ ⁷ might be experimentally trappable under the right conditions. This was further discussed in a recent report from the Pacheco group.¹⁶ Evidence of a second intermediate accumulating at applied potentials between -80 mV vs SHE and -120 mV vs SHE was presented in preliminary UV-vis spectropotentiometric studies,⁴⁴ This was supported by the results from rapid-mixing experiments performed with hydroxylamine and ccNiR.²⁹ Upon mixing ccNiR with excess amounts of hydroxylamine in varying concentrations (10mM-300mM), UV-visible stopped-flow experimental results showed that ccNiR is reduced in a triphasic exponential process. A supplemental experiment using the rapid freeze-quench technique gave evidence that a radical species builds up within 100 ms of mixing and then decays; however, the concentration never reaches zero. An EPR analysis performed by the Pacheco group suggests that this intermediate is likely to be the $[\text{Fe}_{\text{HI}}^{\text{II}}\text{H}_2\text{NO}\cdot]$ moiety that was presented in studies by Bykov and Neese shown

in Step 4 and 5, Scheme 1.2.^{29, 66} The stopped-flow and rapid freeze-quench EPR experiments both reveal that within 10s of mixing ccNiR and hydroxylamine, the electrons are transferred from hydroxylamine to the ccNiR heme pool, generating an equilibrium mixture of partially reduced nitrosylated ccNiR putative intermediates.²⁹ The use of reducing agents that are more powerful than TMPD but weaker than MV_{red} , such as reduced indigo trisulfonate ($I3S_{red}$), may generate one or more catalytic intermediates, tentatively assigned as four-electron reduced, and possibly the three-electron reduced ccNiR moieties.

1.14. Specific objectives of this thesis

Our understanding of the ccNiR reaction mechanism is summarized in Figure 1.7. This schematic is based on the theoretical and experimental evidence reviewed in Section 1.13. The Pacheco group proposes that the rate-limiting step for ccNiR-catalyzed reduction of nitrite to ammonia is the final 2-electron reduction of a Heme #1-bound hydroxylamine equivalent (specifically, Steps 6 and 7 in Scheme 1.2). A strong reducing agent, such as MV_{red} , is capable of overcoming this activation barrier, whereas weaker reductants may allow the accumulation of partially reduced nitrosylated ccNiR moieties. This hypothesis is supported by the fact that the k_{cat} values (measured in electrons transferred per second) are the same for nitrite and hydroxylamine reduction to ammonium in the presence of MV_{red} .⁶⁰

Chapter 2 of this thesis provides an in depth description of the growth of *S. oneidensis*, the purification of ccNiR from the bacteria, the identification and quantification of ccNiR, and the steady-state kinetics of the ccNiR-catalyzed reduction of nitrite under standard assay conditions. Chapter 3 describes assays aimed at detecting any hydroxylamine that might form as a side product under weakly reducing conditions, while the study presented in Chapter 4 is aimed at

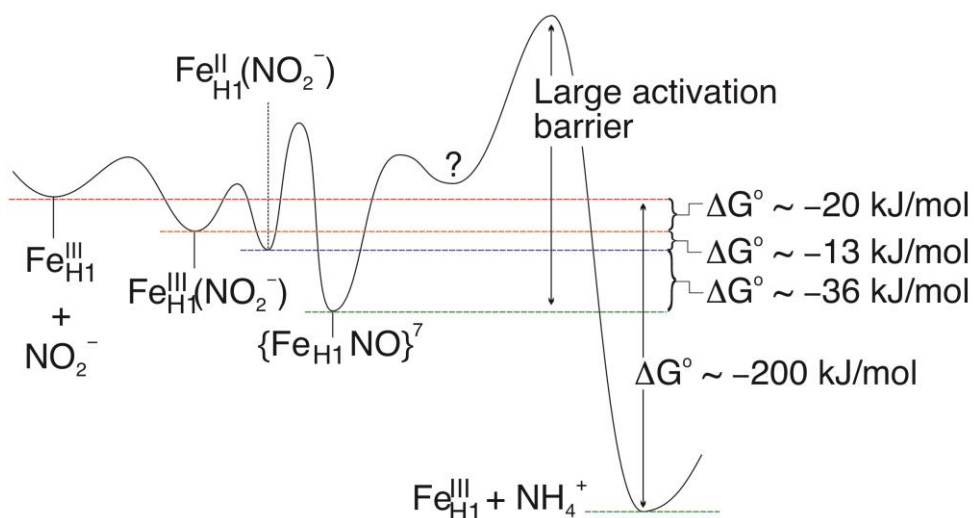


Figure 1.7. Cartoon representation of the ccNiR-catalyzed nitrite reduction path proposed based on experimental and theoretical data available at the start of the project described in this thesis.

quantifying the amount of ammonium formed from ccNiR-catalyzed reduction of nitrite by the weak reductants reduced indigo trisulfonate (I3S_{Red}), reduced indigo tetrasulfonate (I4S_{Red}) and hexaammineruthenium(II) (Ru^{II}). The quantification of ammonium under these conditions not only helps to put a limit on side product formation, but also gives further indication that putative ccNiR intermediates form in the reduction process. Chapter 5 describes the search for the putative four-electron reduced ccNiR intermediate using UV-Vis stopped-flow techniques. In these experiments, I3S_{Red} and I4S_{Red} are the weak reductants used to reduce nitrite-loaded ccNiR. In addition though, Chapter 5 also presents a stopped-flow study in which nitrite-loaded ccNiR is reduced by MV_{red}. This study shows that even when MV_{red} is used, enzymatic intermediates with nitrogen moieties in the active site are detectable after the MV_{red} has been consumed, and these moieties are comparatively long-lived. Finally, Chapter 6 presents preliminary studies that have as a long-term goal the investigation of the two-electron reduced ccNiR intermediate by time-

resolved X-ray crystallography. The chapter describes the conditions needed for making ccNiR microcrystals, catalytic studies of microcrystals using the standard assay, and SONICC Signal and Micro-ED crystal screening tests. Preliminary diffraction patterns obtained with the European X-ray free electron Laser (EuXFEL) will also be presented.

1.15 References

- (1) Aczel, M. What Is the Nitrogen Cycle and Why Is It Key to Life? *Front. Young Minds* **2019**. DOI: 10.3389/frym.2019.00041.
- (2) Britto, D. T.; Kronzucker, H. J. NH₄⁺ toxicity in higher plants: a critical review. *Journal of Plant Physiology* **2002**, *159* (6), 567-584. DOI: <https://doi.org/10.1078/0176-1617-0774>.
- (3) Weathers, K. C.; Groffman, P. M.; Van Dolah, E.; Bernhardt, E.; Grimm, N. B.; McMahon, K.; Schimel, J.; Paolisso, M.; Maranger, R.; Baer, S.; et al. Frontiers in Ecosystem Ecology from a Community Perspective: The Future is Boundless and Bright. *Ecosystems* **2016**, *19* (5), 753-770. DOI: 10.1007/s10021-016-9967-0. Brady, N. W. R. Nutrient cycles and soil fertility. In *Elements of the Nature and Properties of Soils, 3rd Edn.*, Anthony, V. R. Ed.; Pearson Education Inc., 2010; pp 396–420.
- (4) Peoples, M. B.; Herridge, D. F.; Ladha, J. K. Biological nitrogen fixation: An efficient source of nitrogen for sustainable agricultural production? *Plant and Soil* **1995**, *174* (1), 3-28. DOI: 10.1007/BF00032239.
- (5) Manahan, S. E. In *Environmental Chemistry, 9th Edn.*, CRC Press, 2010; pp 166–172.
- (6) Shahid, S. A mechanistic investigation of cytochrome c nitrite reductase catalyzed reduction of nitrite to ammonia: the search for catalytic intermediates. University of Wisconsin-Milwaukee, Milwaukee, WI, 2020.
- (7) Cole, J. A. Independent pathways for the anaerobic reduction of nitrite to ammonia by *Escherichia coli*. *Biochem Soc Trans* **1982**, *10* (6), 476-478. DOI: 10.1042/bst0100476 From 1982 Dec. Kajie S Fau - Anraku, Y.; Anraku, Y. Purification of a hexaheme cytochrome c552 from *Escherichia coli* K 12 and its properties as a nitrite reductase. (0014-2956 (Print)). From 1986 Jan 15.
- (8) Liu, M. C.; Peck, H. D. The isolation of a hexaheme cytochrome from *Desulfovibrio desulfuricans* and its identification as a new type of nitrite reductase. *Journal of Biological Chemistry* **1981**, *256* (24), 13159-13164. DOI: 10.1016/s0021-9258(18)43021-9.
- (9) Schumacher, W.; Kroneck, P. M. H.; Pfennig, N. Comparative systematic study on ?*Spirillum*? 5175, *Campylobacter* and *Wolinella* species. *Archives of Microbiology* **1992**, *158* (4), 287-293. DOI: 10.1007/bf00245247.
- (10) Kroneck, P. M. H.; Beuerle, J.; Schumacher, W. Metal Dependent Conversion of Inorganic Nitrogen and Sulfur Compounds. In *Metal Ions in Biological Systems*, Sigel, H., Sigel, A. Eds.; Marcel Dekker Inc., 1992; pp 455-505.
- (11) Summers, D. P.; Chang, S. Prebiotic ammonia from reduction of nitrite by iron (II) on the early Earth. *Nature* **1993**, *365* (6447), 630-633. DOI: 10.1038/365630a0.
- (12) Moreno-Vivian, C.; Ferguson, S. J. Definition and distinction between assimilatory, dissimilatory, and respiratory pathways. *Mol. Microbiol.* **1998**, *29*, 661-669.

- (13) Fritz, G.; Einsle, O.; Rudolf, M.; Schiffer, A.; Kroneck, P. M. H. Key bacterial multi-centered metal enzymes involved in nitrate and sulfate respiration. *J. Mol. Microbiol. Biotechnol.* **2005**, *10*, 223-233.
- (14) Simon, J. Enzymology and bioenergetics of respiratory nitrite ammonification. *FEMS Microbiol. Rev.* **2002**, *26*, 285-309.
- (15) Richardson, D. J. Bacterial respiration: a flexible process for a changing environment. *Microbiology* **2000**, *146*, 551-571.
- (16) Ali, M.; Stein, N.; Mao, Y.; Shahid, S.; Schmidt, M.; Bennett, B.; Pacheco, A. A. Trapping of a putative intermediate in the cytochrome *c* nitrite reductase (ccNiR)-catalyzed reduction of nitrite: implications for the ccNiR reaction mechanism. *J. Am. Chem. Soc.* **2019**, *141*, 13358-13371. DOI: 10.1021/jacs.9b03036.
- (17) Shahid, S.; Ali, M.; Legaspi-Humiston, D.; Wilcoxon, J.; Pacheco, A. A. A kinetic investigation of the early steps in cytochrome *c* nitrite reductase (ccNiR)-catalyzed reduction of nitrite. *Biochemistry* **2021**, *60*, 2098-2115.
- (18) Venkateswaran, K.; Moser, D. P.; Dollhopf, M. E.; Lies, D. P.; Saffarini, D. A.; MacGregor, B. J.; Ringelberg, D. B.; White, D. C.; Miyuki, N.; Sano, H.; et al. Polyphasic taxonomy of the genus *Shewanella* and description of *Shewanella oneidensis* sp. nov. *International Journal of Systematic Bacteriology* **1999**, *49*, 705-724.
- (19) Galnack, J. A.; Vali, H.; Lies, D. P.; Newman, D. K. Extracellular respiration of dimethyl sulfoxide by *Shewanella oneidensis* strain MR-1. *Proc Natl Acad Sci U S A* **2006**, *103* (12), 4669-4674. DOI: 10.1073/pnas.0505959103 From 2006 Mar 21.
- (20) MacDonell, M. T.; Colwell, R. R. Phylogeny of the Vibrionaceae, and Recommendation for Two New Genera, *Listonella* and *Shewanella*. *Systematic and Applied Microbiology* **1985**, *6* (2), 171-182. DOI: [https://doi.org/10.1016/S0723-2020\(85\)80051-5](https://doi.org/10.1016/S0723-2020(85)80051-5).
- (21) Methe, B. A.; Nelson, K. E.; Eisen, J. A.; Paulsen, I. T.; Nelson, W.; Heidelberg, J. F.; Wu, D.; Wu, M.; Ward, N.; Beanan, M. J.; et al. Genome of *Geobacter sulfurreducens*: metal reduction in subsurface environments. *Science* **2003**, *302* (5652), 1967-1969. DOI: 10.1126/science.1088727 From 2003 Dec 12.
- (22) Mowat, C. G.; Chapman, S. J. Multi-heme cytochromes - new structures, new chemistry. *J. Chem. Soc. Dalton Trans.* **2005**, *21*, 3381-3389.
- (23) Heidelberg, J. F.; Paulsen, I. T.; Nelson, K. E.; Gaidos, E. J.; Nelson, W. C.; Read, T. D.; Eisen, J. A.; Seshadri, R.; Ward, N.; Methe, B.; et al. Genome sequence of the dissimilatory metal ion-reducing bacterium *Shewanella oneidensis*. *Nature Biotechnology* **2002**, *20*, 1118-1123.
- (24) Da Silva, J. F.; Williams, R. J. P. *The biological chemistry of the elements: the inorganic chemistry of life*; Oxford University Press, 2001.
- (25) Sigfridsson, E.; Olsson, M. H. M.; Ryde, U. A Comparison of the Inner-Sphere Reorganization Energies of Cytochromes, Iron-Sulfur Clusters, and Blue Copper Proteins. *The Journal of Physical Chemistry B* **2001**, *105* (23), 5546-5552. DOI: 10.1021/jp0037403.
- (26) Moura, I.; Pauleta, S. R.; Moura, J. J. Enzymatic activity mastered by altering metal coordination spheres. *J Biol Inorg Chem* **2008**, *13* (8), 1185-1195. DOI: 10.1007/s00775-008-0414-3 From 2008 Nov.
- (27) Dias, J. M.; Alves, T.; Bonifacio, C.; Pereira, A. S.; Trincao, J.; Bourgeois, D.; Moura, I.; Romao, M. J. Structural basis for the mechanism of Ca(2+) activation of the di-heme cytochrome *c* peroxidase from *Pseudomonas nautica* 617. *Structure* **2004**, *12* (6), 961-973. DOI: 10.1016/j.str.2004.03.025 From 2004 Jun. Echaliér, A.; Goodhew, C. F.; Pettigrew, G. W.;

- Fulop, V. Activation and catalysis of the di-heme cytochrome c peroxidase from *Paracoccus pantotrophus*. *Structure* **2006**, *14* (1), 107-117. DOI: 10.1016/j.str.2005.09.011 From 2006 Jan.
- Echalier, A.; Brittain, T.; Wright, J.; Boycheva, S.; Mortuza, G. B.; Fülöp, V.; Watmough, N. J. Redox-Linked Structural Changes Associated with the Formation of a Catalytically Competent Form of the Diheme Cytochrome c Peroxidase from *Pseudomonas aeruginosa*. *Biochemistry* **2008**, *47* (7), 1947-1956. DOI: 10.1021/bi702064f.
- (28) Messerschmidt A, H. R., Poulos T, Wieghart K. *Handbook of Metalloproteins*; Wiley, 2001.
- (29) Youngblut, M.; Pauly, D. J.; Stein, N.; Walters, D.; Conrad, J. A.; Moran, G. R.; Bennett, B.; Pacheco, A. A. *Shewanella oneidensis* cytochrome c nitrite reductase (ccNiR) does not disproportionate hydroxylamine to ammonia and nitrite, despite a strongly favorable driving force. *Biochemistry* **2014**, *53*, 2136-2144.
- (30) Maia, L. B.; Moura, J. G. How biology handles nitrite. *Chem. Rev.* **2014**, *114*, 5273-5357.
- (31) Yamanaka, T. O., K. Cytochromes. In *Microbial Iron Metabolism*, Neilands, J. B. Ed.; Ed. Academic Press, 1974; pp 349-400.
- (32) Puustinen, A.; Wikstrom, M. The heme groups of cytochrome o from *Escherichia coli*. *Proc Natl Acad Sci U S A* **1991**, *88* (14), 6122-6126. DOI: 10.1073/pnas.88.14.6122 From 1991 Jul 15.
- (33) Myers, C. R.; Myers, J. M. Localization of cytochromes to the outer membrane of anaerobically grown *Shewanella putrefaciens* MR-1. *J Bacteriol* **1992**, *174* (11), 3429-3438. DOI: 10.1128/jb.174.11.3429-3438.1992 From 1992 Jun.
- (34) Munn, C. A. M. Researches on Myohaematin and the Histohaematins. *Philosophical Transactions of the Royal Society of London* **1886**, *177*, 267-298. (accessed 2023/04/30/).JSTOR.
- (35) Meyer, T. E.; Tsapin, A. I.; Vandenberghe, I.; de Smet, L.; Frishman, D.; Neelson, K. H.; Cusanovich, M. A.; J.J., v. B. Identification of 42 possible cytochrome c genes in the *Shewanella oneidensis* genome and characterization of six soluble cytochromes. *OMICS: A Journal of Integrative Biology* **2004**, *8* (1), 57-77.
- (36) Einsle, O.; Messerschmidt, A.; Stach, P.; Bourenkov, G. P.; Bartunik, H. D.; Huber, R.; Kroneck, P. M. H. Structure of cytochrome c nitrite reductase. *Nature* **1999**, *400* (6743), 476-480.
- (37) Poock, S. R.; Leach, E. R.; Moir, J. W.; Cole, J. A.; Richardson, D. J. Respiratory detoxification of nitric oxide by the cytochrome c nitrite reductase of *Escherichia coli*. *J Biol Chem* **2002**, *277* (26), 23664-23669. DOI: 10.1074/jbc.M200731200 From 2002 Jun 28.
- (38) Pittman, M. S.; Elvers, K. T.; Lee, L.; Jones, M. A.; Poole, R. K.; Park, S. F.; Kelly, D. J. Growth of *Campylobacter jejuni* on nitrate and nitrite: electron transport to NapA and NrfA via NrfH and distinct roles for NrfA and the globin Cgb in protection against nitrosative stress. *Mol. Microbiol.* **2007**, *63*, 575-590. Macuch, P. J.; Tanner, A. C. *Campylobacter* species in health, gingivitis, and periodontitis. *J. Dent. Res.* **2000**, *79*, 785-792. Marcelino, S. L.; Gaetti-Jardim, E., Jr.; Nakano, V.; Canonico, L. A.; Nunes, F. D.; Lotufo, R. F.; Pustiglioni, F. E.; Romito, G. A.; Avila-Campos, M. J. Presence of periodontopathic bacteria in coronary arteries from patients with chronic periodontitis. *Anaerobe* **2010**, *16* (6), 629-632. DOI: 10.1016/j.anaerobe.2010.08.007 From 2010 Dec.
- (39) Klotz, M. G.; Schmid, M. C.; Strous, M.; op den Camp, H. J. M.; Jetten, M. S. M.; Hooper, A. B. Evolution of an octahaem cytochrome c protein family that is key to aerobic and anaerobic ammonia oxidation by bacteria. *Environ. Microbiol.* **2008**, *10*, 3150-3163.

- (40) Einsle, O.; Stach, P.; Messerschmidt, A.; Simon, J.; Kroger, A.; Huber, R.; Kroneck, P. M. H. Cytochrome c nitrite reductase from *Wolinella succinogenes* - Structure at 1.6 angstrom resolution, inhibitor binding, and heme-packing motifs. *J. Biol. Chem.* **2000**, *275* (50), 39608-39616.
- (41) Bamford, V. A.; Angove, H. C.; Seward, H. E.; Thomson, A. J.; Cole, J. A.; Butt, J. N.; Hemmings, A. M.; Richardson, D. J. Structure and spectroscopy of the periplasmic cytochrome c nitrite reductase from *Escherichia coli*. *Biochemistry* **2002**, *41* (9), 2921-2931. DOI: 10.1021/Bi015765d.
- (42) Cunha, C. A.; Macieira, S.; Dias, J. M.; Almeida, G.; Goncalves, L. L.; Costa, C.; Lampreia, J.; Huber, R.; Moura, J. J. G.; Moura, I.; et al. Cytochrome c nitrite reductase from *Desulfovibrio desulfuricans* ATCC 27774 - The relevance of the two calcium sites in the structure of the catalytic subunit (NrfA). *J. Biol. Chem.* **2003**, *278* (19), 17455-17465. DOI: 10.1074/jbc.M211777200.
- (43) Rodrigues, M. L.; Oliveira, T.; Matias, P. M.; Martins, C.; Valente, F. M.; Pereira, I. A.; Archer, M. Crystallization and preliminary structure determination of the membrane-bound complex cytochrome c nitrite reductase from *Desulfovibrio vulgaris* Hildenborough. *Acta Cryst. F* **2006**, *62*, 565-568.
- (44) Stein, N.; Love, D.; Judd, E. T.; Elliott, S. J.; Bennett, B.; Pacheco, A. A. Correlations between the electronic properties of *Shewanella oneidensis* cytochrome c nitrite reductase (ccNiR) and its structure: effects of heme oxidation state and active site ligation. *Biochemistry* **2015**, *54*, 3749-3758.
- (45) Einsle, O.; Messerschmidt, A.; Huber, R.; Kroneck, P. M. H.; Neese, F. Mechanism of the six-electron reduction of nitrite to ammonia by cytochrome c nitrite reductase. *J. Am. Chem. Soc.* **2002**, *124* (39), 11737-11745. DOI: 10.1021/Ja0206487.
- (46) Page, C. C.; Moser, C. C.; Chen, X.; Dutton, P. L. Natural engineering principles of electron tunnelling in biological oxidation-reduction. *Nature* **1999**, *402* (6757), 47-52. DOI: 10.1038/46972.
- (47) Stach, P.; Einsle, O.; Schumacher, W.; Kurun, E.; Kroneck, P. M. H. Bacterial cytochrome c nitrite reductase: new structural and functional aspects. *J. Inorg. Biochem.* **2000**, *79*, 381-385.
- (48) Judd, E. T.; Youngblut, M.; Pacheco, A. A.; Elliott, S. J. Direct Electrochemistry of *Shewanella oneidensis* Cytochrome c Nitrite Reductase: Evidence of Interactions across the Dimeric Interface. *Biochemistry* **2012**, *51* (51), 10175-10185.
- (49) Ali, M. Probing the early steps in the catalytic reduction of nitrite to ammonia, catalyzed by cytochrome c nitrite reductase. University of Wisconsin-Milwaukee, Milwaukee, WI, 2019.
- (50) Polyakov, K. M.; Boyko, K. M.; Tikhonova, T. V.; Slutsky, A.; Antipov, A. N.; Zvyagilskaya, R. A.; Popov, A. N.; Bourenkov, G. P.; Lamzin, V. S.; Popov, V. O. High-resolution structural analysis of a novel octaheme cytochrome c nitrite reductase from the haloalkaliphilic bacterium *Thioalkalivibrio nitratireducens*. *J Mol Biol* **2009**, *389* (5), 846-862. DOI: 10.1016/j.jmb.2009.04.037 From 2009 Jun 26.
- (51) Tikhonova, T. V.; Slutsky, A.; Antipov, A. N.; Boyko, K. M.; Polyakov, K. M.; Sorokin, D. Y.; Zvyagilskaya, R. A.; Popov, V. O. Molecular and catalytic properties of a novel cytochrome c nitrite reductase from nitrate-reducing haloalkaliphilic sulfur-oxidizing bacterium *Thioalkalivibrio nitratireducens*. *Biochim Biophys Acta* **2006**, *1764* (4), 715-723. DOI: 10.1016/j.bbapap.2005.12.021 From 2006 Apr. Tikhonova, T. V.; Slutskaya, E. S.; Filimonenkov, A. A.; Boyko, K. M.; Kleimenov, S. Y.; Konarev, P. V.; Polyakov, K. M.; Svergun, D. I.; Trofimov, A. A.; Khomenkov, V. G.; et al. Isolation and oligomeric composition

of cytochrome c nitrite reductase from the haloalkaliphilic bacterium *Thioalkalivibrio nitratireducens*. *Biochemistry (Mosc)* **2008**, *73* (2), 164-170. DOI: 10.1134/s0006297908020077 From 2008 Feb. Tikhonova, T.; Tikhonov, A.; Trofimov, A.; Polyakov, K.; Boyko, K.; Cherkashin, E.; Rakitina, T.; Sorokin, D.; Popov, V. Comparative structural and functional analysis of two octaheme nitrite reductases from closely related *Thioalkalivibrio* species. *FEBS J* **2012**, *279* (21), 4052-4061. DOI: 10.1111/j.1742-4658.2012.08811.x From 2012 Nov.

(52) Pereira, I. C.; Abreu Ia Fau - Xavier, A. V.; Xavier Av Fau - LeGall, J.; LeGall J Fau - Teixeira, M.; Teixeira, M. Nitrite reductase from *Desulfovibrio desulfuricans* (ATCC 27774)--a heterooligomer heme protein with sulfite reductase activity. *Biochem Biophys Res Commun* **1996**, (0006-291X (Print)), 611-618. Lukat, P.; Rudolf, M.; Stach, P.; Messerschmidt, A.; Kroneck, P.; Simon, J.; Einsle, O. Binding and Reduction of Sulfite by Cytochrome c Nitrite Reductase. *Biochemistry* **2008**, *47*, 2080-2086. Kemp, G. L.; Clarke Ta Fau - Marritt, S. J.; Marritt Sj Fau - Lockwood, C.; Lockwood C Fau - Poock, S. R.; Poock Sr Fau - Hemmings, A. M.; Hemmings Am Fau - Richardson, D. J.; Richardson Dj Fau - Cheesman, M. R.; Cheesman Mr Fau - Butt, J. N.; Butt, J. N. Kinetic and thermodynamic resolution of the interactions between sulfite and the pentahaem cytochrome NrfA from *Escherichia coli*. *Biochem J*. **2010**, (1470-8728 (Electronic)), 73-80.

(53) Clarke, T. A.; Hemmings, A. M.; Burlat, B.; Butt, J. N.; Cole, J. A.; Richardson, D. J. Comparison of the structural and kinetic properties of the cytochrome c nitrite reductases from *Escherichia coli*, *Wolinella succinogenes*, *Sulfurospirillum deleyianum* and *Desulfovibrio desulfuricans*. *Biochem Soc Trans* **2006**, *34* (Pt 1), 143-145. DOI: 10.1042/BST0340143 From 2006 Feb.

(54) Burlat, B.; Gwyer, J. D.; Poock, S.; Clarke, T.; Cole, J. A.; Hemmings, A. M.; Cheesman, M. R.; Butt, J. N.; Richardson, D. J. Cytochrome c nitrite reductase: from structural to physicochemical analysis. *Biochemical Society Transactions* **2005**, *33*, 137-140.

(55) Myers Cr Fau - Nealson, K. H.; Nealson, K. H. Bacterial manganese reduction and growth with manganese oxide as the sole electron acceptor. *Science* **1988**, (0036-8075 (Print)), 1319-1321. Simon, J.; Kern, M. Quinone-reactive proteins devoid of haem b form widespread membrane-bound electron transport modules in bacterial respiration. *Biochem Soc Trans* **2008**, *36* (Pt 5), 1011-1016. DOI: 10.1042/BST0361011 From 2008 Oct. Berks, B. C.; Ferguson, S. J.; Moir, J. W. B.; Richardson, D. J. Enzymes and associated electron transport systems that catalyse the respiratory reduction of nitrogen oxides and oxyanions. *Biochimica et Biophysica Acta (BBA) - Bioenergetics* **1995**, *1232* (3), 97-173. DOI: [https://doi.org/10.1016/0005-2728\(95\)00092-5](https://doi.org/10.1016/0005-2728(95)00092-5). Lockwood, C.; Butt Jn Fau - Clarke, T. A.; Clarke Ta Fau - Richardson, D. J.; Richardson, D. J. Molecular interactions between multiheme cytochromes: probing the protein-protein interactions between pentahaem cytochromes of a nitrite reductase complex. *Biochem Soc Trans* **2011**, (1470-8752 (Electronic)), 263-268. Clarke, T. A.; Cole, J. A.; Richardson, D. J.; Hemmings, A. M. The crystal structure of the pentahaem c-type cytochrome NrfB and characterization of its solution-state interaction with the pentahaem nitrite reductase NrfA. *Biochem J* **2007**, *406* (1), 19-30. DOI: 10.1042/BJ20070321 From 2007 Aug 15.

(56) Shi, L.; Chen, B.; Wang, Z.; Elias, D. A.; Mayer, M. U.; Gorby, Y. A.; Ni, S.; Lower, B. H.; Kennedy, D. W.; Wunschel, D. S.; et al. Isolation of a high-affinity functional protein complex between OmcA and MtrC: two outer membrane decaheme c-type cytochromes of *Shewanella oneidensis* MR-1. *J. Bacteriol.* **2006**, *188*, 4705-4714.

(57) Todorovic, S.; Rodrigues, M. L.; Matos, D.; Pereira, I. A. C. Redox Properties of Lysine- and Methionine-Coordinated Hemes Ensure Downhill Electron Transfer in NrfH2A4 Nitrite

- Reductase. *The Journal of Physical Chemistry B* **2012**, *116* (19), 5637-5643. DOI: 10.1021/jp301356m.
- (58) Hartshorne, R. S.; Reardon Cl Fau - Ross, D.; Ross D Fau - Nuester, J.; Nuester J Fau - Clarke, T. A.; Clarke Ta Fau - Gates, A. J.; Gates Aj Fau - Mills, P. C.; Mills Pc Fau - Fredrickson, J. K.; Fredrickson Jk Fau - Zachara, J. M.; Zachara Jm Fau - Shi, L.; Shi L Fau - Beliaev, A. S.; et al. Characterization of an electron conduit between bacteria and the extracellular environment. *Proc Natl Acad Sci U S A* **2009**, (1091-6490 (Electronic)), 22169-22174.
- (59) Leys, D.; Tsapin, A. S.; Nealsen, K. H.; Meyer, T. E.; Cusanovich, M. A.; Beeumen, J. J. V. Structure and mechanism of the flavocytochrome c fumarate reductase of *Shewanella putrefaciens* MR-1. *Nature Structural Biology* **1999**, *6* (12), 1113-1117. DOI: 10.1038/70051.
- Schuetz, B.; Schicklberger, M.; Kuermann, J.; Spormann, A. M.; Gescher, J. Periplasmic electron transfer via the c-type cytochromes MtrA and FccA of *Shewanella oneidensis* MR-1. *Appl Environ Microbiol* **2009**, *75* (24), 7789-7796. DOI: 10.1128/AEM.01834-09 From 2009 Dec. Pessanha, M.; Rothery, E. L.; Miles, C. S.; Reid, G. A.; Chapman, S. K.; Louro, R. O.; Turner, D. L.; Salgueiro, C. A.; Xavier, A. V. Tuning of functional heme reduction potentials in *Shewanella* fumarate reductases. *Biochim Biophys Acta* **2009**, *1787* (2), 113-120. DOI: 10.1016/j.bbabi.2008.11.007 From 2009 Feb.
- (60) Youngblut, M.; Judd, E. T.; Srajer, V.; Sayyed, B.; Goelzer, T.; Elliott, S. J.; Schmidt, M.; Pacheco, A. A. Laue crystal structure of *Shewanella oneidensis* cytochrome c nitrite reductase from a high-yield expression system. *J. Biol. Inorg. Chem.* **2012**, *17*, 647-662.
- (61) Judd, E. T.; Stein, N.; Pacheco, A. A.; Elliott, S. J. Hydrogen bonding networks tune proton-coupled redox steps during the enzymatic six-electron conversion of nitrite to ammonia. *Biochemistry* **2014**, *53*, 5638-5646.
- (62) Costa, C.; Moura, J. G.; Moura, I.; Liu, M. Y.; Peck, H. D.; LeGall, J.; Wang, Y.; Huynh, B. H. Hexaheme nitrite reductase from *Desulfovibrio desulfuricans* (Mossbauer and EPR characterization of the heme groups). *J. Biol. Chem.* **1990**, *265*, 14382-14387.
- (63) Bykov, D.; Neese, F. Substrate binding and activation in the active site of cytochrome c nitrite reductase: a density functional study. *J. Biol. Inorg. Chem* **2011**, *16*, 417-430.
- (64) Bykov, D.; Neese, F. Reductive activation of the heme iron-nitrosyl intermediate in the reaction mechanism of cytochrome c nitrite reductase: a theoretical study. *J. Biol. Inorg. Chem.* **2012**, *17* (5), 741-760.
- (65) Bykov, D.; Neese, F. Six-electron reduction of nitrite to ammonia by cytochrome c nitrite reductase: insights from density functional theory studies. *Inorg. Chem.* **2015**, *54*, 9303-9316.
- (66) Bykov, D.; Plog, M.; Neese, F. Heme-bound nitroxyl, hydroxylamine, and ammonia ligands as intermediates in the reaction cycle of cytochrome c nitrite reductase: a theoretical study. *J. Biol. Inorg. Chem.* **2014**, *19*, 97-112.
- (67) Pisa, R.; Stein T Fau - Eichler, R.; Eichler R Fau - Gross, R.; Gross R Fau - Simon, J.; Simon, J. The nrfl gene is essential for the attachment of the active site haem group of *Wolinella succinogenes* cytochrome c nitrite reductase. *Mol Microbiol* **2002**, (0950-382X (Print)), 763-770. Martins, G.; Rodrigues, L.; Cunha, F. M.; Matos, D.; Hildebrandt, P.; Murgida, D. H.; Pereira, I. A. C.; Todorovic, S. Substrate binding to a nitrite reductase induces a spin transition. *J. Phys. Chem. B* **2010**, *114*, 5563-5566. Lockwood, C. W. J.; Burlat, B.; Cheesman, M. R.; Kern, M.; Simon, J.; Clarke, T.; Richardson, D. J.; Butt, J. N. Resolution of key roles for the distal pocket histidine in cytochrome c nitrite reductases. *J. Am. Chem. Soc.* **2015**, *137*, 3059-3068.

- (68) Nasri, H.; Ellison, M. K.; Shang, M.; Schultz, C. E.; Scheidt, W. R. Variable π -bonding in iron(II) porphyrinates with nitrite, CO, and tert-butyl isocyanide: characterization of [Fe(TpivPP)(NO₂)(CO)]. *Inorg. Chem.* **2004**, *43*, 2932-2942. Nasri, H.; Ellison, M. K.; Krebs, C.; Huynh, B. H.; Scheidt, W. R. Highly variable π -bonding in the interaction of iron(II) porphyrinates with nitrite. *J. Am. Chem. Soc.* **2000**, *122* (44), 10795-10804. DOI: Doi 10.1021/Ja000149a.
- (69) Hartshorne, S.; Richardson, D. J.; Simon, J. Multiple haem lyase genes indicate substrate specificity in cytochrome *c* biogenesis. *Biochem. Soc. Trans.* **2006**, *34* (Pt 1), 146-149. Almeida, M. G.; Silveira, C. M.; Guigliarelli, B.; Bertrand, P.; Moura, J. G.; Moura, I.; Leger, C. A needle in a haystack: the active site of the membrane-bound complex cytochrome *c* nitrite reductase. *FEBS Lett.* **2007**, *581*, 284-288.
- (70) Enemark, J. H.; Feltham, R. D. Principles of Structure, Bonding and Reactivity for Metal Nitrosyl Complexes. *Coord. Chem. Rev.* **1974**, *13*, 339-406.
- (71) Campechino, J.; Lagishetty, S.; Wawrzak, Z.; Alfaro, V. S.; Lehnert, N.; Reguera, G.; Hu, J.; Hegg, E. Cytochrome *c* nitrite reductase from the bacterium *Geobacter lovleyi* represents a new NrfA subclass. *J. Biol. Chem.* **2020**, *295*, 11455-11465.
- (72) Hoshino, M.; Ozawa, K.; Seki, H.; Ford, P. C. Photochemistry of Nitric-Oxide Adducts of Water-Soluble Iron(III) Porphyrin and Ferrihemoproteins Studied by Nanosecond Laser Photolysis. *J. Am. Chem. Soc.* **1993**, *115* (21), 9568-9575. Hoshino, M.; Maeda, M.; Konishi, R.; Seki, H.; Ford, P. C. Studies on the reaction mechanism for reductive nitrosylation of ferrihemoproteins in buffer solutions. *J. Am. Chem. Soc.* **1996**, *118* (24), 5702-5707.

Chapter 2 The expression, purification, and characterization of Cytochrome *c* Nitrite Reductase

2.1 Overview

The cytochrome *c* nitrite reductase (ccNiR) homologue that is studied by the Pacheco group is found in *Shewanella oneidensis*. However, the efficiency of the enzyme leads to low expression levels in the bacteria, which poses a problem when larger quantities are required for study. Unfortunately, due to the complex heme architecture utilized by ccNiR, recombinant expression in alternate organisms using more conventional techniques has proven difficult. Despite these complications, a method to promote overexpression of ccNiR in *S. oneidensis* was established in Youngblut et al.¹ Over the years, the original purification process has undergone many iterative modifications. This chapter describes the expression of *S. oneidensis*, a purification of ccNiR from the bacteria that incorporates all the latest improvements, and the methodology used to identify, quantify, and assess the purity of the enzyme. Lastly, this chapter presents a comparison of the ccNiR enzymatic activities of the *S. oneidensis* and *D. desulfuricans* homologues, obtained using the standard MV_{red} assay.

2.2. Materials and Methods

2.2.1. General instrumentation

Routine UV/Vis spectroscopy was performed using a CARY Bio 50 UV/Vis spectrophotometer. Two of these spectrophotometers are already placed inside nitrogen-filled gloveboxes (MBraun and Innovative Technologies) which provide an anaerobic environment. The oxygen level was strictly monitored and maintained at less than 2 ppm; the glovebox catalysts were regenerated with 5% or 7% Hydrogen (Airgas) once a month or whenever the

oxygen level rose above 2 ppm. The mass spectrum ccNiR was obtained using a Shimadzu MALDI-7090 MALDI-TOF Mass Spectrometer.

2.2.2. General Materials

All reagents were of high bio-grade purity and purchased from Thermo-Fisher, Dot Scientific, or MP Biomedicals, unless specified otherwise.

2.2.3. Large Scale *S. oneidensis* TSP-C cell culture for wild type ccNiR protein

Wild type ccNiR (wtccNiR) was obtained from an *S. oneidensis* TSP-C expression system first reported by Youngblut et al.² A petri dish containing autoclaved LB agarose and the antibiotics kanamycin (Kan, 50 µg/mL) and rifampicin (Rif, 30 µg/mL) was inoculated with *S. oneidensis* TSP-C cells containing the plasmid with the wtccNiR gene and incubated overnight at 30 °C. A single bacterial colony from the petri dish was suspended in 5mL LB (20 mg/mL), Kan (50 µg/mL), Rif (30 µg/mL) solution and was incubated for 10-11 hours in an incubator shaker at 200 rpm and 30 °C. After that period, 1 mL of bacterial culture was transferred into 1 L of the same medium, which was then incubated for 16 hours under the same conditions as in the first step. In a final step, 1 L of bacterial cell culture was transferred into a 50 L carboy that already contained 45 L LB, Kan (50 µg/mL), Rif (30 µg/mL) thermostated at 30 °C in a constant temperature water bath (Fig. 2.1). The culture was incubated for 16 - 18 hours at 30 °C while being continually sparged with compressed air, which served to agitate the culture suspension and to keep it aerated until late in the growth process when high bacterial density consumed oxygen faster than it could be replenished (Fig. 2.1). The cells were harvested from the 45 L cell culture by centrifuging aliquots in 1 L bottles for 10 minutes at 5,000 × *g*. The pooled cell pellets were resuspended using a buffer that contained 20 mM HEPES, 1mM EDTA pH=7.0 (final

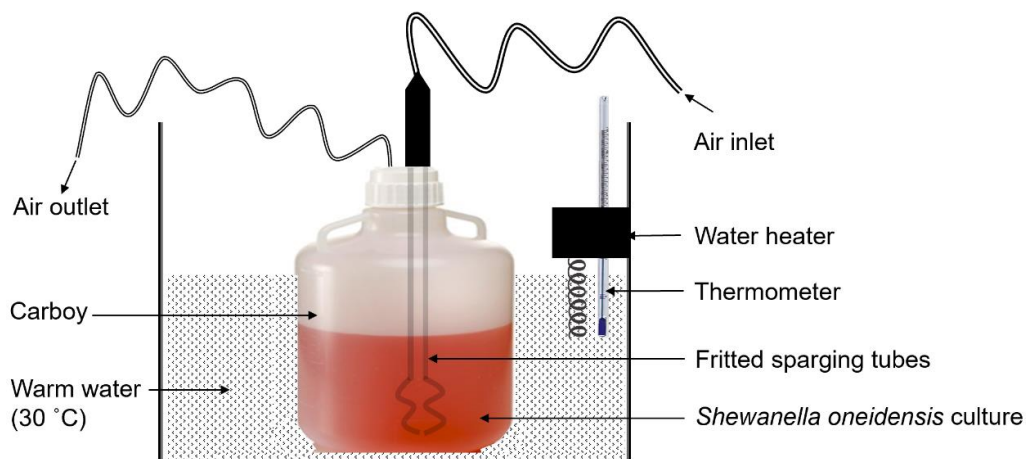


Figure 2.1. Large scale (45 L) *Shewanella oneidensis* culture for high amount wtccNiR enzyme purification. A carboy used for this culture was surrounded by water. A thermostat maintains the constant optimum temperature (30 °C). To keep the culture aerated and to avoid cell settling, two fritted sparging tubes inside of the carboy provided compressed air circulation that continuously agitated the culture.

volume ~500 mL), after which the two protease inhibitors leupeptin (1-10 μ M), AEBSF/PMSF (0.1 - 1.0 mM) were immediately added. The resuspended pooled cell pellet was frozen and stored at -80 °C in a stainless-steel beaker until needed.

Concentrated suspensions of cells containing the overexpressed wtccNiR were lysed by sonication in an ice-cooled stainless-steel beaker, using cycles of 30 s ultrasonic bursts at 70% amplitude followed by 45 s pauses, repeated for 10 minutes of sonication time. The lysed cell products were centrifuged for 30 minutes at 14,000 rpm (21,952 x g) and the supernatant solution was collected to remove cell debris. Finely ground ammonium sulfate (AS) was added very slowly to the solution, which was stirred with a magnetic stirrer, until the solution contained

50 % of the AS needed to saturate at 4 °C. Slow AS addition reduced unwanted ccNiR precipitation. The final mixed salt sample was centrifuged at 14,000 rpm (21,952 x g) for 30 min, and then the supernatant was collected.

In total, four columns were used to sequentially purify wtccNiR protein. First, the collected supernatant protein sample was loaded onto a 600 mL octyl-sepharose column (hydrophobic interaction chromatography, HIC, by GE Healthcare). This column was pre-equilibrated with a buffer that contained 3 M AS, 20 mM HEPES and 1 mM EDTA, adjusted to pH = 7.0 (Buffer A). The HIC column was deemed to be equilibrated when the UV reading at 280 nm of the column flow-through and the conductivity became constant. After the clarified cell extract had been loaded, the column was washed with Buffer A until the UV reading at 280 nm of the column flow-through was once again constant. The loaded protein sample was then washed with at least 2 column volumes of a mixture containing 60% Buffer A and 40% of a pH 7.0 low salt buffer containing 20 mM HEPES and 1 mM EDTA, pH = 7 (Buffer B) until the UV at 280 nm once again dropped to a stable baseline. The eluent contained mostly non ccNiR protein and nucleic acids and was discarded. In a third step, the column was washed with a solution containing 20% Buffer A and 80 % Buffer B. All fractions from this step for which the absorption reading at 280 nm deviated significantly from the baseline were pooled and transferred to Snake-Skin dialysis tubes (9 mL /1 cm, ThermoFisher) for dialysis at 4 °C for roughly 4 hours in a reservoir containing Buffer C (20 mM NaHEPES, 1 mM EDTA pH = 7.0) which was an optimum buffer for the second column, an 80 mL Q-sepharose anion exchange column (GE Healthcare). After 4 hours, the dialysis bags were transferred to a reservoir containing 4 L of fresh Buffer C, a process that was repeated a second time after a further 4 hours. The conductivity of the protein eluent solution was evaluated after the dialysis was

completed. It is imperative that, before proceeding to the next step, the conductivity of the eluent matches that of Buffer C.

The eluent was loaded onto the Q-sepharose column that had been pre-equilibrated with Buffer C, and the unretained flow-through was collected. The Q column retains only negatively charged proteins, and ccNiR is nearly neutral at pH = 7.0. **Important:** it is *critical* to employ buffer made with the HEPES sodium salt rather than the HEPES acid. HEPES buffer made with 20 mM HEPES acid has an ionic strength of 10 mM and at this ionic strength ccNiR binds weakly to Q-Sepharose, which greatly decreases the resolution. HEPES buffer made with 20 mM HEPES sodium salt has an ionic strength of 20 mM and passes through the column cleanly without binding.

The eluent buffer from the Q-Sepharose column was concentrated using a tangential flow filtration device (TFF,30 K, OAPMP220, Pall Life Sciences). After concentrating the volume from ~1L to 100mL, ground solid AS was added directly to the concentrated protein sample in order to match the conductivity of Buffer D (2 M AS, 20 mM HEPES, 1 mM EDTA). The sample was loaded onto a 3.5 mL RESOURCE isopropyl HIC column (GE Healthcare, capacity 25 mg protein/mL) that had been pre-equilibrated with Buffer D, and then eluted with a 0 to 100% gradient of Buffer B. CcNiR eluted at 20 – 30 % Buffer B, and was detectable as a sharp peak in the UV(280 nm) chromatogram.

After concentrating the ccNiR-containing samples and exchanging the enzyme buffer for one with 20 mM HEPES, 1 mM EDTA pH 7.0, using Pall centrifugal concentrator tubes, samples were run through a final 315 mL Hi-Prep 26/60 Sephacryl S100 High Resolution column. The column was equilibrated with buffer containing 150 mM NaCl, 20 mM HEPES, 1 mM EDTA pH = 7.0, after which the sample was loaded with a sample loading volume between

0.5-4% of the column volume (approx. 1.5-12 mL) and eluted using the same buffer used to equilibrate. There was an observable two band separation, the first band to elute being pure ccNiR. The purity of ccNiR was initially checked by UV/Vis spectrophotometry (pure ccNiR has an A_{409}/A_{280} absorbance ratio ≥ 4) and confirmed by observing a single band at ≈ 55 kDa via SDS-PAGE (Fig. 2.2). The ccNiR sample was concentrated and exchanged with the enzyme storage buffer (20 mM HEPES, 1 mM EDTA pH 7.0) using Pall centrifugal concentrator tubes and stored in 1 mL aliquots at -80 °C until needed.

2.2.4. Pyridine hemochromagen assay for determining the concentration of wtccNiR

The pyridine hemochromagen assay was performed to determine the concentration and the extinction coefficient spectrum of wtccNiR. The method used was similar to that described by Berry and Trumpower,³ and Barr and Guo,⁴ but with the following minor modifications. Briefly, Solution-I containing 10 mL 0.1 M potassium ferricyanide was mixed with 800 mL of 0.5 M NaOH, 800 mL of pyridine (Anhydrous, 99.8% pure, Sigma-Aldrich) and 390 mL nano-pure water to make 2 mL of Solution-II. The final concentrations in solution II were 500 mM $K_3[Fe(CN)_6]$, 0.2 M NaOH and 40% v/v pyridine. A solution containing equal volumes of Solution-II and 50 mM HEPES buffer, pH 7, was used to set the baseline for the UV/Vis spectrophotometer. CcNiR samples were dissolved in a 50 mM HEPES buffer, pH = 7.0, to make Solution-III. Equal volumes of Solution-II and Solution-III were mixed in a cuvette, and the UV/Vis spectrum was recorded in the range 450 nm – 800 nm. This was the oxidized pyridine hemochrome sample and was labeled as Dataset-1. A few grains of solid sodium dithionite (sodium hydrosulfite) were added into the cuvette, the solution was carefully mixed, and then several UV/Vis spectra were recorded at 30 s intervals until the spectra remained unchanged. The final spectrum was the reduced pyridine hemochrome sample and was labeled

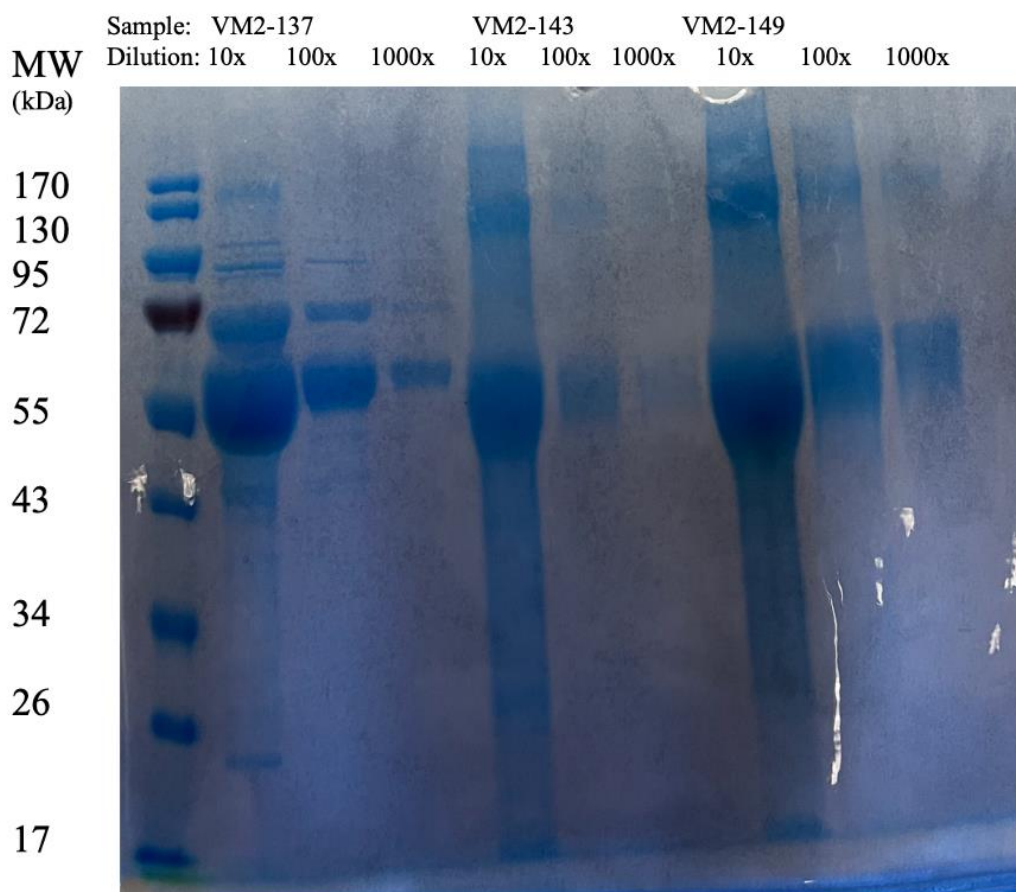


Figure 2.2. SDS-PAGE gel of various samples of purified protein. This gel corresponds to protein samples used for crystallography (Chapter 6). Each lane represents wild type CcNiR samples from separate purifications.

as Dataset-2; the reduced solution is distinctly pink, compared to the orange oxidized pyridine hemochrome. The difference spectrum (Dataset-2) – (Dataset-1) was fit in the range from 525 nm – 620 nm using the known extinction coefficient difference spectrum³ to determine the concentration of pyridine hemochrome in solution. This concentration was divided by 5 to obtain the ccNiR protomer concentration in the pyridine hemochrome solutions (as each ccNiR protomer contains 5 hemes), and then multiplied by 2 to obtain the ccNiR protomer

concentration in Solution-III. To obtain the extinction coefficient spectrum of ccNiR, the spectrophotometer baseline was first reset in the range from 250 nm – 800 nm with a 50 mM HEPES buffer, pH 7. A known volume of Solution-III was diluted to 1 mL such that the Soret band absorbance (409 nm) was ≤ 1.0 , and the UV/Vis spectrum was recorded from 250 nm – 800 nm. As the ccNiR concentration was known from the pyridine hemochrome assay, the extinction coefficient spectrum was readily obtained by dividing the absorbances collected between 250 nm and 800 nm by the concentration and pathlength (Beer's law). A complementary extinction coefficient spectrum for the lower intensity region from 500 nm – 800 nm was also obtained from less diluted samples of Solution-III.

2.2.5. Mass Spectrometry for mass confirmation of wtccNiR

Matrix Assisted Laser Desorption Ionization Time of Flight (MALDI-TOF) was performed in order to obtain the molecular mass of *S. oneidensis* ccNiR. A 1 μ M sample of ccNiR was exchanged into mass spectrometry grade water using small centricon tubes and the small centrifuge. The exchange of solvents was conducted three times. This was done to avoid interferences from the enzyme buffer. Next, a 1 μ L aliquot of sinapinic acid was transferred to the MALDI-TOF plate and left to dry and crystallize. Then, a 1 μ L aliquot of exchanged ccNiR was placed on the sinapinic acid sample and left to dry. Lastly, another 1 μ L aliquot of sinapinic acid was placed on the layered ccNiR and sinapinic acid and left to dry in order to form a “sandwich”. The plate was then inserted into the mass spectrometer for evaluation (Fig. 2.3).

2.2.6. The standard ccNiR activity assay using the methyl viologen monocation radical

The standard assay is used to obtain the specific activity of newly purified ccNiR and check for possible batch-to-batch variations. The assay was completed in an anaerobic glovebox, where the O₂ levels are limited to 2 ppm or less. Preparations for this assay provide a good

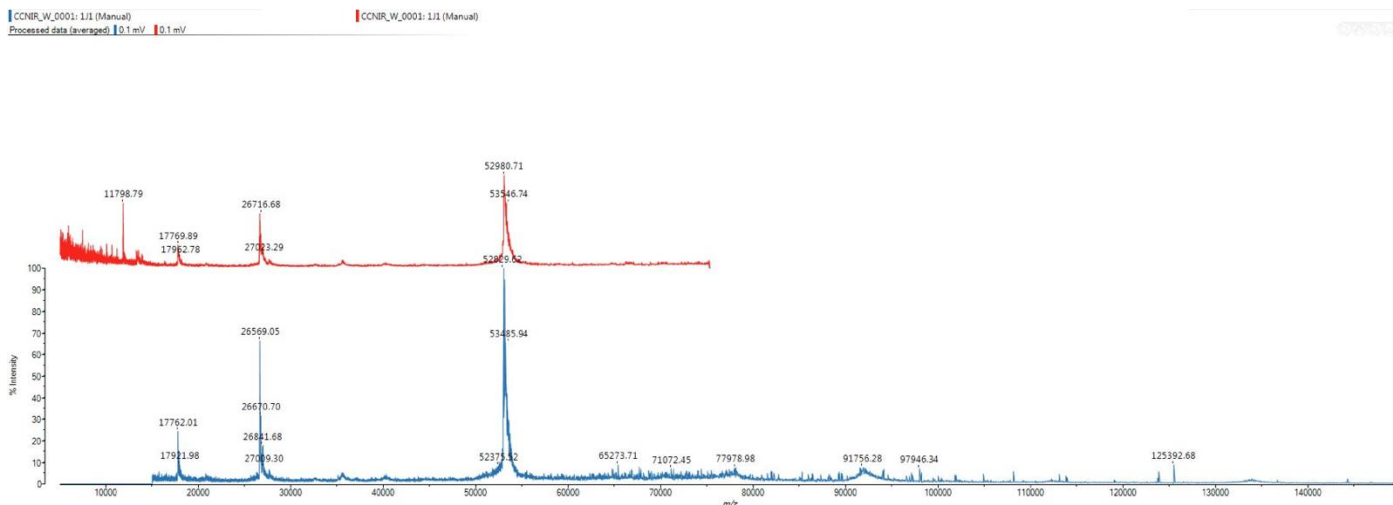


Figure 2.3. The spectrum in red represents the mass spectrum up to 800 m/z. The spectrum in blue shows the full spectrum up to 150,000 m/z. Both spectra show a peak around 52,000 - 53,000 m/z, which confirms the mass of a ccNiR protomer. The full spectrum shows a peak at ~125,000 m/z, which corresponds to the mass of the ccNiR dimer. This confirms the presence of ccNiR in the sample.

template for other experiments involving ccNiR and electrochemically prepared reducing agents and will be described in detail.

Small aliquots (~100 mL) of concentrated ccNiR stock solution were frozen and transferred into the glovebox antechamber in open vials. The antechamber was evacuated and refilled with nitrogen three to five consecutive times to fully exchange the air with pure nitrogen from the glovebox, after which the inner antechamber door could be opened to bring the still frozen air-free enzyme into the glovebox. Care should be taken to minimize the amount of time used in the pump-purge cycles so that the enzyme does not thaw during the process.

Dry assay ingredients were weighed outside the glovebox. For a typical experiment, 0.0206 g methyl viologen (MV_{ox}) and 0.0468 g of NaCl were weighed into one glass vial and

0.028 g NaNO_2 into a separate vial. The vials were covered with parafilm, through which a few holes were poked with a needle to allow gas to flow in and out, after which they were placed into the antechamber of the glovebox and degassed by the same procedure as described above for ccNiR. Within the glovebox, stock MV_{ox} and nitrite solutions were made by adding to each vial 4.0 mL of degassed assay buffer (50 mM HEPES, pH 7.0, made from HEPES free acid); the procedure for degassing buffers and bringing them into the glovebox is described in a separate standard operating procedure available in the Pacheco lab. **Note:** EDTA is not included in the assay buffer because, in the past, it has sometimes interfered with the assays. The final composition of the MV_{ox} stock was 20 mM MV_{ox} and 200 mM NaCl, while that of the stock nitrite was 100 mM NaNO_2 .

To prepare the reduced methyl viologen monocation radical (MV_{red}), the stock MV_{ox} was transferred to a bulk electrolysis cell and a potential of -700 mV vs SHE (~-900 mV vs the Ag/AgCl electrode used in the lab) was applied for 5 minutes, during which the current change with time was monitored. After the 5 minutes, the contents of the electrolysis cell were gently mixed with a 1-mL pipette, then the 5-minute electrolysis procedure was repeated up to 20 times, until the background current at the end of each cycle decreased below 50 mA. The applied potential of -700 mV vs SHE is ~250 mV below MV_{ox} 's midpoint potential (-449 mV vs SHE), which is sufficient to reduce most of the MV_{ox} , but not low enough to promote unwanted 2-electron reduced methyl viologen.

Two common technical problems with bulk electrolysis are drift in the reference electrode and a clogged junction or dirty buffer in the auxiliary electrode's salt bridge. To guard against reference electrode drift, the reference electrode was tested prior to almost every use by performing cyclic voltammetry on a solution of MV_{ox} . The MV_{ox} solution from the previous

section could be used for this purpose, and since CV doesn't harm the solution, the same stock could be used first for CV and then for bulk electrolysis to prepare MV_{red} . In the Epsilon/Basi software program for CV, the initial potential was set to 0 mV, the switching potential was set to -900 mV vs Ag/AgCl, the segment number to 2, the scan rate to 100 mV/s, and the scale was set to 1 mA. Two peaks, one with positive and one with negative current, should be detected between 0 and -900 mV vs Ag/AgCl. The potentials recorded for the two peaks must be added together and divided by two to give the midpoint potential, which should be about -649 mV vs Ag/AgCl (roughly -449 mV vs SHE, the known midpoint potential of MV_{ox}). If the measured differs significantly from -649 mV vs Ag/AgCl, the electrode must be tended to, or the bulk electrolysis procedure may not work.

To guard against a clogged junction or dirty buffer in the auxiliary electrode's salt bridge, the buffer in the salt bridge should be changed frequently (possibly after each electrolysis run, or after every other run), and the Vycor tip of the salt bridge should be changed if it gets dark and limits current. New Vycor tips will be yellow. The salt bridge (and indeed the reference electrode) junction may also be blocked by an air bubble, which can be difficult to detect. An air bubble at the salt bridge junction can be gently removed with a pipette, while one in the reference electrode can sometimes be dislodged by gently flicking the tip.

With an MV_{red} stock solution in hand, the standard assay proceeded as follows. To an Eppendorf tube were added 5 μ L of a 100 mM $NaNO_2$ solution, 100 μ L of an 800 pM solution of ccNiR, and 885 μ L of 50 mM HEPES pH=7.0 assay buffer. Lastly, 10 μ L of 10 mM MV_{Red} solution was added to the Eppendorf tube, at which point the assay solution was mixed and quickly transferred to a quartz cuvette where the reaction was monitored for 5 minutes at 15 second intervals using a UV-Vis spectrophotometer. MV_{red} exists as a mixture of monomer and

dimer in proportions that vary with total MV_{red} concentration and monitoring the 500 nm – 700 nm visible range allowed for the contributions from each species to be distinguishable. In the kinetic experiments, the rate of change in total MV_{red} was reported, where $(MV_{red})_{tot} = MV_{red} + 2(MV_{red})_2$.

MV_{red} is oxidized by nitrite even in the absence of ccNiR, and this background reduction must be subtracted. In addition, residual oxygen in the glovebox may also oxidize MV_{red} . To measure background MV_{red} oxidation, 500 μ M $NaNO_2$ were allowed to react with $\sim 100 \mu$ M MV_{red} in the absence of ccNiR for 5 minutes in 50 mM HEPES pH = 7.0 buffer. The uncatalyzed reaction rate was then subtracted from the catalyzed one. This background rate should typically be no greater than $\sim 3.57 \times 10^{-5}$ mM MV_{red} oxidized per second. Higher rates indicate the presence of substantial residual oxygen in the glovebox, which will make assays unreliable. Thus, the glovebox should be regenerated if an elevated MV_{red} oxidation background is observed.

2.3. Results of the Standard MV_{red} Assay

Upon completing the assay using the spectrophotometer, the datafiles are saved as CSV files. To analyze the data set, four Mathcad programs are used sequentially. The first program is called “Step 1 submatrix former.” The CSV file containing the data is uploaded into this program, which will display the first absorbance vs wavelength (in nm) spectrum in the time series. The program has sliders that can allow the user to trim from the spectrum any noisy or off-scale data; all other spectra in the time series will be similarly trimmed. For the standard assay, one usually keeps data above 500 nm that include the MV_{red} absorbance maximum at 600 nm, and discards data from 200 nm – 500 nm that are often off scale. The program saves the

trimmed data set (upon command from the user), and this trimmed file is called by the “Step 2 data extractor” after the user opens it.

The second program takes the data prepared by the first program, and upon being supplied by the user with the time interval between spectra (typically 15s), reformats the data into a matrix that contains times in the first column, wavelengths in the first row, and absorbances in every other cell of the array (the cell at the intersection of the first row and first column is left as zero). This matrix is exported as a file named “reformatted data.csv”, to be used by the third program.

The third program, called “Step 3 SVD-wavelength in rows” is opened next. This program inputs the reformatted data and first separates the data into three distinct matrices: a matrix of wavelengths (extracted from the first row of “reformatted data.csv”), one of times (extracted from the first column of “reformatted data.csv”), and one of absorbances, obtained from the corresponding cells of “reformatted data.csv”. The program then performs singular value decomposition (SVD) on the absorbance matrix.⁵ A slider allows the user to plot each column of the SVD U matrix vs wavelength, and each column of the SVD V matrix vs time. For the standard assay, the first two columns of the U and V matrices will typically have signal, while the remaining ones will look like noise, showing that only two components are contributing to all the time-resolved spectra. If the slider is set to 1, the program reconstructs a “clean” absorbance matrix using only the first two columns of U and V, together with the first two singular values from the S matrix (in Mathcad, the first row and column of an array have a zero index).⁵ Chemically, the two components correspond to the monomer MV_{red} and the dimer MV_2 , as MV_{ox} does not absorb above 500 nm. The step 3 program exports three separate csv files, one containing the wavelengths, one the times, and the third the absorbance matrix

reconstructed using only the non-noise columns of the U and V matrix, and the corresponding singular values.⁵

Finally, the fourth Mathcad program, referred to as “Step 4 Model fit”, takes as input the three output files from the Step 3 program and fits the SVD-processed absorbance spectra using the independently known extinction coefficient spectra of MV_{red} and MV_2 to obtain the concentrations of each species as a function of time. From this, the total methyl viologen monocation radical concentration was obtained as $(MV_{red})_{tot} = MV_{red} + 2(MV_{red})_2$, after which the initial rate of $(MV_{red})_{tot}$ was obtained from a least-squares fit of the linear part of a $(MV_{red})_{tot}$ vs t plot. The first data set to be analyzed was the blank containing no enzyme, after which the uncatalyzed rate was subtracted from the initial rates of all assays obtained in the presence of ccNiR. In the Step 4 program, a variable labeled “uncat” will be highlighted in blue; for the blank, “uncat” is set to zero. The initial rate is output as the variable “Inrate”, while the initial rate with the background subtracted is output as $Inrate_{corr}$, which is calculated as the difference $Inrate - uncat$.

In the standard assay, a saturating nitrite concentration is used, so k_{cat} (in s^{-1}) for the ccNiR sample can be calculated as $Inrate_{corr}/[ccNiR]$ (the initial rate is independent of $(MV_{red})_{tot}$, at least down to 20 mM).⁶ The k_{cat} parameter provides a direct measure of the ccNiR batch’s specific activity. The k_{cat} values for a representative set of purified ccNiR batches are presented in Table 2.1.

2.4. Discussion of the Standard MV_{red} Assay

The standard assay was performed after almost every purification to evaluate the specific activity of the enzyme. Protein purification can lead to a decreased enzyme activity, especially in a long protocol such as that required to purify ccNiR from *Shewanella oneidensis*. Table 2.1 lists

Enzyme	Bacterial Source	k_{cat} (s^{-1}) at pH=7.0
wtccNiR (VM2-137)	<i>Shewanella oneidensis</i>	5400
wtccNiR (VM2-143)	<i>Shewanella oneidensis</i>	3950
wtccNiR (VM2-149)	<i>Shewanella oneidensis</i>	5380
ccNiR (NrfA:NrfH)	<i>Desulfovibrio desulfuricans</i>	5721
wtccNiR (Youngblut)	<i>Shewanella oneidensis</i>	4944
wtccNiR (Alam)	<i>Shewanella oneidensis</i>	3600
wtccNiR (Shahid)	<i>Shewanella oneidensis</i>	4666

Table 2.1. A comparison of the k_{cat} values for different protein purifications of the *S. oneidensis* ccNiR, as well as the *D. desulfuricans* ccNiR provided by Gabriela Almeida (Instituto Universitario Egas Moniz, Portugal).

the k_{cat} values obtained from several representative purifications, by different researchers, over a twelve-year span. These values range from 3600-5400 s^{-1} at pH=7.0. Some of the observed variation in activity reflects real differences in enzyme quality from batch to batch; however, several Pacheco group researchers over the years have also observed significant variability (as much as 7% – 10%) when repeatedly measuring the k_{cat} value for a single ccNiR batch. This variability is primarily due to the fact that activity is quickly lost if ccNiR samples more dilute than $\sim 10^{-7}$ M are left standing, even though solutions with concentrations of 10^{-6} M or greater are stable for days. To mitigate this effect, the ~ 80 pM ccNiR present in the assay reaction mixture was diluted in multiple steps from ~ 1 mM stocks for each assay, and the partially diluted solutions were discarded immediately after the assay.

The standard assay was completed not only with ccNiR from *S. oneidensis*, but also from the *Desulfovibrio desulfuricans* homologue. As noted in Chapter 1, Section 1.9, the *D. desulfuricans* homologue differs from the *S. oneidensis* ccNiR in an interesting way. The *S.*

oneidensis homologue contains five c-type hemes, whereas *D. desulfuricans* contains nine c-type hemes in a heterodimeric assembly. The large number of hemes in *D. desulfuricans* can be attributed to the enzyme being a NrfA:NrfH adduct, therefore for every five hemes of NrfA, there will be four hemes from NrfH.⁷ As can be seen in Table 2.1, despite the structural differences between the homologues, and the extra four c-type hemes found in *D. desulfuricans*, the activities of the enzyme homologues were quite comparable.

2.5 References

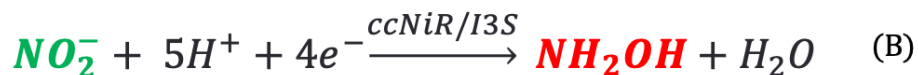
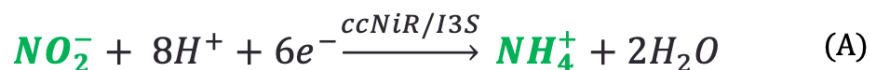
- (1) Youngblut, M.; Pauly, D. J.; Stein, N.; Walters, D.; Conrad, J. A.; Moran, G. R.; Bennett, B.; Pacheco, A. A. *Shewanella oneidensis* cytochrome c nitrite reductase (ccNiR) does not disproportionate hydroxylamine to ammonia and nitrite, despite a strongly favorable driving force. *Biochemistry* **2014**, *53*, 2136-2144.
- (2) Youngblut, M.; Judd, E. T.; Srajer, V.; Sayyed, B.; Goelzer, T.; Elliott, S. J.; Schmidt, M.; Pacheco, A. A. Laue crystal structure of *Shewanella oneidensis* cytochrome c nitrite reductase from a high-yield expression system. *J Biol Inorg Chem* **2012**, *17* (4), 647-662. DOI: 10.1007/s00775-012-0885-0.
- (3) Berry, E. A.; Trumpower, B. L. Simultaneous determination of hemes a, b, and c from pyridine hemochrome spectra. *Anal Biochem* **1987**, *161* (1), 1-15. DOI: 10.1016/0003-2697(87)90643-9.
- (4) Barr, I.; Guo, F. Pyridine hemochromagen assay for determining the concentration of heme in purified protein solutions. *Bio. Protoc.* **2015**, *5*, (18).
- (5) Press, W. H.; Teukolsky, S. A.; Vetterling, W. T.; Flannery, B. P. Numerical Recipes the art of scientific computing. 3rd ed.; Cambridge University Press, 2007; pp 65-75. Henry, E. R.; Hofrichter, J. Singular Value Decomposition: Application to Analysis of Experimental Data. In *Meth. Enzymol.*, Brand, L., Johnson, M. L. Eds.; Vol. 210; Academic Press, 1992; pp 129-192.
- (6) Alam, S. The Effects of an R103Q Mutation on the Chemical and Physical Properties of the Enzyme Cytochrome C Nitrite Reductase (ccNiR). University of Wisconsin - Milwaukee, 2022.
- (7) Cunha, C. A.; Macieira, S.; Dias, J. M.; Almeida, G.; Goncalves, L. L.; Costa, C.; Lampreia, J.; Huber, R.; Moura, J. J. G.; Moura, I.; et al. Cytochrome c nitrite reductase from *Desulfovibrio desulfuricans* ATCC 27774 - The relevance of the two calcium sites in the structure of the catalytic subunit (NrfA). *J. Biol.Chem.* **2003**, *278* (19), 17455-17465. DOI: 10.1074/jbc.M211777200.

Chapter 3 The test for hydroxylamine side product generation during ccNiR catalyzed reduction of nitrite under weakly reducing conditions

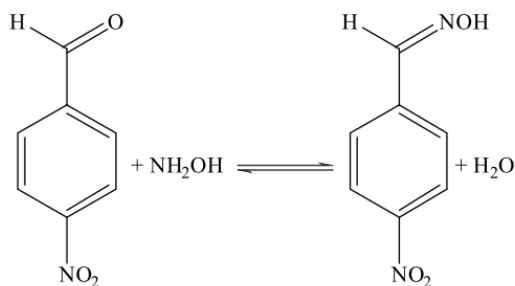
3.1. Overview

The ccNiR- catalyzed reduction of nitrite was previously modelled using computational methods by Bykov and Neese (Scheme 1.2, Chapter 1).¹ In steps 5 and 6 of the proposed mechanistic model (Scheme 1.2), hydroxylamine is bound in the active site. A proton transfer to the oxygen of hydroxylamine must then occur, followed by a dehydration (Scheme 1.2, step 7) which is energetically costly. Previous experimental results from the Pacheco group are consistent with steps 6 and 7 of the Scheme 1.2 mechanism being overall rate-limiting in the nitrite reduction to ammonia at pH 7.0. The question addressed in this chapter is whether, under certain conditions, hydroxylamine might be released from the intermediate species proposed to be present at the end of step 5 in Scheme 1.2. No such release is detected when the strong reductant MV_{red} is the electron source, but we wanted to explore the possibility that hydroxylamine release could compete with the putative rate limiting steps 6 and 7 of Scheme 1.2 when weaker reductants were used. Scheme 3.1 summarizes this conjecture for the case where 50% reduced indigo trisulfonate (I3S), is used as an electron source.

There are few assays for detecting micromolar concentrations of hydroxylamine, and of these, perhaps the most straightforward is one reported by Johnson in 1968 (hereafter referred to as the “Johnson assay”).² The basis of this assay is simple, as shown in Scheme 3.2. If there is hydroxylamine present in the reaction mixture, and 4-nitrobenzaldehyde is added to it, then upon heating, the hydroxylamine and 4-nitrobenzaldehyde will react to form an oxime product. The



Scheme 3.1. The possible outcomes of the ccNiR-catalyzed reduction of nitrite in the presence of partially reduced Indigo trisulfonate (I3S). **A.** The six-electron reduction of nitrite to ammonium by ccNiR using I3S as a reducing agent. **B.** The four-electron reduction of nitrite to hydroxylamine by ccNiR using I3S as a reducing agent.



Scheme 3.2. The reaction between hydroxylamine and *p*-nitrobenzaldehyde to form the oxime product measurable by UV-Visible Spectrophotometry.²

oxime absorbs light at 368 nm, so if a band appears at this wavelength, it can be assumed that hydroxylamine is present in the solution.²

3.2. Materials and methods

3.2.1. General materials

Sodium nitrite was purchased from Acros Organics; Ammonium sulfate (AS), EDTA and HEPES free acid and sodium salt were obtained from Fisher Scientific, nitrogen gas (high purity grade) from Airgas. Wild type *S. oneidensis* ccNiR was purified as described in Chapter 2.

Potassium Indigo Trisulfonate, Hydroxylamine, 4-Nitrobenzaldehyde, Hydrochloric Acid, and Sodium Hydroxide were all received from Millipore Sigma.

3.2.2. General instrumentation

Cary 50 (Varian) spectrophotometers were used to record the UV/vis spectral data. Two of these spectrophotometers are housed in gloveboxes. The gloveboxes (MBraun and Innovative Technologies) were used to maintain anaerobic conditions while recording UV/vis spectra or doing controlled potential electrolysis. The gloveboxes are filled with high purity nitrogen (Airgas, 99.99 % pure), which is continually circulated through an oxygen scrubber to maintain an oxygen level of less than 2 ppm. The glovebox scrubbers were regenerated with 5% or 7% Hydrogen (Airgas) at least once a month, or whenever the oxygen level rose above 2 ppm. BASi Epsilon EC potentiostats were used to measure spectropotentiometric data and to reduce required reagents at the appropriate potentials. An Ag/AgCl electrode (BASi model RE-5B) was used as the reference, and routinely calibrated against the methyl viologen midpoint potential as described in Chapter 2. Concentrations of ccNiR stocks were obtained by fitting UV/Vis spectra with the ccNiR extinction coefficient spectrum independently obtained using the pyridine hemochromagen assay,³ as described in Chapter 2.

3.2.3. Preparation of reduced indigo trisulfonate

The reduction of I3S was completed in the glovebox to ensure that there was no oxygen present. To a clean glass vial were added 0.012 g of I3S and 0.046 g of NaCl, after which the vial was transferred into the glovebox using the procedure described in Chapter 2 for methyl viologen. A solution with 5 mM I3S and 200 mM NaCl was then made by adding 4 mL of 50 mM HEPES pH 7.0 buffer to the vial. This solution was transferred to the bulk electrolysis cell and a potential of -90 mV vs SHE (-290 mV vs Ag/AgCl) was applied for 10 min. The solution

in the cell was gently mixed with a 1-mL pipette, after which it was subjected twice more to 10-minute electrolysis bursts at -90 mV vs SHE. The applied potential coincides with the midpoint potential of I3S, so after electrolysis, the solution should contain 50% I3S_{red} (2.5 mM). Fully oxidized, the solution starts as a dark blue color, and once the solution was partially reduced, it should be a green/aqua in color. Pure I3S_{red} is yellow. This solution can be stored in the glovebox refrigerator for a week and not undergo significant changes.

For the experiments described later in this chapter, 1.6 mL of the electrolyzed solution were diluted to 4.0 mL with assay buffer, to produce a solution containing 2 mM total I3S, or 1 mM I3S_{red}. This will be referred to below as the 1 mM I3S_{red} stock solution.

3.2.4. Johnson assay calibration curve

In preparation for the assay, the following stock solutions were prepared. A 600 mM solution of hydrochloric acid was made by transferring 5 mL of 12 M HCl to a 100 mL volumetric flask, then making up to the mark with nanopure water. A 0.3 M solution of sodium hydroxide was prepared by diluting 0.6 g of NaOH to volume with nanopure water in a 50 mL volumetric flask. Note that the NaOH solution must be prepared daily. A 13 mM 4-nitrobenzaldehyde solution was prepared by weighing out 0.2 g of 4-nitrobenzaldehyde into a 100 mL volumetric flask. A 50 mL aliquot of ethanol was transferred to the flask using a volumetric pipette, after which the solution was made up to the mark with nanopure water. Finally, a 10 mM hydroxylamine hydrochloride stock solution was produced by measuring 0.0695 g of hydroxylamine hydrochloride in to a 100 mL volumetric flask, adding 10 mL of nanopure water, and then diluting to the mark with ethanol.

Five different standard solutions ranging from 100-500 μ M hydroxylamine in 100 μ M increments were prepared. This was done by adding 0.5, 1.0, 1.5, 2.0, and 2.5 mL of 10 mM

stock hydroxylamine solution into five different 50 mL volumetric flasks. Each of these solutions was diluted to volume with ethanol. Next, the reaction solutions were prepared. A blank containing no hydroxylamine was prepared by adding 1 mL of ethanol and 1 mL of 4-nitrobenzaldehyde stock into a graduated test tube. This was referred to later as standard 0. Standards 1-5 were prepared in separate test tubes by adding 1 mL of the 100 μ M, 200 μ M, 300 μ M, 400 μ M, and 500 μ M hydroxylamine solutions prepared above to 1-mL aliquots of 4-nitrobenzaldehyde stock solution. The six test tubes containing standards 0-5 were then placed in a 90 °C water bath, with a piece of aluminum foil covering the tubes, and the solutions were heated for thirty minutes, during which time the solution volume decreased to ~0.5 mL due to solvent evaporation. After the thirty minutes, the test tubes were removed from the water bath, left to cool for at least 10 minutes.

Formation of the oxime product was determined by appearance of the 368 nm peak in the absorbance spectrum (Fig. 3.1). For obtaining the UV/Vis spectra, the spectrophotometer's baseline was set with a solution made by adding 1.5 mL of 0.3 M sodium hydroxide to a graduated test tube and diluting to 8 mL with ethanol. All spectrophotometric measurements, including the baseline, were made in semimicro quartz cuvettes with 1-cm pathlengths. For the standard curve, it was best to begin with the highest concentrated standard (standard 5). To the cooled standard 5 test tube were added first 5 mL of ethanol and then 1.5 mL of 0.3 M sodium hydroxide. Lastly, the solution was diluted to the 8 mL mark of the test tube with more ethanol. The solution was diluted 2-fold more by combining 500 μ L of it with 500 μ L of ethanol in an Eppendorf tube. The contents of the Eppendorf tube were then quickly transferred to a cuvette and the UV/Vis spectrum collected. The procedure was repeated for the remaining standard solutions. A plot of absorbance at 368 nm vs the concentration of hydroxylamine (as oxime) in

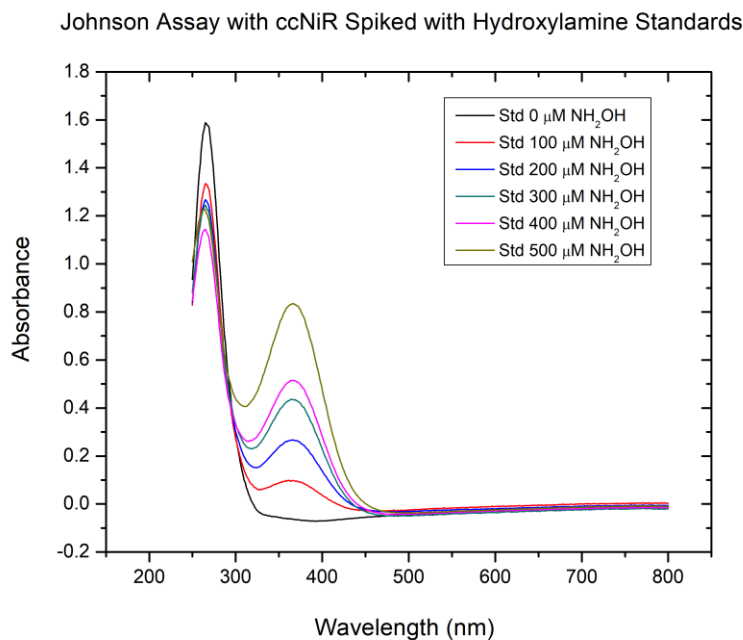


Figure 3.1. Spectra of the reaction mixtures containing a 1 μM ccNiR, 60 μM partially reduced Indigo trisulfonate, and 500 μM Nitrite, with a known amount of hydroxylamine at concentrations ranging from 100-500 μM .

the cuvette after the final dilution was linear, (red trace, Fig. 3.2) and a least-squares fit generated an extinction coefficient value of $2.6 \times 10^4 \text{ M}^{-1}\text{cm}^{-1}$ for the oxime.

3.2.5. Johnson assay as a test for ccNiR-catalyzed hydroxylamine generation

To test whether hydroxylamine was generated during ccNiR-catalyzed reduction of nitrite by I3S_{red}, six replicates of a reaction mixture were prepared by anaerobically mixing in each of six Eppendorf tubes 120 μL of I3S_{red} stock solution (Section 3.2.3), 5 μL of 100 mM NaNO₂ stock (Section 2.2.6), 25 μL of 60 μM ccNiR stock, and 850 μL of assay buffer (1.0 mL total volume in the Eppendorf tube). The concentrations of the species in solution were thus 120 mM I3S_{red}, 500 mM NO₂⁻, and 1.5 mM ccNiR. The six reaction mixtures were allowed to incubate in

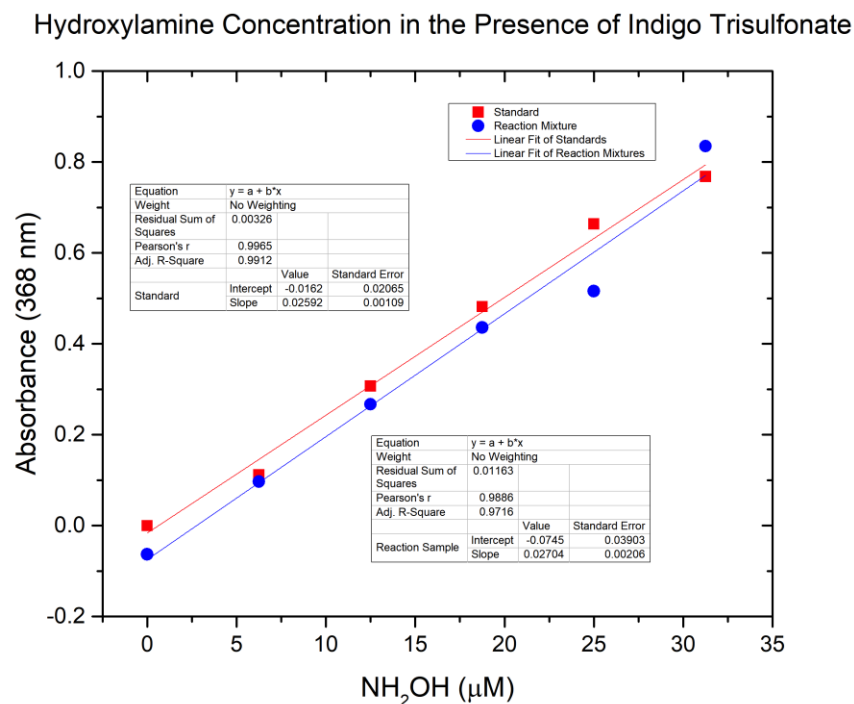


Figure 3.2. A comparison of the standard curve to the linear fit of the reaction mixtures.

the glovebox for 15 min, after which they were removed from the glovebox and centrifuged for 5 minutes at 13,000 rpm in a centrifugal concentrator to remove the ccNiR from the solutions.

Six assay mixtures were prepared in graduated test tubes as follows. One of the six filtered reaction mixtures was combined with 1 mL of 4-nitrobenzaldehyde stock, while each of the remaining five reaction mixtures was combined with 1 mL of one of the hydroxylamine stock solutions from Section 3.2.4 that ranged from 100-500 μM concentration, and 1 mL of 4-nitrobenzaldehyde stock. The assay mixtures were covered with foil and heated for thirty minutes at 90 °C, during which time the solution volumes decreased to less than 1 mL due to solvent evaporation. After thirty minutes, the test tubes were removed from the water bath and left to cool for at least 10 minutes. Once again, the assay mixture that was spiked with standard 5

(500 mM stock hydroxylamine) was assessed first. To the assay mixture were added 5 mL of ethanol and 1.5 mL of 0.3 M sodium hydroxide, after which the mixture was diluted to 8 mL with ethanol. The assay solution was diluted 2-fold more by combining 500 μ L of it with 500 μ L of ethanol in an Eppendorf tube. The contents of the Eppendorf tube were then quickly transferred to a cuvette and the UV/Vis spectrum collected. The procedure was repeated for the remaining assay mixtures. A plot of absorbance at 368 nm vs the concentration of added hydroxylamine (as oxime) in the cuvette after the final dilution was linear, (blue trace, Fig. 3.2) and a least-squares fit generated a slope and intercept very close to that seen for the standard curve (red trace, Fig. 3.2).

<i>Hydroxylamine Concentration (μM)</i>	<i>Standard Abs</i>	<i>Reaction Mixture Abs</i>
0.00	0.00	-0.0632
6.25	0.112	0.0974
12.50	0.307	0.267
18.75	0.482	0.436
25.00	0.664	0.516
31.25	0.768	0.835

Table 3.1. The final concentration of hydroxylamine calculated to be present in the standards and the spiked reaction mixtures. The absorbances for the standards and the reaction mixtures are listed in the table and correspond to those plotted in Figure 3.2.

3.3. Results and discussion of the Johnson assay

Scheme 3.3 summarizes the stoichiometry for nitrite reduction to hydroxylamine by I3S_{red}. I3S_{red} is a 2-electron donor, so 2 equivalents are required to reduce nitrite by 4 electrons to

hydroxylamine. In the experiment described in Section 3.2.5, 120 mM I3S_{red} would supply enough electrons to reduce at most 60 mM of nitrite to hydroxylamine, which after dilution to



Scheme 3.3. Half-reactions for nitrite oxidation to hydroxylamine and I3S_{red} oxidation, and the net reaction for nitrite reduction to hydroxylamine by I3S_{red}. The reactions show that 2 equivalents of I3S_{red} are required to reduce one equivalent of nitrite to hydroxylamine.

generate the assay buffer, would be decreased to 7.5 mM. Given the calculated extinction coefficient of oxime at 368 nm (Section 3.2.4), 7.5 mM of extra oxime added to the solutions spiked with varying amounts of added hydroxylamine stock would shift the intercept of the blue trace in Fig. 3.2 up by 0.195 absorbance units. Clearly, this is not observed, either in Fig. 3.2 or in the values tabulated in Table 3.1. Indeed, given the r-squared values of the two fits (0.9912 for the standard and 0.9716 for the reaction mixture), the data sets appear to be statistically identical. To explore this possibility more rigorously, a t-test was completed to compare the two data sets. In applying a two-tailed test, the degrees of freedom value used was 10. The first equation in Scheme 3.4 was used to obtain a calculated T (T_{calc}) value of 0.2265, after which Table 3.2 was used to find the tabulated T (T_{tab}) value for 10 degrees of freedom. The T_{calc} value can be compared to the T_{tab} value at various confidence levels. From 50-99.95% confidence levels, T_{calc} was less than T_{tab}, therefore it can be concluded with 99.95% confidence that the two sets of data (standard absorbances vs reaction mixture absorbances) are not significantly different from each other. Conversely, if the data sets are not significantly different from each other, then the

reaction mixture contributed negligible amounts of hydroxylamine to the assay mixtures of Fig 3.2. This result is important because it shows that release of free hydroxylamine from ccNiR is minimal even under conditions where a catalytic intermediate that has hydroxylamine bound to the active site might be building up during the catalytic cycle.

$$t_{calc} = \frac{|\bar{x}_1 - \bar{x}_2|}{S_{pooled}} \sqrt{\frac{n_1 n_2}{n_1 + n_2}} \quad (\text{A})$$

$$S_{pooled} = \sqrt{\frac{s_1^2(n_1 - 1) + s_2^2(n_2 - 1)}{n_1 + n_2 - 2}} \quad (\text{B})$$

Scheme 3.4. Equations used to complete a t-test. **A.** The t_{calc} value obtained by evaluating the means of two data sets, the number of values in each data set, and the S_{pooled} value. **B.** The S_{pooled} value obtained from the standard deviations of the two data sets, the number of values in the data set, and the degrees of freedom.

t Table											
cum. Prob	t (0.50)	t (0.75)	t (0.80)	t (0.85)	t (0.90)	t (0.95)	t (0.975)	t (0.99)	t (0.995)	t (0.999)	t (0.9995)
one-tail	0.50	0.25	0.20	0.15	0.10	0.05	0.025	0.01	0.005	0.001	0.0005
two-tails	1.00	0.50	0.40	0.30	0.20	0.10	0.05	0.02	0.01	0.002	0.001
df											
1	0.000	1.000	1.376	1.963	3.078	6.314	12.71	31.82	63.66	318.31	636.62
2	0.000	0.816	1.061	1.386	1.886	2.920	4.303	6.965	9.925	22.327	31.599
3	0.000	0.765	0.978	1.25	1.638	2.353	3.182	4.541	5.841	10.215	12.924
4	0.000	0.741	0.941	1.190	1.533	2.132	2.776	3.747	4.604	7.173	8.61
5	0.000	0.727	0.920	1.156	1.476	2.015	2.571	3.365	4.032	5.893	6.869
6	0.000	0.718	0.906	1.134	1.440	1.943	2.447	3.143	3.707	5.208	5.959
7	0.000	0.711	0.896	1.119	1.415	1.895	2.365	2.993	3.499	4.785	5.408
8	0.000	0.706	0.889	1.108	1.397	1.860	2.306	2.896	3.355	4.501	5.041
9	0.000	0.703	0.883	1.100	1.383	1.833	2.262	2.821	3.25	4.297	4.781
10	0.000	0.700	0.879	1.093	1.372	1.812	2.228	2.764	3.169	4.144	4.587
11	0.000	0.697	0.876	1.088	1.363	1.796	2.201	2.718	3.106	4.025	4.437
12	0.000	0.695	0.873	1.083	1.356	1.782	2.179	2.681	3.055	3.93	4.318
Z	0.000	0.674	0.842	1.036	1.282	1.645	1.96	2.326	2.576	3.090	3.291
	0%	50%	60%	70%	80%	90%	95%	98%	99%	99.80%	99.90%
	Confidence		Level								

Table 3.2. T-test table.

3.4 References

- (1) Bykov, D.; Neese, F. Substrate binding and activation in the active site of cytochrome *c* nitrite reductase: a density functional study. *J. Biol. Inorg. Chem* **2011**, *16*, 417-430. Bykov, D.; Neese, F. Reductive activation of the heme iron-nitrosyl intermediate in the reaction mechanism of cytochrome *c* nitrite reductase: a theoretical study. *J. Biol. Inorg. Chem.* **2012**, *17* (5), 741-760. Bykov, D.; Plog, M.; Neese, F. Heme-bound nitroxyl, hydroxylamine, and ammonia ligands as intermediates in the reaction cycle of cytochrome *c* nitrite reductase: a theoretical study. *J. Biol. Inorg. Chem.* **2014**, *19*, 97-112. Bykov, D.; Neese, F. Six-electron reduction of nitrite to ammonia by cytochrome *c* nitrite reductase: insights from density functional theory studies. *Inorg. Chem.* **2015**, *54*, 9303-9316.
- (2) Johnson, D. P. Spectrophotometric determination of oximes and unsubstituted hydroxylamine. *Anal. Chem.* **1968**, *40*, 646-648.
- (3) Berry, E. A.; Trumpower, B. L. Simultaneous determination of hemes a, b, and c from pyridine hemochrome spectra. *Anal. Biochem.* **1987**, *161*, 1-15. Barr, I.; Guo, F. Pyridine hemochromagen assay for determining the concentration of heme in purified protein solutions. *Bio. Protoc.* **2015**, *5*, (18).

Chapter 4 The quantification of ammonium present in solution after the ccNiR-catalyzed reduction of nitrite under weakly reducing conditions

4.1. Overview

The goal of the work described in this chapter was to quantify the amount of ammonium that was generated when ccNiR mediated the reduction of nitrite by a series of weak reductants. Earlier studies in the Pacheco lab had shown that no ammonium is generated from the ccNiR-mediated reaction of nitrite with the very weak reductants ferrocyanide or *N,N,N',N'*-tetramethyl-*p*-phenylenediamine (TMPD), but that ccNiR catalyzed the very slow 1-electron reduction of nitrite to $\text{NO}\cdot$ under these conditions.^{1,2} The Chapter 3 experiments from this thesis showed that hydroxylamine, another possible side-product of partial nitrite reduction, was not produced in detectable quantities when ccNiR mediated the reaction between nitrite and reduced indigo trisulfonate (I3S_{red}). However, as will be seen in Chapter 5, when I3S_{red} is mixed with an excess of nitrite in the presence of ccNiR, all the I3S_{red} re-oxidizes over time. This raises the question that the work of this chapter answers: do I3S_{red} and other weak reductants reduce nitrite exclusively to ammonium as does MV_{red} ? I3S_{red} is a more potent reducing agent than ferrocyanide or TMPD, but still significantly weaker than the MV_{red} used in the standard assay, so the answer to the question wasn't obvious a priori.

In 1985, Bergmeyer and Beutler published a method that allowed for not only the detection of ammonium, but also for its quantification. The method is summarized in step 2 of Scheme 4.1. Briefly, a test sample containing an unknown amount of ammonium is mixed into a solution that contains nicotinamide adenine dinucleotide (NADH), α -ketoglutarate (α -KG), and

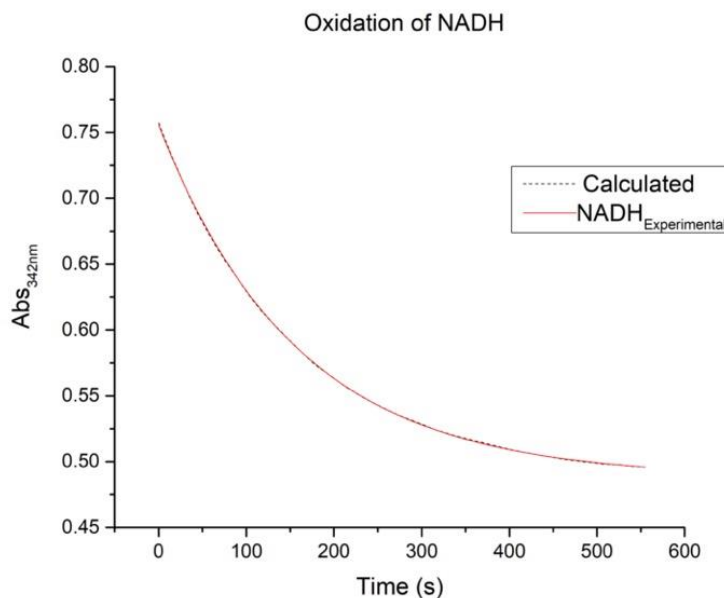
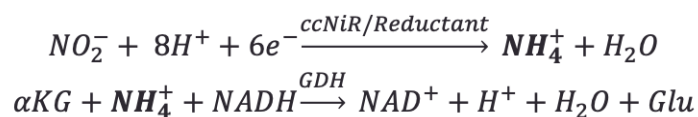


Figure 4.1. Spectral trace at 342nm corresponding to the oxidation of NADH to NAD⁺ over time.



Scheme 4.1. A. The six electron reduction of nitrite to ammonium catalyzed by ccNiR in the presence of a weak reductant. **B.** The glutamate dehydrogenase catalyzed reduction of α -ketoglutarate to glutamate using NADH as an electron donor. NADH oxidation to NAD⁺ can be correlated with the concentration of ammonium in solution.

the enzyme glutamate dehydrogenase (GDH). GDH catalyzes the reductive amination of α -KG by NADH, which generates glutamate (Glu) and NAD⁺. If reaction conditions are set such that α -KG and NADH are in excess of expected ammonium concentrations, then the amount of α -KG and NADH consumed will be limited by the ammonium concentration. The Scheme 4.1 reaction

can be monitored by UV/Vis spectrophotometry as NADH absorbs light at 340 nm while NAD⁺ does not; the amount of NADH consumed is thus determined from the change in absorbance at 340 nm (Fig. 4.1), and since NADH and ammonium are consumed in equimolar proportion, the amount of NADH consumed will directly reflect the amount of ammonium initially present in solution.

For the experiments described in this chapter, the Bergmeyer and Beutler assay was used to quantify the amount of ammonium generated when nitrite reacted with partially reduced I3S (by an applied potential of -90 mV vs SHE), fully reduced I3S (by an applied potential of -290 mV vs SHE), fully reduced Indigo tetrasulfonate (I4S_{red}) (by an applied potential of -230 mV vs SHE), and fully reduced hexaammineruthenium (Ru^{II}) (by an applied potential of -100 mV vs SHE), in the presence of ccNiR.

4.2. Materials and Methods

4.2.1. General materials

Sodium nitrite was purchased from Acros Organics; Ammonium sulfate (AS), EDTA and HEPES free acid and sodium salt were obtained from fisher scientific, Nitrogen gas (high purity grade) from Airgas. Wild type *S. oneidensis* ccNiR and ccNiR variants were purified as described in Chapter 2. Potassium indigo tetrasulfonate, potassium indigo trisulfonate, hexaammineruthenium(III)chloride, glutamate dehydrogenase, a-ketoglutarate, nicotinamide adenine dinucleotide, and sodium chloride were obtained from Millipore Sigma.

4.2.2. General instrumentation

Cary 50 (Varian) spectrophotometers were used to record the UV/vis spectral data. Two of these spectrophotometers are housed in gloveboxes. The gloveboxes (MBraun and Innovative Technologies) were used to maintain anaerobic conditions while recording UV/vis spectra or

doing controlled potential electrolysis. The gloveboxes are filled with high purity nitrogen (Airgas, 99.99 % pure), which is continually circulated through an oxygen scrubber to maintain an oxygen level of less than 2 ppm. The glovebox scrubbers were regenerated with 5% or 7% Hydrogen (Airgas) at least once a month, or whenever the oxygen level rose above 2 ppm. BASi Epsilon EC potentiostats were used to measure spectropotentiometric data and to reduce required reagents at the appropriate potentials. An Ag/AgCl electrode (BASi model RE-5B) was used as the reference, and routinely calibrated against the methyl viologen midpoint potential as described in Chapter 2. Concentrations of ccNiR stocks were obtained by fitting UV/Vis spectra with the ccNiR extinction coefficient spectrum independently obtained using the pyridine hemochromagen assay,³ as described in Chapter 2.

4.2.3. Calibration Curve

A 2.76 mM stock solution of NADH was prepared by dissolving 0.1000 g of NADH in 50 mL of 50 mM HEPES free acid pH=7.45 buffer (which will henceforth be referred to as the assay buffer). The solution was distributed into cryotubes in 1 mL aliquots and stored in a -80 °C freezer until needed to ensure the stability of NADH over time. A 19 mM solution of α -KG was produced by dissolving 0.0362 g into 10 mL of the assay buffer. This solution can be stored in a 4 °C refrigerator for up to one month. Stocks of glutamate dehydrogenase (GDH) were made by dissolving 0.0565 g of GDH in 10 mL of assay buffer in order to produce an enzyme concentration of approx. 100 unit/mL. Aliquots of 1 mL were transferred into Eppendorf tubes and then frozen in a -20 °C freezer until needed.

A stock of 20 mM $(\text{NH}_4)_2\text{SO}_4$ was prepared by dissolving 0.0264 g of solid in 10 mL assay buffer. 100 μL of 20 mM $(\text{NH}_4)_2\text{SO}_4$ solution were then transferred to a falcon tube and diluted to 10 mL with assay buffer to make a 200 mM solution. Ammonium standards with

concentrations of 2, 5, 10, 20, 40, and 80 μM were made from this solution. The 2 μM $(\text{NH}_4)_2\text{SO}_4$ standard was made by taking a 10 μL aliquot of the 200 μM $(\text{NH}_4)_2\text{SO}_4$ solution and diluting to 1 mL with 990 μL of assay buffer. The 5 μM $(\text{NH}_4)_2\text{SO}_4$ standard was made by taking a 25 μL aliquot of the 200 μM $(\text{NH}_4)_2\text{SO}_4$ solution and diluting to 1 mL with 975 μL of assay buffer. The 10 μM $(\text{NH}_4)_2\text{SO}_4$ standard was made by taking a 50 μL aliquot of the 200 μM $(\text{NH}_4)_2\text{SO}_4$ solution and diluting to 1 mL with 950 μL of assay buffer. The 20 μM $(\text{NH}_4)_2\text{SO}_4$ standard was made by taking a 100 μL aliquot of the 200 μM $(\text{NH}_4)_2\text{SO}_4$ solution and diluting to 1 mL with 900 μL of assay buffer. The 40 μM $(\text{NH}_4)_2\text{SO}_4$ standard is made by taking a 200 μL aliquot of the 200 μM $(\text{NH}_4)_2\text{SO}_4$ solution and diluting to 1 mL with 800 μL of assay buffer. The 80 μM $(\text{NH}_4)_2\text{SO}_4$ standard was made by taking a 400 μL aliquot of the 200 μM $(\text{NH}_4)_2\text{SO}_4$ solution and diluting to 1 mL with 600 μL of assay buffer.

Prior to running the ammonium assays, a spectrum of NADH was first obtained by adding a 30 μL aliquot of 2.76 mM NADH stock to 970 μL of assay buffer (final NADH concentration, 82.8 mM). Next, a blank was run to make sure there were no competing reactions occurring (for example, with adventitious ammonium present in one or more of the reagents). This was done by adding 30 μL of 2.76 mM NADH, 185 μL of 19 mM α -KG, and 685 μL of assay buffer to a cuvette, for a total of 900 μL of solution. The spectrometer was then put on a cycle mode for 15 minutes, with a spectrum being taken every 15 seconds. Data collection was started, then after the first spectrum was obtained, 100 μL of GDH was added to the cuvette and the solution mixed with a stir stick before the spectrometer recorded the second spectrum. The GDH addition brings the volume up to a total of 1 mL, which is important when calculating the NH_4^+ concentration. Each standard was obtained using the same procedure except that instead of 685 μL of buffer, 500 μL of an NH_4^+ standard and 185 μL of assay buffer were added, along

with 30 μL of NADH and 185 μL of $\alpha\text{-KG}$. Once again, data collection was then started with 900 μL of reaction mixture in the cuvette, then 100 μL of GDH stock were added before the spectrometer recorded the second spectrum.

The concentration of $[\text{NH}_4^+]$ can be calculated using a rearrangement and variation of the Beer's law equation described in the equation below.

$$[\text{NH}_4^+] = \frac{A_0(0.9) - A_\infty}{6300 \text{ M}^{-1}\text{cm}^{-1}}$$

A_0 describes the absorbance maximum at 340 nm after the initial spectrum, 0.9 is the dilution factor after the addition of GDH, A_∞ is the absorbance obtained after NADH oxidizes no further, and $6300 \text{ M}^{-1}\text{cm}^{-1}$ is the extinction coefficient of NADH at 340 nm. Figure 4.1 shows the A_{340} vs time trace fit to the exponential function $A = A_0(0.9)e^{-kt} + A_\infty$ that can be used to accurately obtain the parameters A_0 and A_∞ . The concentration of GDH was adjusted to make the half-life of the reaction roughly 100s, which made it easy to obtain A_0 and A_∞ accurately. Figure 4.2 shows how the complete spectra change over time in one of the standard assay runs. As will be discussed in Section 4.2.7, fitting the set of time-resolved spectra instead of absorbance changes at a single wavelength is advantageous when analyzing complex reaction mixtures, such as one shown in Fig 4.3.

4.2.4. Electrolytic preparation of reducing agents

I3S, I4S, and hexaammineruthenium, were prepared and reduced by bulk electrolysis in much the same way as described for I3S in Section 3.2.3, or methyl viologen in Section 2.2.6. Specific details are as follows.

4.2.4.1. I3S_{red} preparation. Stock solutions containing 5 mM I3S and 200 mM NaCl were prepared in 50 mM assay buffer as described in Section 3.2.3. To make I3S solutions containing approximately 50% I3S_{red}, (“partially reduced, I3S_{PR}”) the stock was

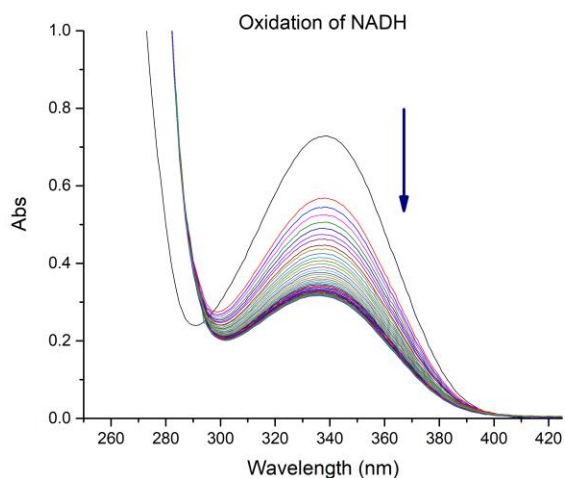


Figure 4.2. NADH spectral changes observed over the course of 15 minutes for the 40 μ M ammonium standard.

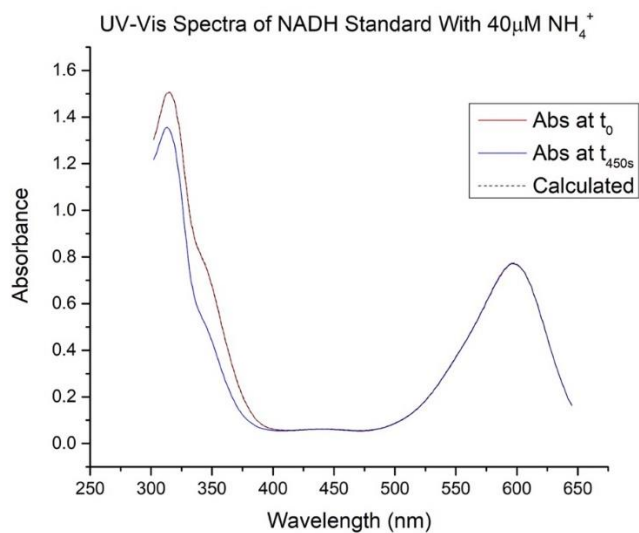


Figure 4.3. Spectral changes observed at $t = 0$ (red) and $t = 450$ s (blue) for a solution containing 40 μ M ammonium standard solution and also oxidized I3S. Changes in the 340 nm range correspond to the decrease in absorbance as NADH is consumed, but for complex mixtures such as this one, it is advisable to fit the entire spectrum as described in section 4.2.7, rather than a single wavelength, as in Fig. 4.1.

electrochemically reduced at an applied potential of -90 mV vs SHE. To make I3S solutions containing close to 100% I3S_{red}, (“fully reduced, I3S_{FR}”), the stock was electrochemically reduced at an applied potential of -290 mV vs SHE. I3S_{PR} solutions were turquoise green, while I3S_{FR} solutions were bright yellow. Spectra were routinely taken of the reduced I3S solutions to monitor reoxidation. The I3S does not stay reduced for more than a week, therefore, it must be used quickly after reduction.

4.2.4.2. I4S_{red} preparation. To prepare I4S stocks, 0.014 g of oxidized I4S and 0.046 g of NaCl were added into a clean, glass vial and dissolved in 4 mL of 50 mM assay buffer. As with the I3S and MV stocks, the buffer was added in the glovebox. The solution thus prepared contained 5 mM I4S and 200 mM NaCl in 50 mM HEPES pH 7.0. To make I4S solutions containing close to 100% I4S_{red}, (“fully reduced, I4S_{FR}”), the stock was electrochemically reduced at an applied potential of -230 mV vs SHE. I4S_{FR} solutions were bright yellow.

4.2.4.3. Hexaammineruthenium(II) (Ru^{II})preparation. To prepare hexaammineruthenium(III) (Ru^{III}) stocks, 0.0124 g of hexaammineruthenium(III) chloride and 0.046 g of NaCl were added to a clean, glass vial and dissolved in 4 mL of 50 mM assay buffer. As with the I3S and MV stocks, the buffer was added in the glovebox. The solution thus prepared contained 10 mM Ru^{III} and 200 mM NaCl in 50 mM HEPES pH 7.0 buffer. To reduce the Ru^{III}, the stock was electrochemically reduced at an applied potential of -100 mV vs SHE, which is 150 mV below Ru^{III}'s midpoint potential (+50 mV vs SHE). Hexaammineruthenium is virtually colorless in either oxidation state, though Ru^{II} is a faint yellow. However, a useful way to monitor the extent of Ru reduction is to add a small amount (10-20 mM) I4S to the solution before reduction. Oxidized I4S absorbs strongly in the 600 nm range, while reduced I4S does not. Because I4S has a midpoint potential of -46 mV vs SHE,⁴ when the absorbance at 600 nm

drops to 50% of the initial value, the ruthenium in solution can be considered reduced. During electrolysis, a spectrum was taken after every third 5-minute electrolysis burst to check the 600 nm absorbance. The solution appeared to be fully reduced after 10 bursts. Note that Ru^{II} degrades over the course of a day, probably due to substitution of the ammine ligands by water. Therefore, fresh solutions must be prepared daily. Another possibility is to freeze the sample in aliquots at -40 °C to use at a later date, though this approach has had variable success.

4.2.5. CcNiR-mediated reduction of nitrite in the presence of the various reducing agents

Nitrite was allowed to react under a variety of reducing conditions, in the presence of ccNiR, after which the reaction mixture was assayed to determine how much, if any ammonium was generated. For all experiments, ccNiR was added from a 60 mM stock solution and nitrite from a 100 mM stock, prepared as described in Section 2.2.6. All reactions were carried out in an anaerobic glovebox as described next for each individual reducing agent.

4.2.5.1. The ccNiR-mediated reduction of nitrite by I3S_{FR}. A 2 mM I3S_{FR} solution was prepared by combining 1.6 mL of the 5 mM stock (section 4.2.4.1) with 2.4 mL of assay buffer. Six reaction mixtures with varying I3S_{FR} concentrations were made in Eppendorf tubes by combining 2 mM I3S_{FR} solution, ccNiR stock, nitrite stock, and assay buffer, in the volumes shown in Table 4.1. It is important to note that the I3S_{FR} solution was the last reagent to be added to the reaction mixtures. After the last addition, each tube was capped, its contents mixed thoroughly and then left to react in the glovebox for 30 minutes. These experiments were done in triplicate. Reaction progress can be visually observed due to the color change of I3S from yellow to blue. Alternatively, the reaction mixture can be transferred to a cuvette, where reaction progress can be more quantitatively monitored by UV/Vis spectroscopy.

<i>Stock solution volumes (mL)</i>				$[I3S_{FR}]_{rxn}$
$I3S_{FR}$	<i>ccNiR</i>	NO_2^-	<i>Assay buffer</i>	(mM)
45	25	5	925	90
60	25	5	910	120
75	25	5	895	150
90	25	5	880	190
105	25	5	865	210
120	25	5	850	240

Table 4.1. Volumes of each stock solution used to make reaction mixtures with varying concentrations of $I3S_{FR}$. The concentrations of *ccNiR* and nitrite are constant at 1.5 mM and 500 mM, respectively, in all reaction mixtures. The total volume of each reaction mixture was 1.0 mL.

4.2.5.2. The *ccNiR*-mediated reduction of nitrite in the presence of $I3S_{PR}$. A reaction mixture with a concentration of 240 μ M $I3S_{PR}$ was produced by combining 48 μ L of 5 mM $I3S_{PR}$ stock, 5 μ L of 100mM $NaNO_2$ stock, 25 μ L of 60uM *ccNiR* stock, and 922 μ L of assay buffer, in an Eppendorf tube. This experiment was replicated six times.

4.2.5.3. The *ccNiR*-mediated reduction of nitrite in the presence of $I4S_{FR}$. A 2 mM $I4S_{FR}$ solution was prepared by combining 1.6 mL of the 5 mM stock (section 4.2.4.2) with 2.4 mL of assay buffer. Six reaction mixtures containing $I4S_{FR}$ concentrations varying from 90 mM – 240 mM were prepared as described for $I3S_{FR}$ in section 4.2.5.1 above, using the same stock solution volumes as shown in Table 4.1. The reaction mixtures were monitored for 1 hour in the glovebox before applying the ammonium assay as described below. These experiments were done in triplicate. UV/Visible monitoring of the reaction mixtures showed that the reactions appeared to be completed within ~20 minutes.

4.2.5.4. The ccNiR-mediated reduction of nitrite in the presence of Ru^{II}. A 2 mM Ru^{II} solution was prepared by combining 0.8 mL of the 10 mM stock (section 4.2.4.3) with 3.2 mL of assay buffer. Five reaction mixtures with varying Ru^{II} concentrations were made in Eppendorf tubes by combining 2 mM Ru^{II} solution, ccNiR stock, nitrite stock, and assay buffer, in the volumes shown in Table 4.2. As with the other reaction mixtures described above, the Ru^{II} reductant was the last reagent to be added to the reaction mixtures. After the last addition, each tube was capped, its contents mixed thoroughly and then left to react in the glovebox for 60 minutes. These experiments were done in triplicate. Unlike I3S and I4S, neither oxidation state of hexaammineruthenium has significant absorbance in the UV/Vis spectrum, so neither visual inspection or UV/Vis spectroscopy could be used to monitor Ru^{II} oxidation. On the other hand, the lack of absorbance from the reducing agent made it easy to observe spectral changes due to changes in ccNiR oxidation state. No spectral changes due to ccNiR were observed after 45-60 minutes.

<i>Stock solution volumes (mL)</i>				$[Ru^{II}]_{rxn}$
Ru^{II}	<i>ccNiR</i>	NO_2^-	<i>Assay buffer</i>	(mM)
10	25	5	960	20
20	25	5	950	40
40	25	5	930	80
60	25	5	910	120
80	25	5	890	160

Table 4.2. Volumes of each stock solution used to make reaction mixtures with varying concentrations of Ru^{II}. The concentrations of ccNiR and nitrite are constant at 1.5 mM and 500 mM, respectively, in all reaction mixtures. The total volume of each reaction mixture was 1.0 mL.

4.2.6. Ammonium assay for reaction products obtained under weakly reducing conditions

The ammonium assay was completed outside of the glovebox, since at this point the nitrite reduction reaction should have consumed all available reductant, thus there was no longer a sensitivity to oxygen. During the purification of ccNiR, ammonium sulfate was used in two purification steps. Although multiple buffer exchanges were done after purification, there could be residual ammonium salt. For this reason, a blank of ccNiR without reducing agent or nitrite was run initially to calculate ammonium already present in solution. This was done by first diluting the ccNiR to $\sim 1 \mu\text{M}$ by transferring $25 \mu\text{L}$ of $60 \mu\text{M}$ ccNiR stock to $975 \mu\text{L}$ of assay buffer. Then, $500 \mu\text{L}$ of the $1 \mu\text{M}$ ccNiR solution were added to an Eppendorf tube, along with $185 \mu\text{L}$ of assay buffer, $30 \mu\text{L}$ of 2.76 mM NADH, and $185 \mu\text{L}$ of 19 mM α -KG. This solution was then put into a quartz cuvette with a pathlength of 1 cm . The spectrometer was then put in cycle mode for 15 minutes , with a spectrum being taken every 15 seconds . Data collection was started, then after the first spectrum was obtained, $100 \mu\text{L}$ of GDH was added to the cuvette and the solution mixed with a stir stick before the spectrometer recorded the second spectrum. The GDH addition brings the volume up to a total of 1 mL , which is important when calculating the NH_4^+ concentration. To test the reaction mixtures produced in Section 4.2.5, a $500 \mu\text{L}$ aliquot of each mixture was added to an Eppendorf tube, along with $185 \mu\text{L}$ of assay buffer, $30 \mu\text{L}$ of 2.76 mM NADH, and $185 \mu\text{L}$ of 19 mM α -KG. These solutions were then transferred to a quartz cuvette with a pathlength of 1 cm . The spectrometer was put in cycle mode for 15 minutes , with a spectrum being taken every 15 seconds . Data collection was started, then after the first spectrum was obtained, $100 \mu\text{L}$ of GDH was added to the cuvette and the solution mixed with a

stir stick before the spectrometer recorded the second spectrum. The data collected for the sample assays and blank were analyzed as described in the following section.

4.2.7. Analysis of the assay results

Upon completing the assays of Section 4.2.6, the datafiles are saved as CSV files. To analyze each data set, six Mathcad programs are used sequentially. The first program is called “Step 1 submatrix former.” The CSV file containing the data is uploaded into this program, which will display the first absorbance vs wavelength (in nm) spectrum in the time series. The program has sliders that allow the user to trim from the spectrum any noisy or off-scale data; all other spectra in the time series will be similarly trimmed. In the ammonia assays that use I3S_{red} or I4S_{red} as the electron source, the spectral regions above ~570 nm and below 335 nm are often off scale and trimmed off using the adjustable sliders within the program. The program then generates a new data set lacking the unwanted spectral regions and exports it with the file name “truncated data set.csv”. The truncated data set CSV will automatically open in the next program.

Next, the second program called “Step 2 data extractor” takes the data exported by the first program, and upon being supplied by the user with the time interval between spectra (typically 15s), it reformats the data into a matrix that contains times in the first column, wavelengths in the first row, and absorbances in every other cell of the array (the cell at the intersection of the first row and first column is left as zero). The program also has a slider with output “index2” that allows the user to trim off unwanted spectra from the start of the time series. In assay experiments, set index = 1 to remove the first spectrum, which is collected before GDH has been added. The matrix prepared by the program is exported as a file named “reformatted data.csv”, to be used by the third program.

The third program, called “Step 3 SVD-wavelength in rows” is opened next. This program inputs the reformatted data and first separates the data into three distinct matrices: a matrix of wavelengths (extracted from the first row of “reformatted data.csv”), one of times (extracted from the first column of “reformatted data.csv”), and one of absorbances, obtained from the corresponding cells of “reformatted data.csv”. The program then performs singular value decomposition (SVD) on the absorbance matrix.⁵ A slider with output variable “components” allows the user to plot each column of the SVD U matrix vs wavelength, and each column of the SVD V matrix vs time. For the ammonia assays, the first two columns of the U and V matrices will typically have signal, while the remaining ones will look like noise, showing that only two components are contributing to all the time-resolved spectra. If the “components” slider is set to 1, the program reconstructs a “clean” absorbance matrix using only the first two columns of U and V, together with the first two singular values from the S matrix (in Mathcad, the first row and column of an array have a zero index).⁵ The step 3 program exports three separate csv files, one containing the wavelengths, one the times, and the third the absorbance matrix reconstructed using only the non-noise columns of the U and V matrix, and the corresponding singular values.⁵

The fourth Mathcad program, referred to as “step 4 rel Evalue extractor 1Exp”, fits the SVD-processed absorbance data generated by the previous program to the equation shown in Scheme 4.2. In the scheme, $A_{\lambda,t}$ is the absorbance obtained at wavelength λ and time t , \mathbf{S}_0 is a spectral component present at $t = 0$, and \mathbf{S}_1 is a component that decays exponentially at a rate governed by k . A slider allows the user to manually adjust the value of k , with which the program calculates the best values of \mathbf{S}_0 , \mathbf{S}_1 , and k by a combination of linear and non-linear least-squares fitting.² The value for k should be manually adjusted until the resulting sum of squares value

$$A_{\lambda,t} = S_{0(\lambda)} + S_{1(\lambda)} \exp(-kt)$$

Scheme 4.2. Equation used to fit the spectral changes associated with NADH oxidation in the presence of other absorbing species such as ccNiR and I3S or I4S.

reaches a minimum, indicating an optimal fit between the experimental and calculated spectra. Once a good fit is achieved, the program exports a file called “Rel ext coeffs.csv” that contains **S₀** and **S₁** as columns in an array.

The last two programs, “Step 5 E1 fit auto” and “Step 6 E2 fit auto”, each fit one of the spectral components **S₀** or **S₁** using independently known extinction coefficient spectra. Three species were found to contribute to **S₀** in proportion to their concentrations at $t = 0$: ccNiR, I3S_{ox} or I4S_{ox}, (but not Ru^{III}), and NADH. For most of the experiments, the extinction coefficient spectrum of ccNiR_{WT} was used; however, this could be replaced by the spectra of the ccNiR_{R103Q}, or ccNiR_{Y206F} variants when necessary (see Section 4.3.3 below). The most important role of the **S₀** fit was to obtain the concentration of I3S or I4S present in solution because these values are necessary for calculating the percent of formation of ammonium relative to the theoretical maximum (see Section 4.3.3).

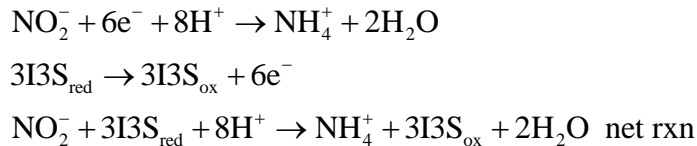
Importantly, only the amount of NADH that oxidized during the GDH-catalyzed amination of a-KG contributed to **S₁**, so this component was fit with the extinction coefficient spectrum of NADH only. In this way, the amount of NADH oxidized, and the corresponding amount of ammonium present in solution at $t=0$, could be obtained very accurately, even in the presence of other strongly absorbing species. Such a feat would be much less certain if only the absorbance differences at 340 nm and the equation from Section 4.2.3 were used. To account for

the fact that trace amounts of adventitious ammonium left over from ccNiR purification were almost always present in the reaction mixture, the program that fit S_1 was modified to automatically subtract the concentration of adventitious ammonium present, which in turn was obtained from the blank assay mixture that contained ccNiR but no added nitrite or reducing agent (Section 4.2.6). The amount of adventitious ammonium is specified by the user by adjusting the parameter $NADH_0$. Then, the program calculates the ammonium formed by ccNiR-catalyzed reduction of nitrite as the difference between the amount calculated from fitting S_1 and $NADH_0$. The corrected ammonium concentration is specified by the parameter $NADH_1$.

4.3. Results

4.3.1. I3S_{PR} as electron source

I3S_{PR} was chosen as the first reductant to test because a 1:1 mix of I3S_{red} and I3S_{ox} poises the reaction mixture's potential at -90 mV vs SHE, which is the potential at which a slight current due to catalytic nitrite reduction is first detected in protein voltammetry experiments.⁶ Would ammonium be formed under these conditions? And if so, how much? To answer this question, an experiment was conducted to see how much ammonium would be generated in the presence of 120 μ M I3S_{red}, 120 μ M I3S_{ox}, 500 mM nitrite, and 1.5 mM ccNiR. Three equivalents of I3S_{red} are required to reduce one equivalent of nitrite to ammonium (Scheme 4.3), so 120 μ M of I3S_{red} is enough to produce a maximum of 40 mM ammonium. For the ammonia assay, the reaction mixture is diluted by half when the assay reagents a-KG, NADH, and GDH are added (Section 4.2.6), so a maximum of 20 mM ammonium could be present in the assay mixture if all the available I3S_{red} reacted with nitrite to produce ammonium. The Fig. 4.4 calibration curve shows that the ammonium assay has a range of detection from 2 μ M to 80 μ M ammonium, so 20 mM should be readily detectable.



Scheme 4.3. Stoichiometry for the reaction of I3S with nitrite to produce ammonium. I4S would have the same stoichiometry, whereas Ru^{II} is a 1-electron donor, so 6 equivalents are required to reduce nitrite to ammonium.

Table 4.3 summarizes the results from 6 replicates of the experiment described in the previous paragraph. The second column of the table lists the I3S_{red} concentrations obtained experimentally by fitting the S₀ spectral component of Scheme 4.2 with the extinction coefficient spectra of I3S_{ox}, NADH, and ccNiR_{ox}. (Section 4.2.7). Note that the analysis of S₀ tells only how much I3S_{ox} is present at the time that the assay is initiated. To obtain the I3S_{red} values listed in

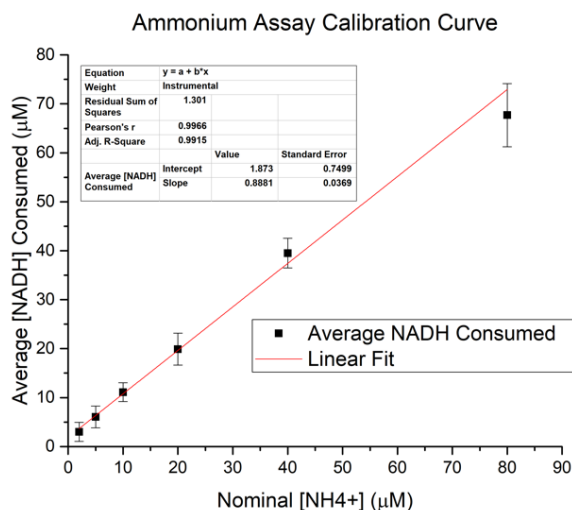


Figure 4.4. The calibration curve produced from measuring the change in NADH concentration over time for standards ranging from 2-80µM ammonium. The linear fit is shown in red.

<i>I3S_{Red}</i> Nominal (μM)	<i>I3S_{Red}</i> Calculated (μM)	$[\text{NH}_4^+]$ Expected (μM)	$[\text{NH}_4^+]$ Calculated (μM)	Percent NH_4^+ Formation
60.0	67.85	22.62	20.76	91.79
60.0	63.90	21.30	20.77	97.51
60.0	71.00	23.67	21.79	92.07
60.0	68.30	22.77	20.61	90.53
60.0	69.65	23.22	23.51	101.26
60.0	69.95	23.32	23.83	102.20

Table 4.3. Replicated experiments of the ccNiR-catalyzed reduction of nitrite in the presence of partially reduced Indigo trisulfonate.

the second column of Table 4.3, it was assumed that exactly 50% of the total I3S was reduced when I3S, nitrite, and ccNiR were first mixed. Based on the values listed in column 2, column 3 of Table 4.3 lists the ammonium concentrations expected if all the electrons from I3S_{red} go towards generating ammonium. From the stoichiometry of Scheme 4.3, these would be one third of the column 2 I3S_{red} concentrations. Column 4 of the table then lists the ammonium concentrations obtained by fitting the S_1 spectral component with the NADH extinction coefficient spectrum (Scheme 4.2, Section 4.2.7). This reflects the actual ammonium present in the assay mixture. Finally, the last column in the table lists the percent ammonium formation, calculated as follows:

$$\text{Percent } \text{NH}_4^+ \text{ Formation (\%)} = \frac{[\text{NH}_4^+]_{\text{Calculated}}}{[\text{NH}_4^+]_{\text{Expected}}} \times 100$$

As can be seen from the table, the average percent formation of ammonium was $96 \pm 5\%$; that is, all, or virtually all the electrons from I3S_{red} went towards reducing nitrite to ammonium.

4.3.2. I3S_{FR} as an electron source

The ammonium assay was completed for five replicate sets of data obtained from ccNiR-catalyzed reactions of nitrite with varying concentrations of I3S_{FR}. Table 4.4 lists the ammonium concentrations calculated by fitting each of the **S**₁ spectral components with the NADH extinction coefficient spectrum (Scheme 4.2, Section 4.2.7). Table 4.5 then calculates the percent ammonium formation observed for each I3S_{red} concentration of the first data set from Table 4.4, using the procedure described for I3S_{PR} in Section 4.3.1; the other four data sets gave similar results. The average percentage of ammonium formation was found to be 78±8%, which is lower than was observed for I3S_{PR} in Section 4.3.1. However, this is most likely because I3S_{FR} solutions did not in fact contain 100% reduced I3S (remember that fitting the **S**₀ spectral component reveals only the amount of I3S_{ox} present after the reaction is over, not how much I3S_{red} was present at the reaction's start).

<i>I3S_{red} Nominal (μM)</i>	<i>[NH₄⁺] Calculated (μM)</i>	<i>[NH₄⁺] Calculated (μM)</i>	<i>[NH₄⁺] Calculated (μM)</i>	<i>[NH₄⁺] Calculated (μM)</i>	<i>[NH₄⁺] Calculated (μM)</i>
	<i>Dataset 1</i>	<i>Dataset 2</i>	<i>Dataset 3</i>	<i>Dataset 4</i>	<i>Dataset 5</i>
45.0	9.75	13.36	11.42	13.65	9.52
60.0	12.8	16.66	13.8	15.46	11.42
75.0	15.3	20.61	16.69	17.85	19.91
90.0	17.6	25.29	18.1	19.38	15.97
105.0	26.9	27.78	19.96	24.43	23.56
120.0	25.0	29.21	20.38	24.85	-

Table 4.4. The calculated ammonium formation for the ccNiR-catalyzed reduction of nitrite in the presence of fully reduced indigo trisulfonate at concentrations ranging from 45-120 μM . The experiments were reproduced five times.

<i>I3S_{Red}</i> Nominal (μM)	<i>I3S_{Red}</i> Calculated (μM)	$[\text{NH}_4^+]$ Expected (μM)	$[\text{NH}_4^+]$ Calculated (μM)	Percent NH_4^+ Formation
45.0	35.5	11.8	9.75	82.4
60.0	48.8	16.3	12.8	78.7
75.0	62.8	20.9	15.3	73.1
90.0	75.2	25.1	17.6	70.2
105.0	88.6	29.5	26.9	91.1
120.0	102.0	34.0	25.0	73.5

Table 4.5. The calculated percent ammonium formation for the ccNiR-catalyzed reduction of nitrite in the presence of fully reduced indigo trisulfonate at concentrations ranging from 45-120 μM for Dataset 1 from Table 4.4.

4.3.3. $I3S_{FR}$ reduction of nitrite in the presence of the ccNiR variants R103Q and Y206F

In addition to measuring how much ammonium was generated when nitrite and $I3S_{FR}$ were mixed in the presence of ccNiR_{WT}, the assay was also used to assess how much ammonium formed when the reagents were combined in the presence of the variants ccNiR_{R103Q} and ccNiR_{Y206F}. Table 4.6 and Table 4.7 show the results obtained with the R103Q variant, while Table 4.8 and Table 4.9 list those obtained with the Y206F variant. In both cases, the amount of ammonium formed was well below the maximum amount possible, $14 \pm 2\%$ for ccNiR_{R103Q}, and $20 \pm 4\%$ for ccNiR_{Y206F}. Furthermore, the Table 4.7 data reveal a possible decrease in the percent ammonium formed as the reductant concentration increases, though a more thorough analysis will be needed to determine if this trend is statistically significant.

<i>I3S_{red}</i> Nominal (μM)	$[\text{NH}_4^+]$ Calculated (μM)	$[\text{NH}_4^+]$ Calculated (μM)	$[\text{NH}_4^+]$ Calculated (μM)
	<i>Dataset A</i>	<i>Dataset B</i>	<i>Dataset c</i>
45.0	2.64	-8.43	1.93
60.0	3.37	4.37	3.00
75.0	3.81	3.28	3.54
90.0	4.55	4.74	3.39
105.0	4.84	4.87	5.72
120.0	5.63	4.84	4.67

Table 4.6. The calculated ammonium formation for the R103Q ccNiR variant -catalyzed reduction of nitrite in the presence of fully reduced Indigo trisulfonate at concentrations ranging from 45-120 μM . The experiments were reproduced in triplicate.

<i>I3S</i> Nominal (μM)	<i>I3S</i> Calculated (μM)	$[\text{NH}_4^+]$ Expected (μM)	$[\text{NH}_4^+]$ Calculated (μM)	Percent NH_4^+ Formation
45.0	48.47	16.16	2.64	16.34
60.0	65.83	21.94	3.37	15.36
75.0	86.24	28.75	3.81	13.25
90.0	106.3	35.43	4.55	12.84
105.0	120.2	40.07	4.84	12.08
120.0	141.7	47.23	5.63	11.92

Table 4.7. The calculated percent ammonium formation for the R103Q ccNiR variant -catalyzed reduction of nitrite in the presence of fully reduced Indigo trisulfonate at concentrations ranging from 45-120 μM for Dataset A from Table 4.6.

<i>I3S_{red}</i> Nominal (μM)	$[\text{NH}_4^+]$ Calculated (μM)	$[\text{NH}_4^+]$ Calculated (μM)	$[\text{NH}_4^+]$ Calculated (μM)
	Dataset A	Dataset B	Dataset c
45.0	2.31	3.17	2.51
60.0	5.75	1.29	3.06
75.0	4.36	1.45	4.03
90.0	6.431	2.59	5.77
105.0	7.6	N/A	6.13
120.0	8.94	2.52	N/A

Table 4.8. The calculated ammonium formation for the Y206F ccNiR mutant-catalyzed reduction of nitrite in the presence of fully reduced Indigo trisulfonate at concentrations ranging from 45-120 μM . The experiments were reproduced in triplicate.

<i>I3S</i> Nominal (μM)	<i>I3S</i> Calculated (μM)	$[\text{NH}_4^+]$ Expected (μM)	$[\text{NH}_4^+]$ Calculated (μM)	Percent NH_4^+ Formation
45.0	47.43	15.81	2.31	14.61
60.0	63.24	21.08	5.75	27.28
75.0	80.62	26.87	4.36	16.22
90.0	99.23	33.08	6.43	19.44
105.0	113.5	37.83	7.60	20.09
120.0	130.9	43.63	8.94	20.49

Table 4.9. The calculated percent ammonium formation for the Y206F ccNiR mutant-catalyzed reduction of nitrite in the presence of fully reduced Indigo trisulfonate at concentrations ranging from 45-120 μM for Dataset A from Table 4.6.

4.3.4. I4S_{FR} as an electron source

The analysis for the ccNiR-catalyzed reduction of nitrite in the presence of fully reduced I4S was completed in the same manner used to analyze the I3S data, the only difference being that, when fitting the S_0 spectral component, the extinction coefficient spectrum of fully oxidized I4S was used in place of the I3S one. The reaction was completed in triplicate with varying concentrations of I4S. The calculated ammonium formations are listed in Table 4.10. Table 4.11 then calculates the percent ammonium formation observed for each I4S_{red} concentration of the first data set from Table 4.10, using the procedure described for I3S_{PR} in Section 4.3.1. The other two data sets from Table 4.10 gave similar results. Interestingly, the ccNiR-catalyzed reduction of nitrite in the presence of I4S as a reducing agent resulted in an average of only $49 \pm 3\%$ ammonium formation.

<i>I4S_{red} Nominal (μM)</i>	<i>[NH₄⁺] Calculated (μM)</i>	<i>[NH₄⁺] Calculated (μM)</i>	<i>[NH₄⁺] Calculated (μM)</i>
	<i>Dataset 1</i>	<i>Dataset 2</i>	<i>Dataset 3</i>
45.0	5.03	6.66	7.99
60.0	10.16	10.35	8.76
75.0	11.57	13.49	12.35
90.0	15.64	15.17	15.25
105.0	15.91	16.76	17.35
120.0	17.24	18.33	17.52

Table 4.10. The calculated ammonium formation for the ccNiR-catalyzed reduction of nitrite in the presence of fully reduced indigo tetrasulfonate at concentrations ranging from 45-120 μM . The experiments were reproduced in triplicate.

<i>I4S_{Red}</i> Nominal (μM)	<i>I4S_{Red}</i> Calculated (μM)	$[\text{NH}_4^+]$ Expected (μM)	$[\text{NH}_4^+]$ Calculated (μM)	Percent NH_4^+ Formation
45.0	43.54	14.51	6.66	45.89
60.0	61.37	20.46	10.35	50.59
75.0	76.44	25.48	13.49	52.94
90.0	89.38	29.79	15.17	50.92
105.0	106.7	35.57	16.76	47.12
120.0	125.2	41.73	18.33	43.92

Table 4.11. The calculated percent ammonium formation for the ccNiR-catalyzed reduction of nitrite in the presence of fully reduced indigo tetrasulfonate at concentrations ranging from 45-120 μM for Dataset 2 from Table 4.10.

4.3.5. Ru^{II} as an electron source

The ccNiR-catalyzed reduction of nitrite mediated by hexaammineruthenium(II) yielded a complicated, yet interesting result. Ru^{II} is different than I3S and I4S in that it does not have significant absorbance at the concentrations used in the experiments. Therefore, when fitting S_0 from Scheme 4.2 as described in Section 4.2.7, only the NADH and ccNiR extinction coefficient spectra were used in the fits, and the total hexaammineruthenium concentration couldn't be independently verified. Furthermore, data analysis is complicated by the fact that Ru^{II} (and Ru^{III}) has six ammonia ligands, and though the complex is relatively stable, it does undergo slow substitution of the ammonia ligands by water, which releases free ammonium. To correct for this interference, control ammonium assays were completed with only Ru^{II} in solution, omitting ccNiR and nitrite. Three sets of control reaction mixtures were analyzed. Each set consisted of 5

experiments in which the Ru^{II} concentrations varied from 10-80 μ M in the same way as they did in the reaction mixtures containing ccNiR and nitrite (Table 4.12). The three control datasets differed from each other in the amount of time that they were allowed to incubate in the glovebox before being subjected to the ammonium assay: 30 minutes, 60 minutes, and 2 hours, respectively. The amount of ammonium detected by the assay was found to plateau within a 60-minute period, possibly implying that an equilibrium was reached between free and Ru-bound ammonium.

For the analysis of the actual datasets, the amount of ammonium produced in the blank dataset was averaged for each concentration and was subtracted from the total amount of ammonium calculated by the **S**₁ component fit (Section 4.2.7). As mentioned in Section 4.2.7, the amount of adventitious ammonium contributed by the ccNiR stock solution was also subtracted at this point. The net amounts of ammonium calculated to come from the reaction of nitrite with Ru^{II}, rather than from other sources, are listed in Table 4.12. Note that these are uniformly negative, which shows that the amount of adventitious ammonium calculated from the control measurements overestimated the amount truly present in the reaction mixtures. Similar results were obtained when Ru^{II} was allowed to react with nitrite in the presence of the ccNiR variants R103Q and Y206F (Table 4.13 and Table 4.14). Though these experiments will need to be repeated with better quantification of adventitious ammonium, the fact that the ammonium concentration measured in all the experiments from Tables 4.12 – 4.14 remained constant as the Ru^{II} concentration increased suggests that little or no ammonium is generated when Ru^{II} is the electron source.

<i>HexRu_{red}</i> <i>Nominal (μM)</i>	<i>[NH₄⁺]</i> <i>Expected (μM)</i>	<i>[NH₄⁺]</i> <i>Calculated</i> <i>(μM)</i>	<i>[NH₄⁺]</i> <i>Calculated</i> <i>(μM)</i>	<i>[NH₄⁺]</i> <i>Calculated</i> <i>(μM)</i>	<i>Average</i> <i>[NH₄⁺]</i> <i>(μM)</i>
		<i>Dataset 1</i>	<i>Dataset 2</i>	<i>Dataset 3</i>	
10.0	1.67	-9.89	-9.56	-8.89	-9.45
20.0	3.33	-8.85	-8.51	-8.16	-8.51
40.0	6.67	-4.14	-7.4	-4.21	-5.25
60.0	10.0	-12.60	-8.77	-7.29	-9.55
80.0	13.33	-14.12	-11.65	-4.86	-10.21

Table 4.12. The calculated ammonium formation for the ccNiR-catalyzed reduction of nitrite in the presence of fully reduced hexaammineruthenium at concentrations ranging from 10-80 μM.

The experiments were reproduced in triplicate.

<i>HexRu_{red}</i> <i>Nominal (μM)</i>	<i>[NH₄⁺]</i> <i>Expected (μM)</i>	<i>[NH₄⁺]</i> <i>Calculated</i> <i>(μM)</i>	<i>[NH₄⁺]</i> <i>Calculated</i> <i>(μM)</i>	<i>[NH₄⁺]</i> <i>Calculated</i> <i>(μM)</i>	<i>Average</i> <i>[NH₄⁺]</i> <i>(μM)</i>
		<i>Set 1</i>	<i>Set 2</i>	<i>Set 3</i>	
10.0	1.67	-9.86	-10.64	-11.93	-10.81
20.0	3.33	-9.14	-9.71	-10.94	-9.93
40.0	6.67	-8.56	-9.06	-11.38	-9.67
60.0	10.0	-11.40	-13.18	-13.88	-12.82
80.0	13.33	-11.13	-9.74	-9.56	-10.14

Table 4.13. The calculated ammonium formation for the ccNiR_{R103Q} variant-mediated reduction of nitrite in the presence of fully reduced hexaammineruthenium at concentrations ranging from

10-80 μM. The experiments were reproduced in triplicate.

$[HexRu_{red}]$ Nominal (μM)	$[NH_4^+]$ Expected (μM)	$[NH_4^+]$ Calculated (μM)	$[NH_4^+]$ Calculated (μM)	$[NH_4^+]$ Calculated (μM)	Average $[NH_4^+]$ (μM)
		Set 1	Set 2	Set 3	
10.0	1.67	-10.20	-10.57	-11.93	-10.90
20.0	3.33	-9.43	-9.56	-12.66	-10.55
40.0	6.67	-8.20	-10.20	-6.82	-8.41
60.0	10.0	-8.54	-20.73	-6.41	-11.89
80.0	13.33	-5.91	-2.56	-8.33	-5.60

Table 4.14. The calculated ammonium formation for the ccNiR_{Y206F} variant-mediated reduction of nitrite in the presence of fully reduced hexaammineruthenium at concentrations ranging from 10-80 μM . The experiments were reproduced in triplicate.

4.4. Discussion

4.4.1. I3S as an electron source

The results reported in sections 4.3.1 and 4.3.2 (Tables 4.3 – 4.5) suggest that ccNiR_{WT} catalyzes the reduction of nitrite by I3S_{red} to produce ammonium quantitatively and exclusively. For the experiments with I3S_{PR} (Section 4.3.1), the % ammonium formation was $96 \pm 5\%$, or essentially 100%. The experiments with I3S_{FR} (Section 4.3.2) appeared to show less conversion to ammonium ($78 \pm 8\%$), but this is probably an artifact because I3S was not truly fully reduced at the start of the reaction. It is more difficult to fully reduce I3S by bulk electrolysis than it is to reduce it by 50%, and it is also more difficult to store it at that level of reduction. From these results, we can conclude that I3S is a potent enough reductant to overcome the activation barrier of the putative rate limiting step in the ccNiR-catalyzed reduction of nitrite to ammonium (Fig. 1.7). This is an important result because I3S_{red} is a weaker reductant than MV_{red}, and yet it is still able to produce ammonium quantitatively at a detectable rate.

In contrast to the result obtained in the presence of ccNiR_{WT}, the amounts of ammonium produced when I3S_{FR} and nitrite were mixed in the presence of the ccNiR_{R103Q} and ccNiR_{Y206F} were minimal ($14\pm 2\%$ for ccNiR_{R103Q}, and $20\pm 4\%$ for ccNiR_{Y206F}; Tables 4.6 – 4.9). There are at least three possible explanations for this result. First, the low yields could be due to the variant-catalyzed reactions being much slower than those catalyzed by the wild type, so that not enough time was allowed for the reactions to go to completion. Second, it is possible that, during turnover, the variants are converted into inactive forms of the enzyme, so that catalysis stopped after a few catalytic cycles. There is some spectroscopic evidence for this mechanism,⁷ and the possibility is currently being investigated further. Finally, it is possible that nitrogenous species other than ammonium are generated when the ccNiR_{R103Q} and ccNiR_{Y206F} mediate nitrite reduction by I3S_{red}, even though ammonium is the sole product of the ccNiR_{WT} – catalyzed process. In the experiments with the variants, the extent of I3S_{red} re-oxidation that took place in the glovebox before the reaction mixtures were brought out for the assay was not monitored. Therefore, for now, it is unclear which of the possible mechanisms accounts for the low ammonium yields. Further experiments are planned to address this question soon.

4.4.2. I4S as an electron source

When I4S_{FR} was the electron source, the %yield of ammonium was only $49\pm 3\%$ of that expected if all the electrons available from I4S had gone to ammonium formation. Again, there could be several reasons for this, but one intriguing possibility is that as the ratio of I4S_{red}/I4S_{ox} decreases, the solution potential increases to a value too high to overcome the activation barrier of the putative rate limiting step in the ccNiR-catalyzed reduction of nitrite to ammonium (Fig. 1.7). The midpoint potential for I4S is -45 mV vs SHE, which is about 50 mV higher than the potential at which a slight current due to catalytic nitrite reduction is first detected in protein

voltammetry experiments.⁶ At high $I4S_{red}/I4S_{ox}$ ratios, the solution potential would be near -100 vs SHE. However, as the ratio decreased, the potential would increase, which might drastically slow the rate of catalysis. The fact that the % yield of ammonium remained the same as the total I4S concentration was varied from 45-120 μ M supports the hypothesis that it is the $I4S_{red}/I4S_{ox}$ ratio that determines reaction effectiveness. However, further experiments will be needed to confirm this hypothesis.

4.4.3. Ru^{II} as an electron source

As noted in Section 4.3.5, the amount of ammonium generated when Ru^{II} provided the electrons could not be reliably quantified because estimates of the amount of adventitious ammonium generated from hexaammineruthenium hydrolysis were unreliable (Tables 4.12-4.14). Though these experiments will need to be repeated with better quantification of adventitious ammonium, they suggest that little or no ammonium is generated when Ru^{II} is the electron source. This could be because Ru^{II} catalyzes reduction of nitrite to ammonium too slowly to generate detectable quantities during the time allowed for the reaction. In support of this possibility, the fit of the S_0 spectral component with the known extinction coefficient spectra of ccNiR_{ox} and NADH was poor in a way that suggests that ccNiR remained reduced outside the glovebox at the start time of the assay (the ccNiR Soret peak shifts from 409 nm to 424 nm as the enzyme reduces). This is what might be expected if significant Ru^{II} was still present at the start of the assay because it hadn't been consumed in reactions with nitrite. By contrast, fits of the S_0 spectral component when $I3S_{red}$ or $I4S_{red}$ was the electron source were much better in the ccNiR Soret region. The midpoint potential for hexaammineruthenium is +50 mV vs SHE, which is ~90 mV higher than that of I4S.

4.5. Summary

In conclusion, with appropriate data processing, the Bergmeyer and Beutler assay was able to reliably quantify the ammonium generated in ccNiR-mediated reactions of nitrite with various reducing agents, even in the presence of interfering colored species. The results of the assay showed that ammonium is generated quantitatively when I3S is the electron source, irrespective of the I3S_{red}/I3S_{ox} ratio. On the other hand, the amount of ammonium produced when I4S_{red} is the electron source may depend on the I4S_{red}/I4S_{ox} ratio, while no ammonium appears to be produced when Ru^{II} is the electron source. Studies are now under way to confirm these results and to more accurately quantify how I4S_{red} re-oxidation correlates with ammonium formation. Lastly, even while ccNiR_{WT} can catalyze reduction of nitrite exclusively to ammonium when I3S_{red} is the electron source, the same is not true for the ccNiR_{R103Q} and ccNiR_{Y206F} variants. This is in line with previous studies by the Pacheco group, and the cause is now being further investigated.⁷

4.6 References

- (1) Ali, M. Probing the early steps in the catalytic reduction of nitrite to ammonia, catalyzed by cytochrome *c* nitrite reductase. University of Wisconsin-Milwaukee, Milwaukee, WI, 2019.
- (2) Shahid, S.; Ali, M.; Legaspi-Humiston, D.; Wilcoxon, J.; Pacheco, A. A. A kinetic investigation of the early steps in cytochrome *c* nitrite reductase (ccNiR)-catalyzed reduction of nitrite. *Biochemistry* **2021**, *60*, 2098-2115.
- (3) Berry, E. A.; Trumpower, B. L. Simultaneous determination of hemes a, b, and c from pyridine hemochrome spectra. *Anal. Biochem.* **1987**, *161*, 1-15. Barr, I.; Guo, F. Pyridine hemochromagen assay for determining the concentration of heme in purified protein solutions. *Bio. Protoc.* **2015**, *5*, (18).
- (4) Fultz, M. L.; Durst, R. A. Mediator compounds for the electrochemical study of biological redox systems: a compilation. *Anal. Chim. Acta* **1982**, *140*, 1-18.
- (5) Press, W. H.; Teukolsky, S. A.; Vetterling, W. T.; Flannery, B. P. Numerical Recipes the art of scientific computing. 3rd ed.; Cambridge University Press, 2007; pp 65-75. Henry, E. R.; Hofrichter, J. Singular Value Decomposition: Application to Analysis of Experimental Data. In *Meth. Enzymol.*, Brand, L., Johnson, M. L. Eds.; Vol. 210; Academic Press, 1992; pp 129-192.
- (6) Judd, E. T.; Youngblut, M.; Pacheco, A. A.; Elliott, S. J. Direct Electrochemistry of *Shewanella oneidensis* Cytochrome *c* Nitrite Reductase: Evidence of Interactions across the Dimeric Interface. *Biochemistry* **2012**, *51* (51), 10175-10185. Judd, E. T.; Stein, N.; Pacheco, A.

A.; Elliott, S. J. Hydrogen bonding networks tune proton-coupled redox steps during the enzymatic six-electron conversion of nitrite to ammonia. *Biochemistry* **2014**, *53*, 5638-5646.
(7) Alam, S. The Effects of an R103Q Mutation on the Chemical and Physical Properties of the Enzyme Cytochrome C Nitrite Reductase (ccNiR). University of Wisconsin - Milwaukee, 2022.

Chapter 5 The search for the four-electron reduced putative ccNiR intermediate using the stopped-flow technique

5.1. Overview

In recent years, the Pacheco group gathered evidence of an intermediate that accumulates at an applied potential between -80 mV vs SHE and -120 mV vs SHE. One piece of evidence was found in UV/vis spectropotentiometric and protein film voltammetry studies.^{1,2} Rapid-mixing experiments performed with hydroxylamine and ccNiR supported these results.³ When ccNiR was mixed with excess hydroxylamine at varying concentrations (10 mM-300 mM), UV/visible stopped-flow experiments showed reduction of ccNiR taking place as a triphasic exponential process. Rapid freeze-quench results gave EPR spectroscopic evidence that a radical species accumulates within 100 ms of mixing and then decays without reaching a concentration of zero. EPR analysis also indicated that the intermediate formed is most likely to be the [Fe_{H1}(H₂NO·)] moiety presented in computational studies shown in Step 4 and 5, Scheme 1.2.^{3,4} These studies indicate that within 10 s of mixing ccNiR and hydroxylamine, electrons are transferred from hydroxylamine to the ccNiR heme pool, generating an equilibrium mixture of partially reduced nitrosylated ccNiR putative intermediates.³ As mentioned in Chapter 1 and summarized in Fig. 1.7, 1- and 2-electron reduced intermediates can be detected when nitrite-loaded ccNiR is reduced by weak reductants such as ferrocyanide or TMPD.^{5,6} The results of Stein and Youngblut suggest that, in the presence of reducing agents more powerful than TMPD but weaker than MV_{red}, for example, I3S_{red}, 3- and 4-electron reduced intermediates might also be trappable.^{1,3} This chapter begins with stopped-flow studies of the ccNiR-catalyzed reduction of nitrite in the presence of strong reductant MV_{red}. Methyl viologen demystified the groundwork of the experiments and presented quite unexpected results. Further experiments were performed

with various weak reductants which included partially reduced Indigo trisulfonate (I3S_{PR}), fully reduced I3S (I3S_{red}), and fully reduced Indigo tetrasulfonate (I4S_{red}). The weak reductants were reduced to potentials between -90 mV vs SHE and -290 mV vs SHE, which is within the range that the second intermediate has been hypothesized to build up.¹⁻³

5.2. Materials and Methods

5.2.1. General materials

Sodium nitrite was purchased from Acros Organics; ammonium sulfate (AS), EDTA and HEPES free acid and sodium salt were obtained from fisher scientific; nitrogen gas (high purity grade) from Airgas. Wild type *S. oneidensis* ccNiR and variant ccNiRs were purified as described in Chapter 2. Potassium indigo tetrasulfonate, potassium indigo trisulfonate, hexaammineruthenium(III) chloride, Mmethyl viologen, and sodium chloride were received from Millipore Sigma.

5.2.2. General instrumentation

Cary 50 (Varian) spectrophotometers were used to record the UV/vis spectral data. Two of these spectrophotometers are housed in gloveboxes. The gloveboxes (MBraun and Innovative Technologies) were used to maintain anaerobic conditions while recording UV/vis spectra or doing controlled potential electrolysis. The gloveboxes are filled with high purity nitrogen (Airgas, 99.99 % pure), which is continually circulated through an oxygen scrubber to maintain an oxygen level of less than 2 ppm. The glovebox scrubbers were regenerated with 5% or 7% Hydrogen (Airgas) at least once a month, or whenever the oxygen level rose above 2 ppm. BASi Epsilon EC potentiostats were used to measure spectropotentiometric data and to reduce required reagents at the appropriate potentials. An Ag/AgCl electrode (BASi model RE-5B) was used as the reference, and routinely calibrated against the methyl viologen midpoint potential as

described in Chapter 2. Concentrations of ccNiR stocks were obtained by fitting UV/Vis spectra with the ccNiR extinction coefficient spectra of wild type and variants, independently obtained using the pyridine hemochromagen assay,⁷ as described in Chapter 2.

5.2.3. Preparation of reducing agents

5 mM solutions of partially and fully reduced I3S (I3S_{PR} and I3S_{red}) were prepared as described in Section 4.2.5. A 5 mM stock solution of I4S was reduced as described in Section 4.4.2.2. A 20 mM stock solution of methyl viologen (MV) was reduced in the glovebox as described in Section 2.2.6.

5.2.4. Preparation of the ccNiR/nitrite tonometers

For each stopped-flow experiment, 80 μ L of 100 mM nitrite stock and an aliquot of ccNiR were combined in a glovebox with enough degassed assay buffer to give a total volume of 8 mL, after which the solution was transferred to a tonometer. The exact volume of the ccNiR aliquot varied depending on the concentration of the ccNiR stock from which it was obtained, which in turn was determined by UV/Vis spectroscopy. In all cases, the final concentrations once the tonometer contents were mixed on the stopped-flow should be 500 μ M Nitrite, and 1 – 2 μ M ccNiR.

5.2.5. Preparation of the I3S_{FR} Tonometers

Tonometers with I3S_{red} concentrations varying from 60-240 μ M were prepared to ensure that the final concentration after stopped-flow mixing varied from 30-120 μ M. The first tonometer was made by transferring 288 μ L of 5 mM I3S_{FR} stock solution to the tonometer and diluting to 6 mL with degassed buffer, creating a concentration of 240 μ M I3S_{red}. The second sample was made by transferring 252 μ L of 5 mM I3S_{red} stock solution to the tonometer and diluting to 6 mL with degassed buffer, creating a concentration of 210 μ M I3S_{FR}. The next

sample was made by transferring 216 μL of 5 mM I3S_{red} stock solution to the tonometer and diluting to 6 mL with degassed buffer, creating a concentration of 180 μM I3S_{red} . The next sample was produced by transferring 180 μL of 5 mM I3S_{red} stock solution to the tonometer and diluting to 6 mL with degassed buffer, creating a concentration of 150 μM I3S_{red} . The next sample was created by transferring 144 μL of 5 mM I3S_{red} stock solution to the tonometer and diluting to 6 mL with degassed buffer, creating a concentration of 120 μM I3S_{red} . The next sample was produced by transferring 108 μL of 5 mM I3S_{red} stock solution to the tonometer and diluting to 6 mL with degassed buffer, creating a concentration of 90 μM I3S_{red} . The final sample was created by transferring 72 μL of 5 mM I3S_{red} stock solution to the tonometer and diluting to 6 mL with degassed buffer, creating a concentration of 60 μM I3S_{red} .

5.2.6. Preparation of the I3S_{PR} Tonometer

A tonometer containing 160 μM I3S_{PR} was made by diluting 128 μL of 5mM I3S_{PR} stock solution to 4 mL with degassed buffer.

5.2.7. Preparation of the I4S_{FR} Tonometers

The first tonometer containing I4S_{FR} was made by diluting 32 μL of 5 mM I4S_{FR} stock to a final volume of 8 mL with degassed buffer to give a concentration of 20 μM in solution. A second I4S_{FR} sample with a concentration of 10 μM was produced by adding 16 μL of 5 mM I4S_{FR} stock to a tonometer and diluting to 8 mL with degassed buffer.

5.2.8. Preparation of the MV_{red} Tonometer

The tonometer which held MV_{red} was created to contain 200 μM MV_{red} . This was completed by adding 40 μL of 20 mM MV_{red} and diluting to 4 mL with degassed buffer.

5.2.9. Reduction of nitrite-loaded *S. oneidensis* ccNiR by various reductants: Stopped-flow experiments

A single mixing SX-20 stopped-flow spectrophotometer (Applied Photophysics) was used to monitor the pre-steady-state kinetics of nitrite-loaded ccNiR_{WT} reduction by MV_{red}, partially and fully reduced I3S, and fully reduced I4S. In preparation for the experiments, a 20 mL mixture of 20 mM α -D-glucose (0.0721 g) and 15 U/mL *Aspergillus niger* glucose oxidase (3 mg, MP biomedical) enzyme was used to scrub oxygen from the stopped-flow apparatus. Lyophilized glucose oxidase and glucose were dissolved in buffer inside a glovebox, and the solution was transferred to a tonometer to which the stopcocks and caps were greased with Apiezon M Economical High-Vacuum Lubricant. The sealed tonometer was removed from the glovebox and connected to one of the stopped-flow loading ports, from which both stopped flow syringes and the observation cell could subsequently be filled with the scrubbing solution, according to the instructions provided in the SX-20 manual. This solution was flushed through the stopped-flow apparatus and left in the stopped-flow overnight to make the system completely anaerobic, after which it was washed out with anaerobic 50 mM HEPES, pH=7.0 buffer, again following the SX-20 manual instructions. Stock reagent solutions were made in a glovebox as described previously in Chapter 2, Sections 2.2.6. A tonometer containing only buffer was also prepared in the glovebox, and the solution from this tonometer was used to wash out the glucose-glucose oxidase scrubbing solution (see above) and was also used to blank the stopped-flow spectrophotometer. The tonometer containing nitrite-loaded ccNiR was used to fill one of the stopped-flow drive syringes, while a sample containing one of the reducing agents was used to fill the other in the subsequent experiments. The solutions were mixed 1:1 by the stopped-flow

drive piston. Data sets were collected on varying timescales from 0.01s to 1000s. Each experiment conducted at a certain reductant concentration was repeated three times and the dataset signals were averaged. All the data were collected in photodiode array (PDA) mode. Data were collected in CSV format and later analyzed by using programs written for Mathcad 15.0 (PTC Software) and Origin 9.0 (Microcal Software).⁸

5.3. Results and discussion

Each dataset was completed in triplicate. A Mathcad program called “Averager” was used to average a triplicate data set at a particular timescale. The Averager program output a file to the current folder labeled “Averaged data.csv”. Next, a program called “Step 1 submatrix former” was opened that automatically imports the “Averaged data” file and displays the first time-resolved spectrum for inspection. This program allows the user to trim out short wavelength data that are often off-scale, using fine- and coarse-scale sliders to adjust the cutoff wavelength. The program automatically exports a file called “truncated data set.csv”. It also exports a file that contains difference spectra, which are formed by subtracting the first spectrum in the time resolved series from the rest. For some cases, it may be useful to analyze difference spectra instead of the absolute spectra, though this was not done in the studies reported herein.

The third program, called “Step 2 SVD” is analogous to the Step 3 program in the Chapter 3 analysis. As with the earlier program, “Step 2 SVD” exports three files: absorbance.csv, wavelength.csv, and time.csv. These files serve as the input for the fourth program called “step 3 kinetic fit”, which fit the data to a kinetic model. The exact model used depended on the data set being analyzed, as is described in more detail below. Whatever model was used, “step 3 kinetic fit” exported a csv file containing spectral components, which could eventually be fit with independently obtained extinction coefficient spectra, to determine what

species were contributing to each component. This was not yet done in the work covered in the chapter.

5.3.1. Partially Reduced I3S as the electron source

The stopped-flow experiments completed with partially reduced I3S were obtained at the timescales 1 s to 40 s. The singular value decomposition (SVD) analysis suggested that there are three spectral components, including the component at $t = 0$, so the data were fit to an $A \rightarrow B \rightarrow C$ model (Scheme 5.1).⁶ In Figure 5.1, the spectral changes observed after mixing ~ 1 mM ccNiR and 500 mM nitrite with 80 μ M I3S_{PR} have been plotted for the 100 ms and 5 s time intervals. From 100 ms to 5 s, there is a visible decrease in the 409 nm peak and an increase in the peak at 600 nm, suggesting that the ccNiR hemes are reducing, while I3S is re-oxidizing. The spectral changes with time are more clearly seen in Fig. 5.2, which shows absorbance vs time traces from Fig. 5.1 at 401 nm, 424 nm, and 598 nm. The $A_{401\text{nm}}$ trace decreases while the $A_{598\text{nm}}$ trace increases; the $A_{424\text{nm}}$ initially increases but begins to decrease after 1 s. The calculated fits for each trace (dotted red curves) begin to diverge after nearly 20s, but less so at 598 nm than 401 nm and 424 nm, suggesting that the re-oxidation of I3S is finished after 50s, but heme re-oxidation may be taking place on a longer timescale, which is not captured by the current fitting model.

Figure 5.3 shows the spectral component present at $t = 0$ ($\Lambda_{0(\lambda)}$, Scheme 5.1). The 409 nm band shows that ccNiR is still mostly or completely oxidized at $t = 0$, and that I3S is mostly oxidized as well. Figure 5.4 shows the spectral component that grows in with a half-life of 111 ms and corresponds to $\Lambda_{1(\lambda)}$ in Scheme 5.1. Some I3S oxidation has taken place on this timescale (peak at 585 nm), but the most prominent signals are due to *c*-heme reduction. The 525 nm and 554 nm are diagnostic of bis-His heme reduction, most likely because Heme #4 (Fig. 1.2c) is

$$A_{\lambda,t} = \Lambda_{0(\lambda)} + \Lambda_{1(\lambda)}f_1(t) + \Lambda_{2(\lambda)}f_2(t)$$

where:

$$f_1(t) = \frac{k_1}{k_1 - k_2} [\exp(-k_1t) - \exp(-k_2t)]$$

$$f_2(t) = \frac{1}{k_1 - k_2} \{k_2 [1 - \exp(-k_1t)] - k_1 [1 - \exp(-k_2t)]\}$$

$$k_{1app} = 6.23 \text{ s}^{-1} (t_{0.5} = 111 \text{ ms})$$

$$k_{2app} = 0.145 \text{ s}^{-1} (t_{0.5} = 4.8 \text{ s})$$

Scheme 5.1. The kinetic model for the partially reduced I3S data.

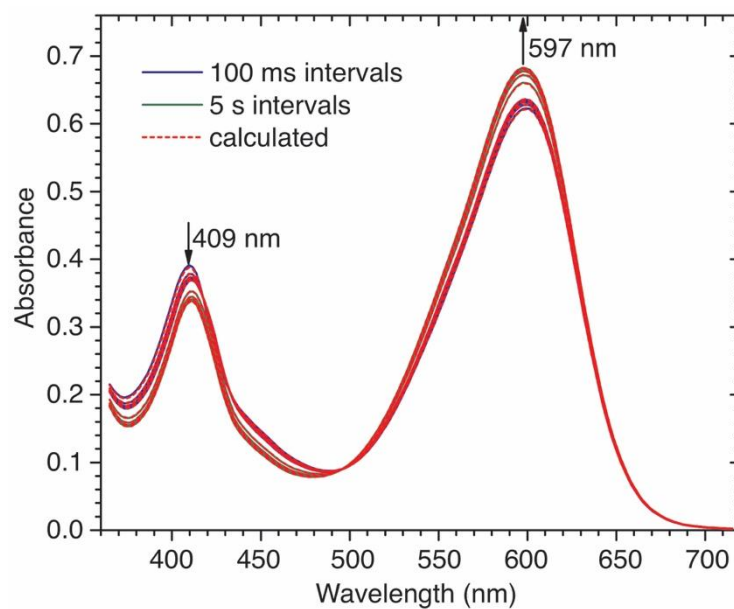


Figure 5.1. Spectral changes observed at selected times after mixing $\sim 1 \mu\text{M}$ ccNiR and 500 mM nitrite with $80 \mu\text{M}$ I3S_{PR}.

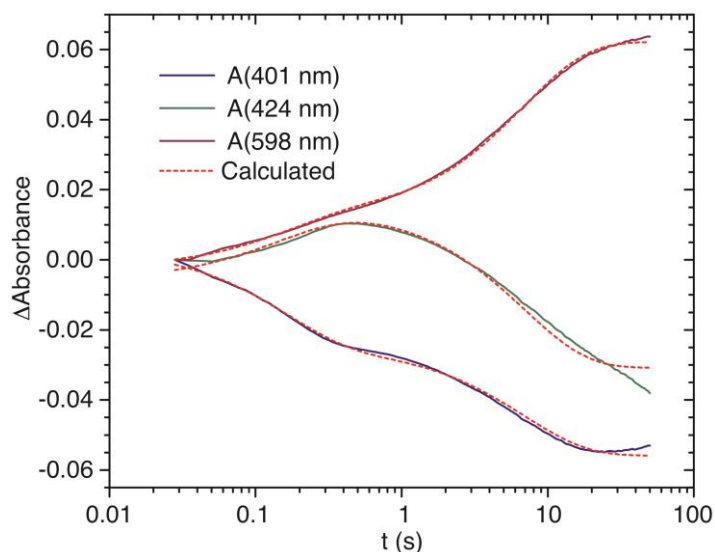


Figure 5.2. Absorbance vs time traces at specific wavelengths obtained from the Fig. 5.2 data.

reducing. The 401 nm and 424 nm features could be due to a bis-His heme reduction, active site reduction, or possibly both. The spectral component that grew in with a half-life of 4.5 s (associated with $\Lambda_{2(\lambda)}$, Scheme 5.1) is presented in Fig. 5.5, and shows that the major change

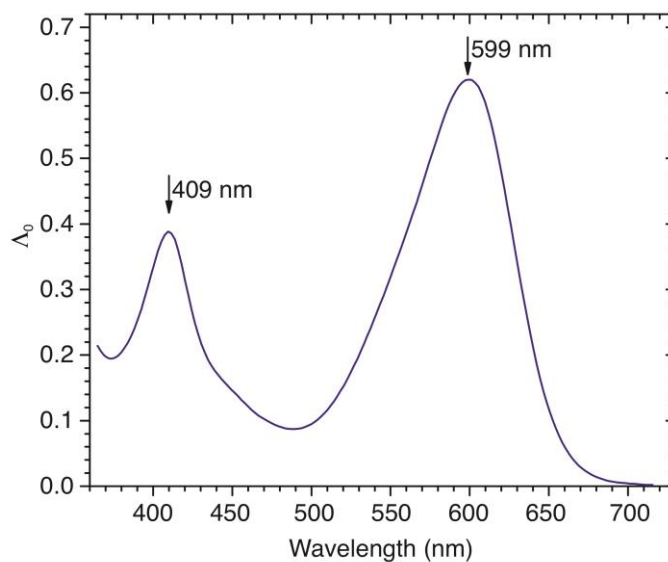


Figure 5.3. Spectral component that was present at $t = 0$ after mixing $\sim 1 \mu\text{M}$ ccNiR and 500 mM nitrite with $80 \mu\text{M}$ I3SPR.

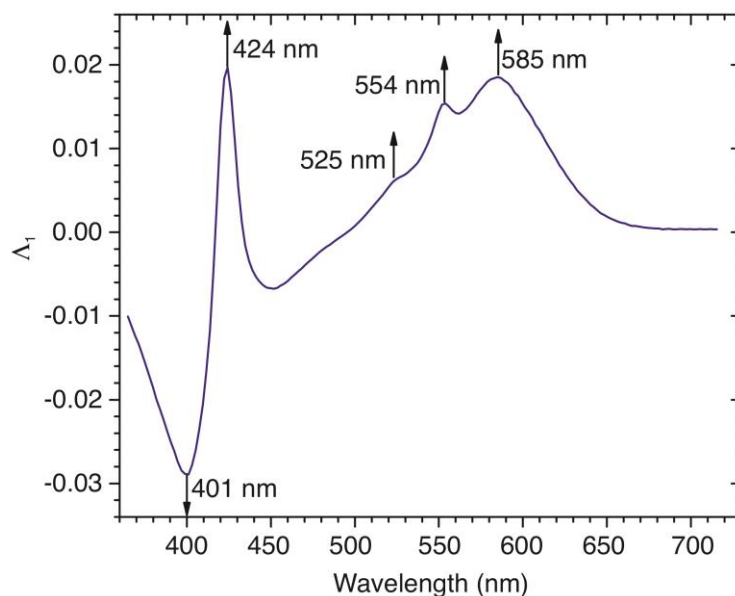


Figure 5.4. Spectral component that grew in with a half-life of 111 ms after mixing $\sim 1 \mu\text{M}$ ccNiR and 500 mM nitrite with $80 \mu\text{M}$ I3S_{PR}.

occurring is I3S re-oxidation. Peaks that are diagnostic of heme reduction are visible, however, it appears that most (if not all) of the heme reduction occurred on the millisecond timescale. From

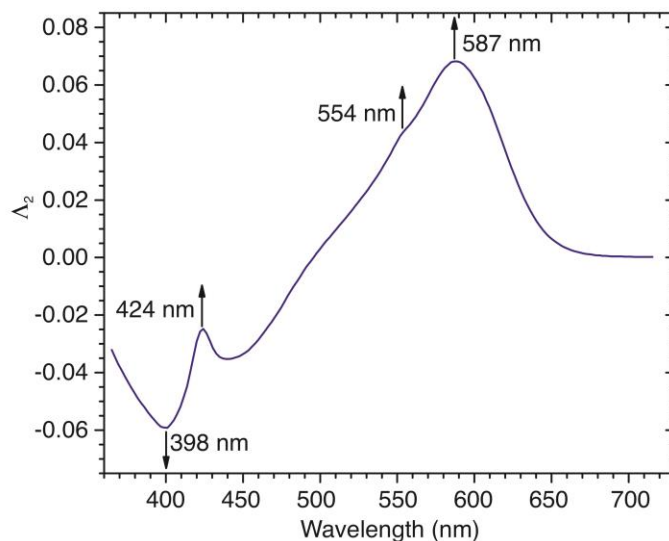


Figure 5.5. Spectral component that grew in with a half-life of 4.8 s after mixing $\sim 1 \mu\text{M}$ ccNiR and 500 mM nitrite with $80 \mu\text{M}$ I3S_{PR}.

the results, I3S re-oxidation is completed by 50s. Heme reduction occurs on the millisecond timescale. Heme re-oxidation seems to happen on a longer timescale, which can be inferred from the deviation from the fits in Fig. 5.2. To see if any heme reduction had taken place at time zero (Fig. 5.3), the data would need to be fit with the extinction coefficient spectra of I3S_{ox}, I3S_{red}, and ccNiR_{ox}.

5.3.2. Fully Reduced I3S as the electron source

The analysis for varying concentrations (45-120 μM) of I3S_{FR} resulted in a dataset with four spectral components in the SVD. Hence, the data were fit to a model $A \rightarrow B \rightarrow C \rightarrow D$. Most interesting were the S_1 components, corresponding to appearance of species B, which are shown in Fig. 5.6 for the various I3S_{FR} concentrations. These components grew in with half-lives of less than 10 ms and show the 525 nm and 554 nm bands characteristic of bis-his-ligated heme reduction, in addition to the 424 nm band characteristic of *c*-heme reduction in general. Notably, there is no underlying broad band in the 520 – 570 nm region, which might have been attributed to active site heme 1 reduction;^{5,6} the broad band centered around 600 nm is attributable to I3S oxidation. Thus, it appears that electrons populate the ccNiR bis-His heme pool before being transferred to the nitrite-loaded heme 1 active site when I3S_{red} provides the electrons, even though the midpoint potential of nitrite-loaded heme 1 is almost 300 mV higher than that of heme 4, which has the next highest midpoint potential.^{1,5}

Figure 5.7 shows that k_{1obs} varies linearly with I3S concentration, which is what one would expect if I3S_{red} is directly reducing the ccNiR bis-His heme pool in a process that is first-order in [I3S_{red}], first-order in [ccNiR], and second-order overall. Importantly, the k_{1obs} value is about 100 \times higher than k_{2obs} which governs conversion of B to C, even at the lowest I3S_{red}

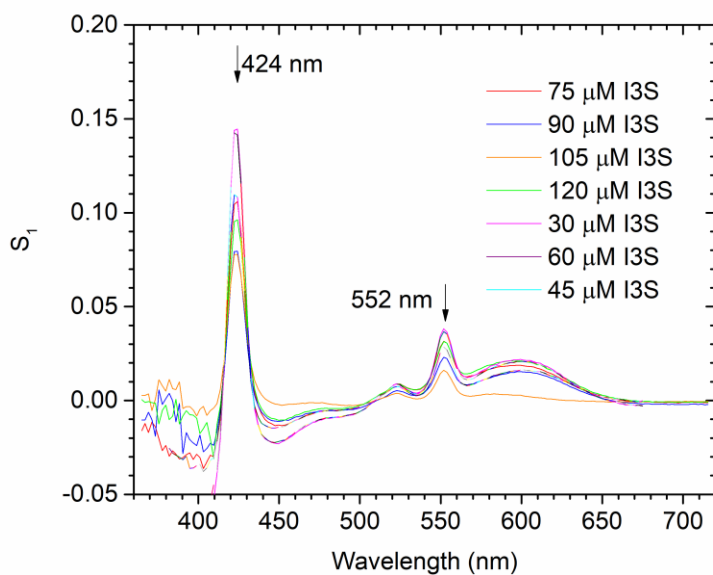


Figure 5.6. Spectral component that grew in ~ 1 s with $I3S_{FR}$ at varying concentrations, $\sim 1 \mu M$ ccNiR and 500 mM nitrite.

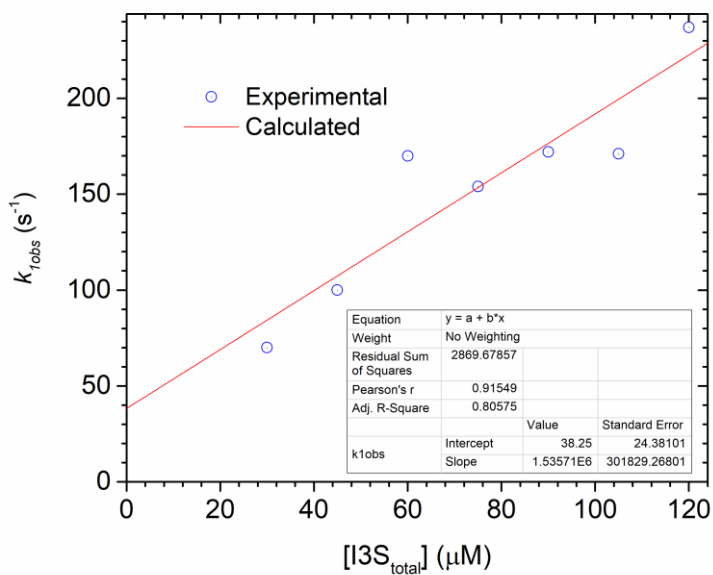


Figure 5.7. Rate constant k_{obs} for the reactions described in Figure 5.6. (Linear fit shown as a solid red line.)

concentration studied, 30 mM. This means that the intermediate with the bis-His heme pool reduced and the nitrite-loaded active site still oxidized should be easily trappable using the rapid freeze-quench method and then studied by EPR. In fully oxidized ccNiR, the active site interacts magnetically with at least one and maybe two of the bis-His hemes, which makes EPR spectra difficult to interpret. With one or more bis-His hemes reduced and the nitrite-loaded active site still in the ferric state, at least some of the magnetic coupling would be eliminated, which could help greatly in EPR data interpretation.

5.3.3. Fully Reduced I4S as the electron source

The stopped-flow data using I4S were analyzed in the same manner as those using the fully reduced I3S data. The timescales evaluated were from 1 s to 1000 s. An analysis using SVD suggested that there were four components contributing to the reaction. From the 500 s dataset, the spectral component at time zero showed some heme reduction had occurred, which can be seen at the 409nm peak. At this time point, some re-oxidation of I4S had also taken place. The first spectral component with a half-life of 1.77 s shows that heme reduction has taken place by the shift in the Soret band from 409 nm to 424 nm. There is a visible peak at 552 nm that represents the reduction of the bis-his ligated heme, however a 522 nm peak is not visible yet, which may be because the band is hidden under the one due to I4S re-oxidation. The second spectral component that appeared with a half-life of 53 s shows that heme reduction is still occurring visibly at the 522 and 552 nm peaks, however the absorbance of the Soret band is constant from the first spectral component. More I4S re-oxidation has taken place which is visible at the 584 nm peak. From the stopped-flow data, the information that was obtained was that heme reduction and I4S re-oxidation appear to have occurred on a much slower timescale,

and heme re-oxidation was not visible at all. This is expected since I4S is a slightly weaker reducing agent than I3S.

To follow reactions occurring on longer timescales, conventional UV/Vis spectroscopy was used. In one such experiment, 500 mM nitrite, 10 μ M I4S, and 2 μ M ccNiR were mixed in a cuvette inside of the glovebox and left to react for an hour. The reaction was monitored in cycle mode (spectrum taken every 15 seconds) using the UV/vis spectrophotometer. After the data were collected, spectra at ten different time increments were extracted from the data and plotted (Fig. 5.8). At $t = 0$, the 552 nm peak is visible, attributable to bis-His heme reduction. However, this peak is no longer detectable after 3.75 minutes. Importantly, I4S reoxidation appeared to level off by $t = 22.5$ min. It is unclear from visual inspection whether the heme 1 active site remains reduced at $t = 22.5$ min because the I4S bands dominate the spectrum, but this question could be answered in future by quantitatively analyzing the spectral components using independently obtained I4S and ccNiR extinction coefficient spectra.⁶

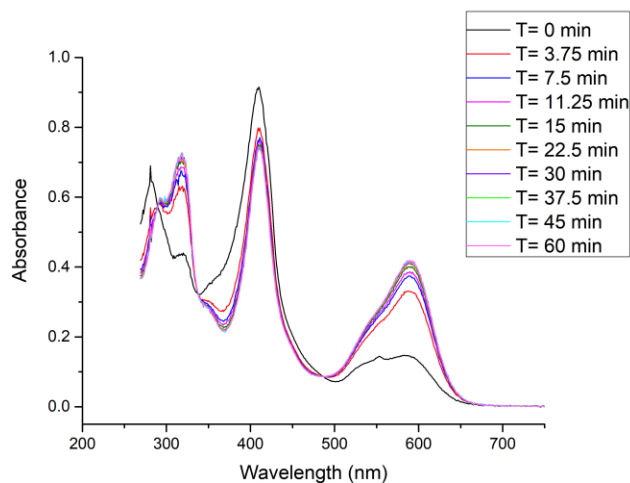


Figure 5.8. Spectra extracted at different timescales from the reaction of 10 μ M I4S, 2 μ M ccNiR, and 500 mM Nitrite produced from a UV-visible spectrophotometer run on cycle mode.

5.3.4. Reduced methyl viologen as the electron source

The stopped-flow experiments using MV_{red} were completed with collection timescales from 10 ms to 10 s. An analysis using SVD suggested that there are six spectral components contributing to the reaction, so the data sets were fit to the differential equations shown in Scheme 5.2. Note though that the first three rate constants in Scheme 5.2 provide a purely empirical fit and have no readily interpretable chemical significance.

Observe 6 SVD spectral components. Fit with the following differential equations:

$$\begin{aligned} \frac{dC_1}{dt} &= -k_1 C_1 \\ \frac{dC_2}{dt} &= k_1 C_1 - k_2 C_2 \\ \frac{dC_3}{dt} &= k_2 C_2 - k_3 C_3 \\ \frac{dC_4}{dt} &= k_3 C_3 - k_4 C_4 \\ \frac{dC_5}{dt} &= k_4 C_4 - k_5 C_5 \\ \frac{dC_6}{dt} &= k_5 C_5 \end{aligned}$$

Initial conditions:

$$(C_1)_0 = 1$$

$$(C_2)_0 - (C_6)_0 = 0$$

Beer's law fit:

$$\Lambda = (C^T \cdot C)^{-1} C^T \cdot A_{\text{exper}}$$

$$A_{\text{calc}} = C \cdot \Lambda$$

Scheme 5.2. The differential equations that were applied to analyze the ccNiR-mediated reduction of nitrite using the strong reductant MV_{red} .

Figure 5.9 focuses on the spectral changes observed in the first 20 ms after mixing ~1 mM ccNiR and 500 mM nitrite with 200 μM MV_{red} . MV_{red} was re-oxidized in the first 20 ms of mixing; however, ccNiR remained significantly reduced after this time. The spectral changes observed between 20 ms and 10 s are shown in Fig. 5.10. The Soret band of oxidized ccNiR is at ~409 nm and the Q-band absorbs at ~530 nm. However, upon reduction, the Soret band shifts from 409 nm to ~424 nm, and the Q-band splits into bands at 522 nm and 552 nm. At 20 ms, the

Soret band has shifted to 420 nm, while there are two visible bands at 522 and 552 nm, showing that the enzyme is in a reduced state. However, from 20 ms to 10 s, there is a decrease in absorbance at 420 nm, 522 nm, and 552 nm, but an increase in absorbance at 412 nm, conveying that heme re-oxidation is occurring during this time. The re-oxidation of ccNiR is best followed visually in the $A_{420\text{nm}}$ vs t (s) trace in Fig. 5.11, which shows that the 10 s stopped-flow run only captures a little over a half-life of the final re-oxidation step. A deeper look into the heme reduction and re-oxidation is provided in Figs 5.12 to 5.14. Figure 5.12 is the UV/Vis absorbance spectrum taken after 30 ms from the Fig. 5.10 data set. By this time, all the MV_{red} has re-oxidized and only ccNiR is contributing to the spectrum. This spectrum shows extensive bis-His heme reduction (Fig. 1.2c), as evidenced by the prominent signals at 420 nm, and especially at 522 nm and 552 nm.

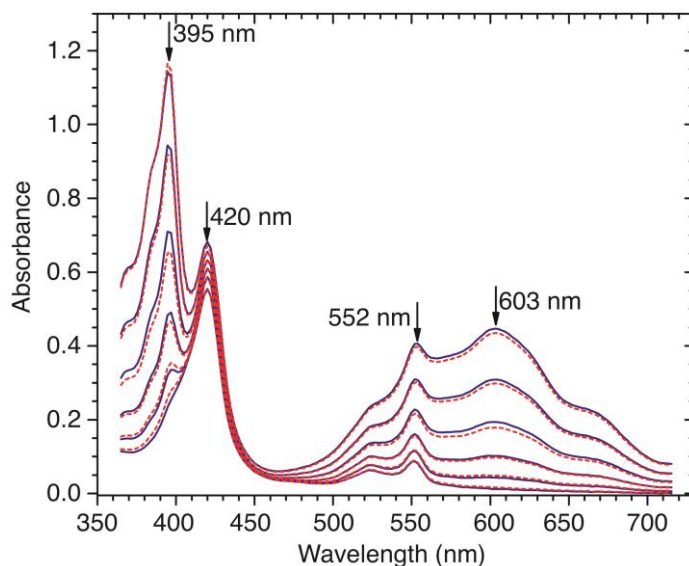


Figure 5.9. Spectral changes observed in the first 20 ms after mixing $\sim 1 \mu\text{M}$ ccNiR and 500 mM nitrite with 200 μM methyl viologen monocation radical (MV_{red}).

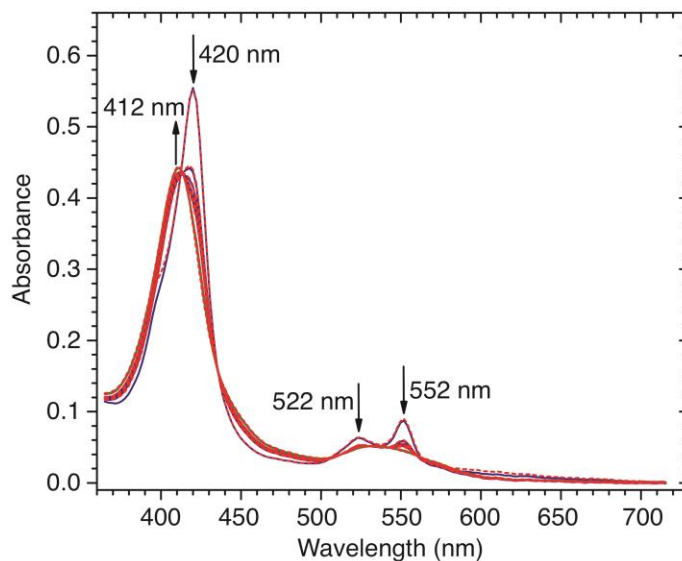


Figure 5.10. Spectral changes observed between 20 ms and 10 s after mixing ~ 1 mM ccNiR and 500 mM nitrite with 200 μ M methyl viologen monocation radical (MV_{red}). The dotted red curves are the fits obtained with the Scheme 4.2 model.

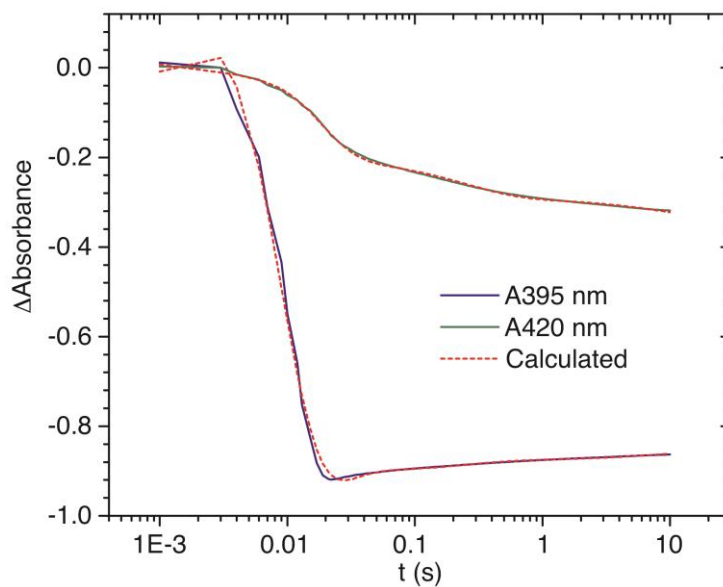


Figure 5.11. Spectral traces observed after mixing ~ 1 μ M ccNiR and 500 mM nitrite with 200 μ M methyl viologen monocation radical (MV_{red}). The dotted red curves are the fits obtained with the Scheme 4.2 model.

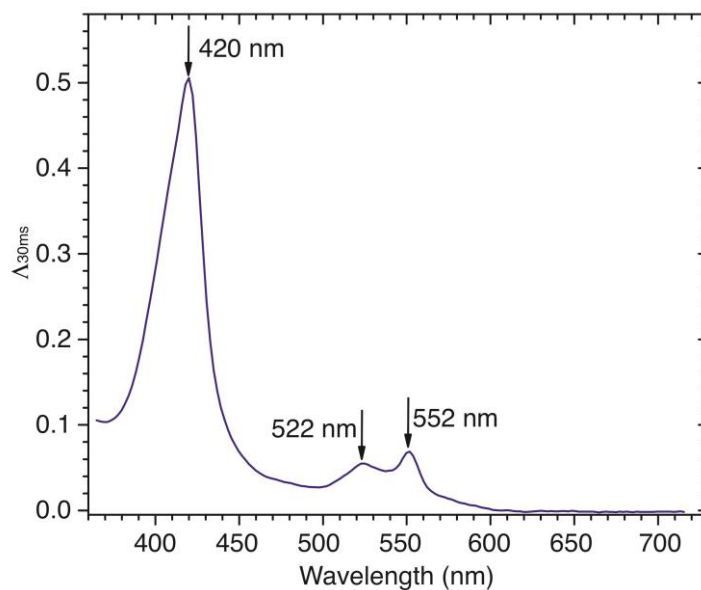


Figure 5.12. UV/Vis absorbance spectrum taken after 30 ms from the Fig. 5.10 data set. The spectrum shows extensive bis-His heme reduction.

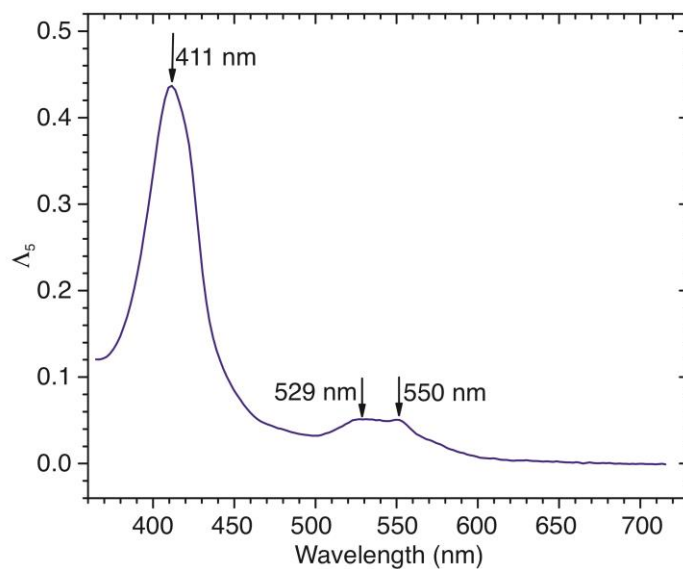


Figure 5.13. The fifth spectral component obtained in the fit of the stopped-flow data presented in Fig. 5.10 with the Scheme 5.2 model. This component appears with a half-life of ~ 170 ms.

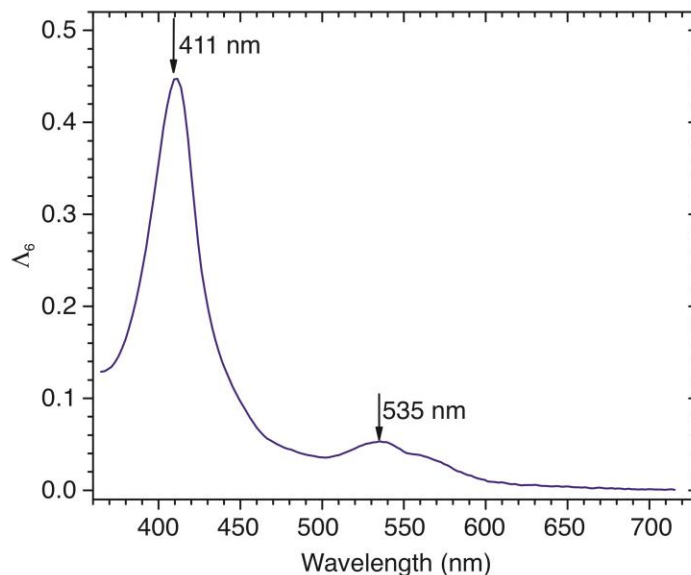


Figure 5.14. The sixth spectral component obtained in the fit of the stopped-flow data presented in Fig. 5.10 with the Scheme 5.2 model. This component appears with a half-life of ~ 6.5 s.

Figure 5.13 is the fifth spectral component obtained in the fit of the stopped-flow data presented in Fig. 5.10 with the Scheme 5.2 model. This component appears with a half-life of ~ 170 ms. In this spectral component, there is no longer a 420 nm peak, which suggests that significant heme re-oxidation has occurred; however, the Soret band is at 411 nm rather than at 409 nm, suggesting that the enzyme is not fully oxidized. Furthermore, though the peaks at 522 nm and 552 nm have decreased significantly in size, a 550 nm peak in particular is still clearly present, which conveys that at least one bis-his ligated heme remains reduced after 850 ms.

Finally, the sixth spectral component that appears with a half-life of ~ 6.5 s is shown in Fig. 5.14. At first glance, this spectrum is like that of fully oxidized ccNiR. However, there is still a slight shift in the Soret band, from 409 nm to 411 nm, and the 535 nm band is slightly broadened in the red region, which suggests that the active site is still in the reduced state.

To summarize, the stopped-flow experiments with MV_{red} show that, even though the MV_{red} is re-oxidized within 20 ms of mixing, The ccNiR hemes remain reduced for much longer. Furthermore, these hemes re-oxidize at timescales sufficiently different from each other so as to allow the relatively facile trapping of distinct partially reduced intermediates using the rapid freeze-quench method. The trapped intermediates could, in turn, be analyzed by EPR and Mossbauer spectroscopy. As noted earlier with the I3S_{red} data (Section 5.3.2), in fully oxidized ccNiR, the active site interacts magnetically with at least one and maybe two of the bis-His hemes, which makes EPR spectra difficult to interpret. With one or more bis-His hemes reduced and the nitrite-loaded active site still in the ferric state, at least some of the magnetic coupling would be eliminated, which could help greatly in EPR data interpretation. A better understanding of the EPR spectra will be essential for characterizing the ccNiR reactive intermediates that accumulate under various reaction conditions, which in turn will allow the ccNiR reaction mechanism to be worked out.

5.4 References

- (1) Stein, N.; Love, D.; Judd, E. T.; Elliott, S. J.; Bennett, B.; Pacheco, A. A. Correlations between the electronic properties of *Shewanella oneidensis* cytochrome *c* nitrite reductase (ccNiR) and its structure: effects of heme oxidation state and active site ligation. *Biochemistry* **2015**, *54*, 3749-3758.
- (2) Judd, E. T.; Youngblut, M.; Pacheco, A. A.; Elliott, S. J. Direct Electrochemistry of *Shewanella oneidensis* Cytochrome *c* Nitrite Reductase: Evidence of Interactions across the Dimeric Interface. *Biochemistry* **2012**, *51* (51), 10175-10185. Judd, E. T.; Stein, N.; Pacheco, A. A.; Elliott, S. J. Hydrogen bonding networks tune proton-coupled redox steps during the enzymatic six-electron conversion of nitrite to ammonia. *Biochemistry* **2014**, *53*, 5638-5646.
- (3) Youngblut, M.; Pauly, D. J.; Stein, N.; Walters, D.; Conrad, J. A.; Moran, G. R.; Bennett, B.; Pacheco, A. A. *Shewanella oneidensis* cytochrome *c* nitrite reductase (ccNiR) does not disproportionate hydroxylamine to ammonia and nitrite, despite a strongly favorable driving force. *Biochemistry* **2014**, *53*, 2136-2144.
- (4) Bykov, D.; Plog, M.; Neese, F. Heme-bound nitroxyl, hydroxylamine, and ammonia ligands as intermediates in the reaction cycle of cytochrome *c* nitrite reductase: a theoretical study. *J. Biol. Inorg. Chem.* **2014**, *19*, 97-112.
- (5) Ali, M.; Stein, N.; Mao, Y.; Shahid, S.; Schmidt, M.; Bennett, B.; Pacheco, A. A. Trapping of a putative intermediate in the cytochrome *c* nitrite reductase (ccNiR)-catalyzed reduction of

nitrite: implications for the ccNiR reaction mechanism. *J. Am. Chem. Soc.* **2019**, *141*, 13358-13371. DOI: 10.1021/jacs.9b03036.

(6) Shahid, S.; Ali, M.; Legaspi-Humiston, D.; Wilcoxon, J.; Pacheco, A. A. A kinetic investigation of the early steps in cytochrome *c* nitrite reductase (ccNiR)-catalyzed reduction of nitrite. *Biochemistry* **2021**, *60*, 2098-2115.

(7) Berry, E. A.; Trumpower, B. L. Simultaneous determination of hemes a, b, and c from pyridine hemochrome spectra. *Anal. Biochem.* **1987**, *161*, 1-15. Barr, I.; Guo, F. Pyridine hemochromagen assay for determining the concentration of heme in purified protein solutions. *Bio. Protoc.* **2015**, *5*, (18).

(8) Koebke, K. J.; Pauly, D. J.; Lerner, L.; Liu, X.; Pacheco, A. A. Does the oxidation of nitric oxide by oxymyoglobin share an intermediate with the metmyoglobin-catalyzed isomerization of peroxynitrite? *Inorg. Chem.* **2013**, *52*, 7623-7632. Koebke, K. J.; Waletzko, M. T.; Pacheco, A. A. Direct monitoring of the reaction between photochemically generated nitric oxide and *Mycobacterium tuberculosis* truncated hemoglobin N wild type and variant forms: an assessment of computational mechanistic predictions. *Biochemistry* **2016**, *55*, 686-696.

Chapter 6 The Crystallographic Search for the Two Electron Reduced ccNiR Intermediate

6.1. Overview

The first crystal structure of the ccNiR homologue from *S. oneidensis* was obtained at room temperature using the Laue method (2.59 Å PDB 3UBR).¹ Recently, a low temperature structure was also captured at an even higher resolution (1.66 Å, PDB 6P73)². Both crystal structures revealed that the *S. oneidensis* enzyme is structurally similar to the previously characterized ccNiR homologues from *Wolinella succinogenes*,³ *E. coli*,⁴ *Sulfurospirillum deleyianum* (1.9 Å),⁵ *Desulfovibrio desulfuricans*,⁶ *Desulfovibrio vulgaris*,⁷ and *Haemophilus influenzae*⁵.

An advantage of the Laue method is that it produces picosecond X-Ray pulses, which allow “snapshot” crystal structures to be obtained at different times following the initiation of a reaction within a crystal. Stop-motion “movies” of reactions can then be generated by putting a series of snapshots together. Another advantage of the Laue method’s picosecond pulses is that they are short enough that data collection outruns X-ray damage to some extent, though some damage is captured in Laue diffraction patterns. Set against its advantages, the Laue method also has several limitations. In order to use the method, large crystals (>50 µm) must be grown, which has proven to be tricky with ccNiR, whose ability to crystallize is rather batch-dependent. Another limitation of the Laue method is that a polychromatic beam is used, and analysis of such data sets is more challenging than analysis collected with a monochromatic X-ray source.

An alternative to the Laue method for doing time-resolved crystallography, that has become available over the last ten years, is Serial Femtosecond X-ray Crystallography (SFX). SFX utilizes an X-ray Free Electron Laser (XFEL) that produces laser pulses on the femtosecond timescale. Such ultrashort laser pulses allow data collection to easily outrun X-ray damage,

which is especially useful when probing redox-active proteins such as ccNiR that are particularly prone to such damage. In addition to providing ultrashort laser pulses, another advantage of XFELs is that they require very small crystals (<50 μm).⁸ The SFX method was useful in crystallographic studies of the large membrane protein Photosystem II, which has a molecular weight near 350 kDa. This study produced not only a crystal structure of Photosystem II, but gave insight into the mechanism of the Oxygen Evolving Complex (OEC).⁹

SFX uses two sample injection approaches: pump-probe and mix-and-inject. In the pump-probe method changes are induced within a crystal by a rapid temperature change of the solvent surrounding a protein (ns), by releasing a photocaged compound in the crystal, or by inducing a change in a photoactive protein (ns- μs). In each case, the changes are initiated by ns laser pulses of visible or infrared light. The Mix and Inject approach involves the rapid mixing (μs -ms) of micro-crystals with a substrate using a T-junction (Fig. 6.1). Furthermore, the distance between the T-junction and the X-ray beam can be modified in order to vary the times available for reaction between protein crystals and substrate¹⁰.

As mentioned in Chapter 1 Section 1.13.2, stopped-flow and UV/Vis spectropotentiometric studies revealed an observable accumulation of two transient intermediates during the reduction of nitrite-loaded ccNiR by the weak reductant TMPD, which were assigned as the short-lived one-electron reduced species $\text{Fe}_{\text{HI}}^{\text{II}}(\text{NO}_2^-)$ and the long-lived $\{\text{Fe}_{\text{HI}}(\text{NO})\}$ ⁷ species.¹¹ This chapter describes preliminary efforts ultimately aimed at characterizing the one- and two-electron reduced ccNiR intermediates using SFX. The proposed strategy will use the mix-and-inject approach to mix ccNiR micro-crystals with nitrite and then to further mix the crystals with a weak reductant to generate the intermediates. First, a baseline crystal structure of ccNiR micro-crystals will be obtained. Next, a crystal structure of nitrite-loaded ccNiR micro-

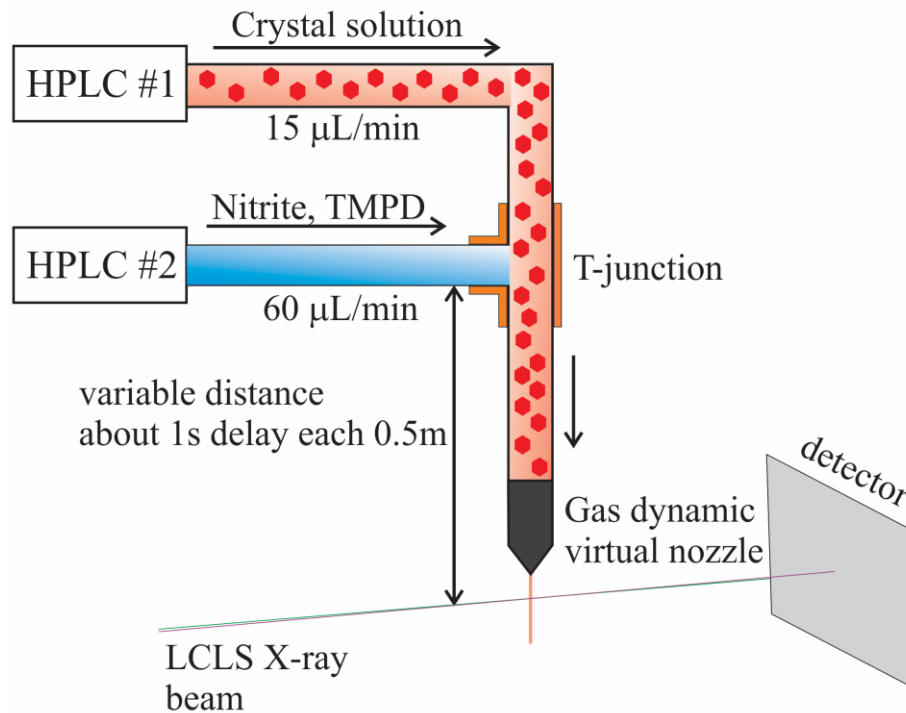


Figure 6.1. A schematic representation of ccNiR microcrystals flowing through the injector to be struck by the X-ray beam. A diffraction pattern is created on the detector and later used to obtain a crystal structure.

crystals will be collected, and lastly, the ccNiR-catalyzed reduction of nitrite will be probed. The SFX experiments could show the orientation of nitrite and NO in the partially reduced active site relative to the key R103, Y206, and H257 residues, which is information not readily obtainable by any other method. Such information would complement the information about the active site electronic structure being obtained in EPR experiments.

6.2. Materials and methods

All reagents were of high bio-grade purity and purchased from Thermo-Fisher, Dot Scientific, or MP Biomedicals, unless specified otherwise.

6.2.1. Formation of ccNiR microcrystals

CcNiR enzyme was purified as described in Chapter 2 and concentrated to a final concentration of 30 mg/mL. A typical precipitant solution was 32% w/v polyethylene glycol 4000 (PEG 4000) in 50 mM Triethanolamine (TEA) pH 7 buffer (but see Section 6.2.3 below). To generate microcrystals, 30 μ L each of stock ccNiR and precipitant were mixed in an Eppendorf tube, creating a slurry with a final concentration of 15 mg/mL ccNiR, 16% w/v PEG 4000. This slurry was left to crystallize at room temperature over the course of 2-4 weeks while briefly agitating the slurry every other day to increase the number of nucleation sites.

6.2.2. Test for the catalytic activity of ccNiR microcrystals

The standard methyl viologen assay was adapted to assess the activity of the microcrystals. First, microcrystals were made inside of the glovebox using the degassed precipitant solution and crystallization method described in Section 6.2.1. The slurry was left in the glovebox for 2 weeks to allow for crystal formation. Methyl viologen was reduced and the standard assay conducted in the same manner described in chapter 2, with the following slight modifications. Degassed precipitant solution replaced the 50mM HEPES Free Acid pH 7 buffer, and the stock nitrite solution was made with the precipitant solution as well. Three trials of the standard assay were completed with concentrations of 200 mM MV_{red}, 500 mM nitrite, and $(10^9)\times$, $(5\times 10^{10})\times$, and $(1\times 10^{10})\times$ dilutions of ccNiR anaerobic microcrystal stock, respectively, as the source of ccNiR (Fig. 6.2).

6.2.3. Preliminary screening tests for and investigation of serial femtosecond X-ray crystallography

In preparation for a run at the European XFEL, two different crystallization conditions were used in the Schmidt Lab, Milwaukee, WI, USA. Condition 1 started from a protein stock:

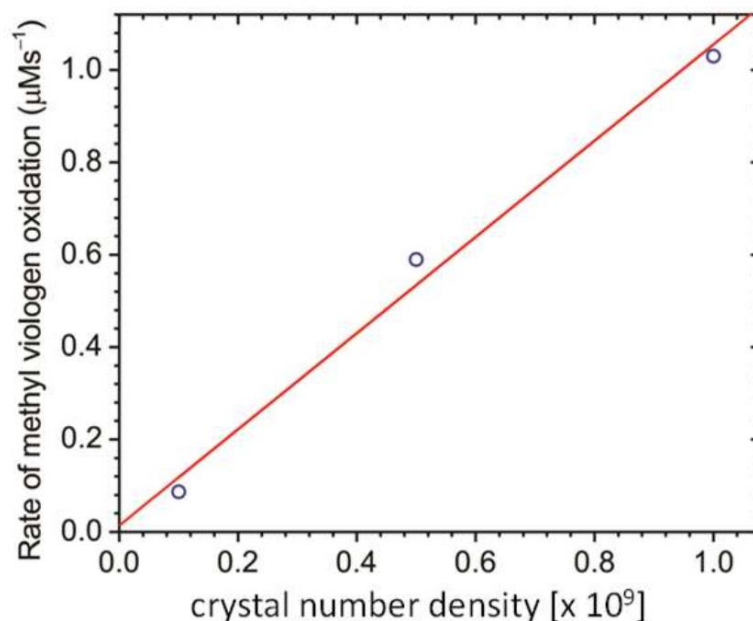


Figure 6.2. A representation of the catalytic activity of ccNiR microcrystals. The linear fit is shown in red. The activity of the crystals increases with increasing crystal number density.

30 mg/mL in 20 mM HEPES buffer at pH 7. The precipitant solution was 28 % PEG 4K, 100 mM triethanolamine at pH 7.5. The crystals were prepared by mixing protein solution (further concentrated to 40 mg/ml) and precipitant solution in 1:1 ratio and vortexing thoroughly. The final PEG concentration was 14%. The second condition started from a protein stock of 30 mg/mL in 150 mM NaCl, 50 mM HEPES, 30 mM ammonium sulfate at pH 7. The precipitant solution was 40 % PEG 4K, 200 mM sodium malonate, 100 mM MES buffer at pH 6.5. The crystals were prepared by mixing protein solution (further concentrated to 80 mg/ml) and precipitant solution in the ratio 2:1. The final PEG concentration was also 14%. An example of the crystal preparations can be observed in a Neubauer counting chamber shown in Fig. 6.3. Next, the crystal preparations were analyzed using Second Order Nonlinear Imaging of Chiral

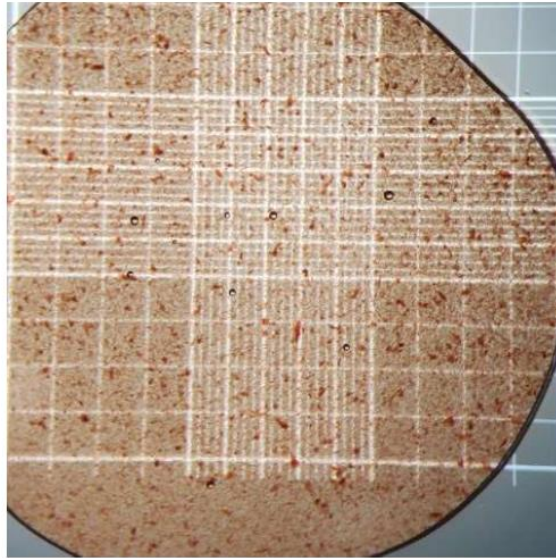


Figure 6.3. Crystal preparation viewed in a Neubauer counting chamber. In addition to crystals, amorphous debris is present.

Crystal (SONICC), which is a type of imaging technology used to distinguish protein crystals that are buried in precipitate (Fig. 6.4). Second Harmonic Generation (SHG) and Ultraviolet Two-Photon Excited Fluorescence (UV-TPEF) were combined to quickly image crystal plates and identify protein crystals. The SONICC image in Fig. 6.4 shows protein crystals fluorescing. The crystals were transferred to a Micro-Electron Diffraction (Micro-ED) grid and analyzed using a transmission electron microscope (TEM, Fig. 6.5). Originally, Micro-ED was used to determine the structure of proteins from nanocrystals. This method was used in place of X-ray diffraction when protein crystals were not of a suitable size. The main difference between Micro-ED and X-ray diffraction is the type of beam used for diffraction. The purpose of completing a screening test using Micro-ED was to confirm that the protein crystals will diffract using an XFEL. Based on results of the tests shown in Figs 6.3 – 6.5, crystallization condition 1 was used

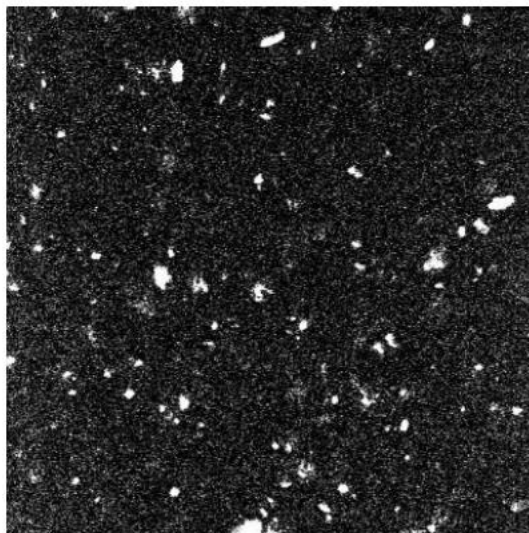


Figure 6.4. SONICC signal of ccNiR microcrystals.

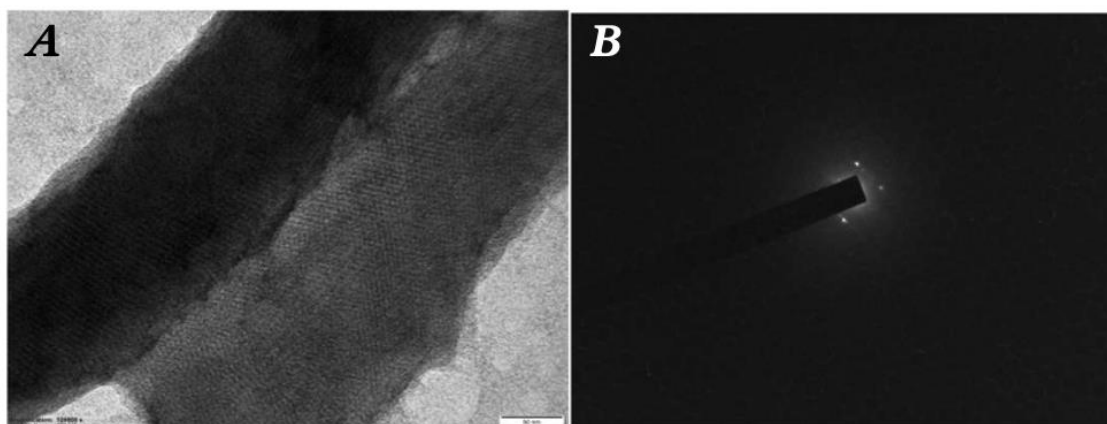


Figure 6.5. **A.** Crystal lattice. **B.** Electron diffraction using Micro-ED.

in the XFEL study at the European XFEL (Eu-XFEL). The injection was done with the double focusing injector, ID 75 μm , sample flow rate of 20 $\mu\text{l}/\text{min}$, sheet flow (ethanol) rate of 25 $\mu\text{l}/\text{min}$. Lastly, the XFEL repetition rate was 564 kHz.

6.3. Results and Discussion

6.3.1. Catalytic activity of the ccNiR micro-crystals

Since the goal of future studies is to probe transient intermediates formed during the ccNiR-catalyzed reduction of nitrite, ensuring that catalytic activity was maintained for ccNiR micro-crystals was crucial. In Chapter 2, the standard assay using methyl viologen monocation radical (MV_{red}) was described. A method was developed to test the catalytic activity of the crystals by forming anaerobic crystals, modifying the assay buffer, and performing the assay under these new conditions. Three different dilutions, $(10^9) \times$, $(5 \times 10^{10}) \times$, and $(1 \times 10^{10}) \times$ of ccNiR anaerobic micro-crystal stock were tested in the presence of MV_{red} and nitrite. The data were analyzed using the same program described in Chapter 2 Section 6.2. The rate of methyl viologen oxidation was plotted against the micro-crystal densities, as shown in Fig. 6.2. The data analysis resulted in a linear fit, showing that the activity of the ccNiR crystals increased with increasing crystal density.

6.3.2. Preliminary XFEL Investigation

Both crystallization conditions described in Section 6.2.3 produced a strong SONICC signal. However, when the crystals were transferred to a Micro-ED grid and examined with TEM, only crystallization condition 1 displayed electron diffraction (Fig. 6.5). Thus, condition 1 was chosen for further studies using the Eu-XFEL. The double-flow focusing nozzle (DFFN) as well as the conventional gas-dynamic virtual nozzle (GDVN) were used for injection. GDVN uses a flow rate of 40-50 $\mu\text{l}/\text{min}$ to produce a stable jet of protein crystals whereas DFFN has a jet that flows sample through the center, and a sheath of liquid on the outside. The DFFN streams are laminar and do not have time to mix, with a gas flow creating a meniscus in the sample stream and allowing the sample to be drawn out into a fine jet of 2-5 μm . The double-flow

focusing nozzle is preferred because this type of injection requires very little sample consumption, which is necessary for biological samples that cannot be produced in high quantities.¹² At the EuXFEL, the crystals diffracted beyond the water ring, as can be observed in Fig. 6.6, though the DFFN and GDVN frequently clogged with crystal preparations. In an attempt to minimize clogging, the crystal slurry was diluted ~100 fold; however, the crystal density then became too low to provide hit rates high enough to collect a data set and produce a diffraction pattern. The initial beamtime was a successful proof of concept that yielded nice diffraction patterns, even though a full dataset could not be collected. Further studies on crystal density and jet conditions are underway that should allow for the collection of good datasets in the near future.

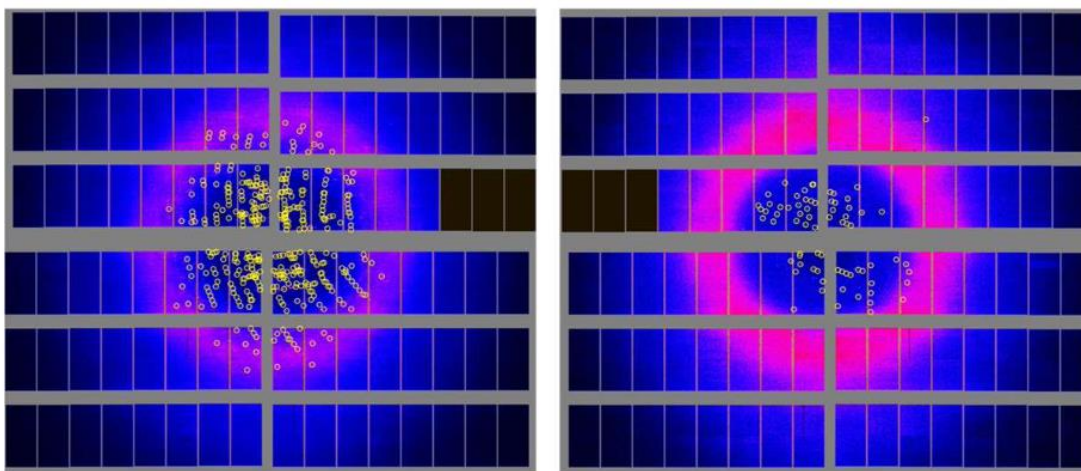


Figure 6.6. Diffraction patterns of microcrystals beyond the water ring.

6.4. References

- (1) Youngblut, M.; Judd, E. T.; Srajer, V.; Sayyed, B.; Goelzer, T.; Elliott, S. J.; Schmidt, M.; Pacheco, A. A. Laue crystal structure of *Shewanella oneidensis* cytochrome *c* nitrite reductase from a high-yield expression system. *J. Biol. Inorg. Chem.* **2012**, *17*, 647-662.
- (2) Ali, M.; Stein, N.; Mao, Y.; Shahid, S.; Schmidt, M.; Bennett, B.; Pacheco, A. A. Trapping of a putative intermediate in the cytochrome *c* nitrite reductase (ccNiR)-catalyzed reduction of

- nitrite: implications for the ccNiR reaction mechanism. *J. Am. Chem. Soc.* **2019**, *141*, 13358-13371. DOI: 10.1021/jacs.9b03036.
- (3) Einsle, O.; Stach, P.; Messerschmidt, A.; Simon, J.; Kroger, A.; Huber, R.; Kroneck, P. M. H. Cytochrome c nitrite reductase from *Wolinella succinogenes* - Structure at 1.6 angstrom resolution, inhibitor binding, and heme-packing motifs. *J. Biol. Chem.* **2000**, *275* (50), 39608-39616.
- (4) Bamford, V. A.; Angove, H. C.; Seward, H. E.; Thomson, A. J.; Cole, J. A.; Butt, J. N.; Hemmings, A. M.; Richardson, D. J. Structure and spectroscopy of the periplasmic cytochrome c nitrite reductase from *Escherichia coli*. *Biochemistry* **2002**, *41* (9), 2921-2931. DOI: 10.1021/Bi015765d.
- (5) Einsle, O.; Messerschmidt, A.; Stach, P.; Bourenkov, G. P.; Bartunik, H. D.; Huber, R.; Kroneck, P. M. H. Structure of cytochrome c nitrite reductase. *Nature* **1999**, *400* (6743), 476-480.
- (6) Cunha, C. A.; Macieira, S.; Dias, J. M.; Almeida, G.; Goncalves, L. L.; Costa, C.; Lampreia, J.; Huber, R.; Moura, J. J. G.; Moura, I.; et al. Cytochrome c nitrite reductase from *Desulfovibrio desulfuricans* ATCC 27774 - The relevance of the two calcium sites in the structure of the catalytic subunit (NrfA). *J. Biol. Chem.* **2003**, *278* (19), 17455-17465. DOI: 10.1074/jbc.M211777200.
- (7) Rodrigues, M. L.; Oliveira, T.; Matias, P. M.; Martins, C.; Valente, F. M.; Pereira, I. A.; Archer, M. Crystallization and preliminary structure determination of the membrane-bound complex cytochrome c nitrite reductase from *Desulfovibrio vulgaris* Hildenborough. *Acta Cryst. F* **2006**, *62*, 565-568.
- (8) Liu, H. A.-O.; Lee, W. The XFEL Protein Crystallography: Developments and Perspectives. *Int J Mol Sci.* **2019**, (1422-0067 (Electronic)).
- (9) Tenboer, J.; Basu, S.; Zatsepin, N.; Pande, K.; Milathianaki, D.; Frank, M.; Hunter, M.; Boutet, S.; Williams, G. J.; Koglin, J. E.; et al. Time-resolved serial crystallography captures high-resolution intermediates of photoactive yellow protein. *Science* **2014**, *346*, 1242-1246.
- (10) Levantino, M.; Schirò, G.; Lemke, H. T.; Cottone, G.; Glowonia, J. M.; Zhu, D.; Chollet, M.; Ihee, H.; Cupane, A.; Cammarata, M. Ultrafast myoglobin structural dynamics observed with an X-ray free-electron laser. *Nature Communications* **2015**, *6* (1), 6772. DOI: 10.1038/ncomms7772.
- (11) Ali, M. Probing the early steps in the catalytic reduction of nitrite to ammonia, catalyzed by cytochrome c nitrite reductase. University of Wisconsin-Milwaukee, Milwaukee, WI, 2019.
- Shahid, S. A mechanistic investigation of cytochrome c nitrite reductase catalyzed reduction of nitrite to ammonia: the search for catalytic intermediates. University of Wisconsin-Milwaukee, Milwaukee, WI, 2020.
- (12) Stagno, J. R.; Liu, Y.; Bhandari, Y.; Conrad, C.; Panja, S.; Swain, M.; Fan, L.; Nelson, G.; Li, C.; Wendel, D.; et al. Structures of riboswitch RNA reaction states by mix-and-inject XFEL serial crystallography. *Nature* **2017**, *541*, 242-246.

Chapter 7 Concluding Remarks

This thesis provides several important new insights about the ccNiR mechanism. The results from Chapter 3 demonstrate that release of free hydroxylamine from ccNiR is minimal even under conditions that should most favor such release. These conditions are a 1:1 mixture of I3S_{red} and I3S_{ox} that poises the solution potential at ~ -90 mV vs SHE, which is a potential at which protein film voltammetry studies show ammonium formation to be comparatively slow,¹ and at which spectropotentiometric studies show that accumulation of a 4-electron reduced ccNiR intermediate is most likely.²

Perhaps the pivotal assays described in this thesis are found in Chapter 4. The quantification of ammonium formed in the ccNiR-mediated reduction of nitrite by the weak reductants reduced indigo trisulfonate (I3S_{Red}), reduced indigo tetrasulfonate (I4S_{Red}) and hexaammineruthenium(II) (Ru^{II}) showed that ammonium was virtually the sole product when I3S_{red} was the reductant, but was produced in ~50% yield when I4S_{red} was the reductant, and maybe not at all when Ru^{II} was the reductant. Such experiments help put an upper limit on the amount of side product that could be forming under each set of conditions, and they also provide guidance about the putative ccNiR intermediates that could form under those conditions.

Chapter 5 described UV-Visible stopped-flow experiments aimed at identifying optimal conditions for detecting and characterizing a putative four-electron reduced ccNiR intermediate (Fig. 1.7). The experiments showed that I3S_{Red} and I4S_{Red} are the ideal weak reductants that can be used in future EPR studies to assist in trapping the formally hydroxylamine-Heme #1 bound active site in the catalytic cycle. Interestingly, the studies in this chapter also showed that even when MV_{red} is used, enzymatic intermediates with nitrogen moieties in the active site are detectable after the MV_{red} has been consumed, and that these moieties are comparatively long-

lived. These results open the door to many future studies in which the nitrosylated intermediates will be prepared by rapid freeze-quench and examined using a variety of EPR techniques and Mossbauer spectroscopy. Because MV_{red} initially reduces many of ccNiR's low potential hemes at the same time as the nitrite-loaded heme 1, experiments with this reductant may remove some of the spin couplings that complicate interpretation of the ccNiR EPR spectra obtained when most hemes are in their ferric state. As the hemes sequentially re-oxidize, couplings will sequentially re-appear and can thus be deconvoluted.

Lastly, Chapter 6 presented preliminary studies that have, as a long-term goal, the investigation of the 2-electron reduced ccNiR intermediate by time-resolved X-ray crystallography. These preliminary experiments provided knowledge about the conditions needed for making ccNiR microcrystals, catalytic studies of microcrystals using the standard assay, and SONICC Signal and Micro-ED crystal screening tests. Initial diffraction patterns were also obtained with the European X-ray free electron Laser (EuXFEL). With the studies presented in this thesis, a very clear path has been paved towards more experiments. In collaboration with Professor Schmidt from the UWM Physics Department, studies of the the reaction of nitrite-loaded ccNiR with weak reductants using time-resolved serial femtosecond X-ray crystallography (TR-SFX) can be completed once an initial crystal structure of ccNiR is obtained with microcrystals. Specifically, we anticipate being able to crystallographically characterize the $\text{Fe}_{\text{HI}}^{\text{II}}(\text{NO}_2^-)$ and $\{\text{Fe}_{\text{HI}}\text{NO}\}^7$ species that are proposed to be trapped when nitrite-loaded ccNiR is reduced by a weak reductant such as TMPD. Further in the future, the 4-electron reduced ccNiR catalytic intermediate might also be investigated using the TR-SFX technique.

The results presented in this thesis mainly focused on the detection and kinetic characterization of putative intermediates generated during the ccNiR-catalyzed reduction of

nitrite to ammonium. These results indicate the way in which future investigations that aim to characterize the catalytic intermediates structurally and spectroscopically should be conducted. Preliminary EPR characterization of $\{\text{Fe}_{\text{HI}}\text{NO}\}$ ⁷, and the proposed species $[\{\text{Fe}_{\text{HI}}(\text{HNO})\}]$ ⁸, $\text{Fe}_{\text{H4}}^{\text{II}}$ and $[\text{Fe}_{\text{HI}}^{\text{II}}\text{H}_2\text{NO}\cdot, \text{Fe}_{\text{H4}}^{\text{III}}]$ has already been done previously by the Pacheco group,³ but these studies left many questions unanswered. By using a suite of reductants with varying midpoint potentials to poise the reaction solutions at different potentials, these and other intermediates will be trapped by rapid freeze-quench to be studied by advanced EPR techniques or Mossbauer spectroscopy or investigated by TR-SFX at an XFEL facility. Future spectroscopic studies will be done in collaboration with Dr. Wilcoxon of the UWM Chemistry department, while TR-SFX studies will be done in collaboration with Dr. Schmidt of the UWM Physics department.

7.1 References

- (1) Judd, E. T.; Youngblut, M.; Pacheco, A. A.; Elliott, S. J. Direct Electrochemistry of *Shewanella oneidensis* Cytochrome *c* Nitrite Reductase: Evidence of Interactions across the Dimeric Interface. *Biochemistry* **2012**, *51* (51), 10175-10185. Judd, E. T.; Stein, N.; Pacheco, A. A.; Elliott, S. J. Hydrogen bonding networks tune proton-coupled redox steps during the enzymatic six-electron conversion of nitrite to ammonia. *Biochemistry* **2014**, *53*, 5638-5646.
- (2) Stein, N.; Love, D.; Judd, E. T.; Elliott, S. J.; Bennett, B.; Pacheco, A. A. Correlations between the electronic properties of *Shewanella oneidensis* cytochrome *c* nitrite reductase (ccNiR) and its structure: effects of heme oxidation state and active site ligation. *Biochemistry* **2015**, *54*, 3749-3758.
- (3) Ali, M.; Stein, N.; Mao, Y.; Shahid, S.; Schmidt, M.; Bennett, B.; Pacheco, A. A. Trapping of a putative intermediate in the cytochrome *c* nitrite reductase (ccNiR)-catalyzed reduction of nitrite: implications for the ccNiR reaction mechanism. *J. Am. Chem. Soc.* **2019**, *141*, 13358-13371. DOI: 10.1021/jacs.9b03036. Youngblut, M.; Judd, E. T.; Srajer, V.; Sayyed, B.; Goelzer, T.; Elliott, S. J.; Schmidt, M.; Pacheco, A. A. Laue crystal structure of *Shewanella oneidensis* cytochrome *c* nitrite reductase from a high-yield expression system. *J. Biol. Inorg. Chem.* **2012**, *17*, 647-662. Youngblut, M.; Pauly, D. J.; Stein, N.; Walters, D.; Conrad, J. A.; Moran, G. R.; Bennett, B.; Pacheco, A. A. *Shewanella oneidensis* cytochrome *c* nitrite reductase (ccNiR) does not disproportionate hydroxylamine to ammonia and nitrite, despite a strongly favorable driving force. *Biochemistry* **2014**, *53*, 2136-2144.